Doubly Fed Drives for Variable Speed Wind Turbines

Lindholm, Morten; Rasmussen, Tonny Wederberg; Andersen, Kurt; Pedersen, Jørgen Kaas

Publication date:
2004

Document Version
Publisher's PDF, also known as Version of record

Morten Lindholm

Doubly Fed Drives for Variable Speed Wind Turbines

A 40kW laboratory setup

Technical University of Denmark
Ørsted
2800 Lyngby
Denmark

To Katrina, Oskar and Frederik

Student:	M.Sc.E.E. Morten Lindholm ID# : s928912
Company:	NEG Micon Control Systems A/S Frankrigsvej 8450 Hammel Denmark Tel: (+45) 87 62 26 00
University:	Technical University of Denmark Ørsted.DTU Anker Engelundsvej 2800 Lyngby Denmark
Financing:	This project is fully funded by NEG Micon Control Systems A/S.
Supervisor:	
University main supevisor: April 2000 - April 2002: Retired	Jørgen Kaas Pedersen Technical University of Denmark Ørsted.DTU
April 2000 - September 2003:	Tonny W. Rasmussen Technical University of Denmark Ørsted.DTU
University secondary supervisor April 2002 - September 2003:	Kurt Andersen Technical University of Denmark Ørsted.DTU
Industrial supervisor:	Jan Kristiansen NEG Micon Control Systems

Abstract

This thesis deals with the use of variable speed wind turbines. Different wind turbine generator topologies are described. In particular, the reduced variable speed turbine, which uses a doubly fed induction generator, is covered.

An overview of the power electronic inverters of interest to the field of wind energy is given and a topology for a laboratory model is selected. The discipline of Pulse Width Modulation is presented.

The vector control principles of induction machines and grid connected inverters are derived. Having the stator connected directly to the grid it is given that the flux level in the machine, is nearly constant. This means that changes in either the flux or torque producing current in the rotor circuit are limited by the transient time constant of the machine.

A 40 kW laboratory model with a doubly fed induction generator and a 3-level neutral point clamped back to back power converter is constructed.

Adaptive active filters are used to reduce harmonics and slip harmonics in the stator current. The filters are implemented in both inverters.

The active filters reduce the stator harmonics by 20-30 dB. The filters can reduce the slip harmonics at variable speed.

Resume

Denne Ph.D. afhandling omhandler brugen af variabel hastighed vindmøller. Forskellige vindmølle generator typer er beskrevet. Specielt med focus på reduceret variabel hastigheds vindmøller, herunder den dobbelt fødet asynkron generator.

Der er givet et gennemgang af de forskellige effektelektroniske inverter topologi, der har interesse for brug i forbindelse med vindmøller. Een topologi er valgt til brug for en laboratorie model. En detaljeret gennemgang af pulsbredde modulation er givet.

Principperne for vektor kontrol af asynkron maskiner og nettilsluttede invertere er beskrevet. Resultater, for vektor kontrol af dobbelt fødet, viser at både den moment og den felt producerende rotor strøm vector har ens respons tid, idet at statoren er koblet direkte til nettet, og dermed er feltet i motoren næsten konstant.

En 40 kW laboratorie model er opbygget med en dobbelt fødet asynkron generator med tilhørende effektelektronisk styring. En 3 niveau *neutral point clamped* back to back effektkonverter er konstrueret.

Adaptive aktive filtre er anvendt til a reducere harmoniske og slip harmoniske stator strømme. Filterne er implementeret i begge invertere.

Målinger viser at de aktive filtere kan reducere stator strømme med 20-30 dB. Filterne kan reduce de slipharmoniske selv ved variabel hastighed.

Acknowledgements

This thesis is fully funded by NEG Micon Control Systems. I would like to thank the company for its financial support throughout the project.

I would like to thank my main supervisor for the first two years associate professor Jørgen Kaas Pedersen, and associate professor Tonny W. Rasmussen for the last year as main supervisor, but who followed the project from the beginning.

One person is to blame for the birth of this project, Ole Nymann, without whom the project would never have been a reality.

Thanks to associate professor Kurt Andersen for his supervision.

I would like thank all my colleagues at Ørsted.dtu, Technical University of Denmark, but also thanks to my colleagues at NEG Micon Control Systems, especially in the final months of this project.

Finally, a thanks goes to my wife, Katrina, who has had to live with me during this project and proof read the thesis.

Contents

List of Figures

1

Introduction

1.1 Background

The penetration of wind energy into the electrical grid has increased tremendously in the last 10 years, especially in Denmark and Germany. Other countries have also had an increase in installed wind energy production capacity, e.g. Spain. In Denmark, installed wind power is 28% of the total installed electrical power.

Five to ten years ago, the standard wind turbine was a simple and highly reliable stall controlled turbine. This type of turbine was designed to produce electricity whenever the wind speed was high enough and the grid was stable. In situations of grid instability, the turbine would disconnect. For a small number of wind turbines, this works fine, but in the case of a large penetration of wind energy, turbines have to help stabilize the grid. This requires turbines that are more controllable.

A way to make more controllable turbines is variable speed. Variable speed turbines can store some of the power fluctuations due to turbulence by increasing the rotor speed. By pitching the rotor blades, these turbines can control the power output at any given wind speed. As will be described in this thesis, a way to transfer the wind energy from a variable speed turbine to the electrical grid is a combination of an electrical generator and a power converter.

The doubly fed induction generator with a power converter is a simple and highly controllable way to transform the mechanical energy from the variable speed rotor to a constant frequency electrical utility grid.

One of the main objectives of this Ph.D. project was to set up a laboratory model of a variable speed generator with power electronic inverters. The generator used for the model is a doubly fed induction generator, with two back to back 3-level neutral point clamped inverters.

1.2 Thesis outline

This thesis is organized as follows:

Chapter 2 General description of wind energy production from a historical perspective. Introduction to different aerodynamic control principles. Finally, a brief overview of power quality.

Chapter 3 An overview of different generator topologies that are of interest with respect to wind turbines.

Chapter 4 The different reference frames used throughout the thesis are presented. The nature of positive, negative and zero sequence is shown.

Chapter 5 Presents a classification of the different types of doubly fed induction generators.

Chapter 6 Deals with equations related to the induction generator and the doubly fed induction generator. Describes the problem of turn ratio in relation to doubly fed machines and shows the steady state equivalent diagram.

Chapter 7 Covers different three phase inverter topologies, including 2-level inverters hard or soft switched and multilevel inverters. Introduces the problem of neutral point balancing.

Chapter 8 Describes some of the features of PWM, including suboscillation PWM, space vector modulation and various discontinuous PWM methods. Space vector modulation together with 3-level inverter are covered. A simple method to implement space vector modulation in 3-level inverters is described. Finally, a more in-depth discussion of the neutral point balancing problem.

Chapter 9 In this chapter, the principles of vector control are stated, with a discussion of the different flux oriented frames. Vector control of the doubly fed induction generator is more thoroughly described.

Chapter 10 Presentation of vector control and amplitude-phase control of a grid connected inverter. A comparison of different phase lock loops is presented.

Chapter 11 Gives an overview of the harmonics in the stationary and synchronously rotating reference frames. Presents a table with the harmonics in the doubly fed induction generator.

Chapter 12 In this chapter, an adaptive filter is presented. Both inverters can be used as an active filter.

Chapter 13 Description of the hardware used in the laboratory set up.

Chapter 14 A short presentation of some of the software.

Chapter 15 Presents the measurements and results.

Chapter 15 The conclusion.

Appendix A Glossary of symbols, superscripts and subscripts that are used in the thesis.

Appendix B Includes the look-up table used in relation to the space vector modulation.

Appendix C List of parameters of the doubly fed induction generator and the motor used as the load.

Appendix D Includes schematics of the PCBs used in the laboratory model.

Appendix E Includes additional measurements.

Appendix F Includes the programming source code (Not include in the public version).

Appendix G Contains a submitted and accepted paper with the title: "Harmonic Analysis of Doubly Fed Induction Generators".

Part I

Wind Turbines and Doubly Fed Induction generators

2

Wind Energy Generation

For more one than thousand years, wind energy has been used by humans [1]. Until the end of the 19th century, wind power was only used in mechanical constructions, such as grain grinding, etc. In 1891, Danish Poul la Cour started his work on the electrical wind turbine at Askov folk high school; this was the start of Danish wind turbines [6]. During World War I and II, Denmark was cut off from its supply of oil and electrical energy from wind turbines was important, though not sufficient. In 1957, J. Juul made his 200 kW Gedser wind turbine. During the oil crises in the mid-1970s, it became apparent that alternative energy to oil was needed. That started the Danish wind energy industry.

In the beginning of the 1980s, the first wind turbine gold rush in California happened. Back then, the traditional Danish wind turbine drive train was also made up of a 3-bladed rotor, a gear box and an induction generator, better known as the "Danish standard". The average turbine contained a 55 kW induction generator. During the 1980s, turbines increased in size, but the penetration of wind energy into the electrical grid was marginal. There were no major problems, with the induction generators drawing reactive power from the grid. At the end of the 1980s, the larger Danish turbines were equipped with a 35 m rotor and a 350-450 kW induction generator [6].

More advanced drive trains have been made since the beginning of the 1980s, but not on a large commercial basis. The drive train topologies can be divided into two groups: fixed speed and variable speed. Both groups

can again be split into two groups one with induction generators and one with synchronous generators. In addition there is a drive train without a gear box. The generators used here are with multipole synchronous machines.

Today the biggest commercial turbines are 4-5 MW. Enercon has developed a prototype of a 5 MW synchronous multipole direct driven turbine, and NEG Micon is producing a 4.2 MW doubly fed induction generator turbine with gear box. Both are with pitch controlled rotor.

2.1 Wind Energy

The power available in the wind flowing through an area A is given by

$$P_{wind} = \frac{1}{2}\rho v_w^3 A \tag{2.1}$$

where A is the area swept by the turbine blades, ρ is the air density, v_w is the velocity of the wind.

The mechanical power produced by the wind turbine can be expressed as [7]

$$P_{mech} = \frac{1}{2}C_p\rho v_w^3 A \tag{2.2}$$

where C_p is the power performance coefficient. The maximum C_p for a typical wind turbine is 0.48-0.50. The theoretical maximum of C_p is called Betz limit and is equal to $16/27 = 0.59$ [1].

The tip speed ratio is $\lambda = v_{tip}/v_w$. The tip speed lies between 60 and 80 m/s. The turbines start production at wind speeds above 2 m/s and reach maximum power production around 12-15 m/s ($v_{P_{\max}}$) depending on rotor diameter. Most of the turbines shut down at wind speeds above 25 m/s. When the wind speed is above 12-15 m/s, the rotor has to waste the excess power by letting it pass by the rotor, in order not to damage the turbine. Commercial wind turbines are designed to make maximum power at a given wind speed. For a fixed speed turbine the power production is only optimized for one wind speed. Figure 2.1 shows the normalized rotor speed vs. normalized electrical power. The power output for a fixed speed

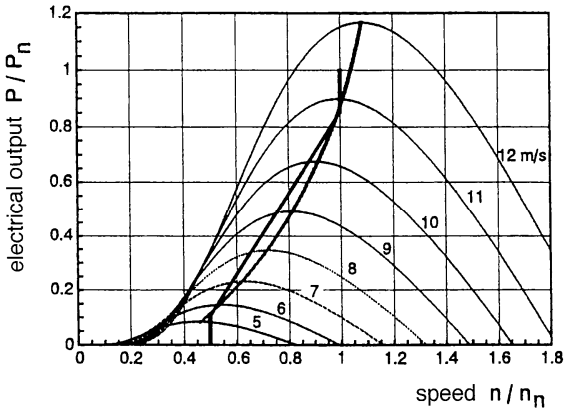

Fig. 2.1. Electrical power vs. rotor speed (figure is from [1])

turbine can be drawn on the figure as a vertical line at n/n_n equal to one, optimal production is only meet at 11 m/s. The curves in Fig. 2.1 can be shifted left or right, in order to optimize the turbine to a given site. A variable speed turbine on the other hand can optimize its speed, so optimal power is meet for any wind speed, this is showed by the thicker line in Fig. 2.1. Power extraction from the wind can be controlled in different ways, including stall control and pitch control.

2.2 Stall control

The control principle of stall control is fairly simple. With passive stall, the rotor blades are mounted with a fixed angle to the rotor hub. At wind speeds below $v_{P_{\max}}$, laminar flow is obtained around the rotor blades. When wind speeds are above $v_{P_{\max}}$, the flow starts to detach from the blade and turbulence occur behind the rotor blade, see Fig. 2.2. In order to use the stall phenomenon to control the maximum power, the stall region has to be rather accurate. How clean the blades are a factor for the stall point. If the surface of blades are covered with dirt and insects the maximum production is decreased since the stall will occur at lower wind speeds. Equation (2.2) shows that the density of the air is a factor of the power production, therefore the power production depends on the air temperature. The blade angle on a stall controlled turbine is chosen so

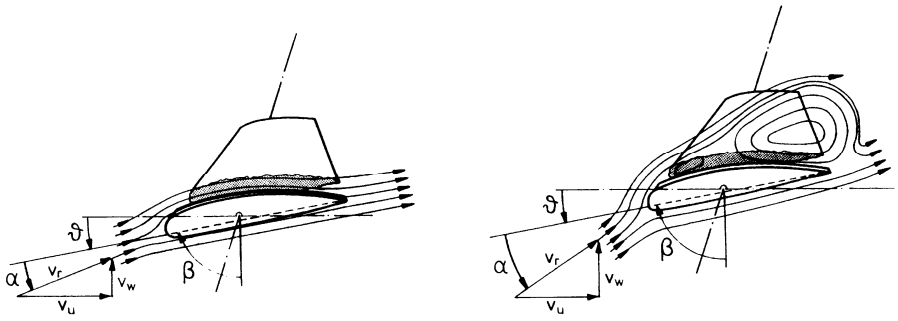

(a) laminar flow (b) stalling

Fig. 2.2. Airflow behaviour at the rotor balde (figures are from [1])

that its production is maximized at a given temperature. Which in turn causes problems with changing seasons. In order to overcome this issue, NEG Micon now sells a hub with the possibility of slowly changing the blade angle 1-2 degrees, this feature is sold under the name Power Trim$^{\text{TM}}$.

One of the disadvantages of this power limiting control principle can be seen in Fig. 2.3 where power around $v_{P_{\max}}$ gives a little overshoot.

2.2.1 Active stall

A more advanced way to control the power is active stall. With active stall, the blades are mounted on a hub that is capable of a fast change of the blade angle a few negative degrees. The power controller will try to maintain maximum production at any given wind speed by pitching the blade. Above rated wind speed, i.e. rated power, the controller will pitch the blade in order to enforce the stall effect. By actively controlling the stall, the power curve looks like Fig. 2.4, where the power overshoot is not present. Active stall eliminates negative side effect of passive stall such as temperature dependant maximum production and blade contamination.

2.3 Pitch control

When controlling a wind turbine with pitch control, blade angle is changed with a positive angle, as opposed to stall where a negative angle is used. Instead of forcing stall to occur, the blades are pitched out of the wind. As in stall controlled turbines the controller will try to maintain max C_p. Above rated wind speed, the blades are pitched out of the wind and when the wind speed reduces again, the blades are pitched back into the wind. This results in a lot of trimming of the pitch angle compared to active stall. The angle the blades have to be pitched is about 10-20 degrees.

Since pitch control limits power by pitching the blade out of the wind, fast power fluctuations in the wind above rated wind speed will also result in a fast electrical power fluctuation above rated power, unless the blades can be pitched fast enough to overcome the fluctuation. This can not be accomplished. Therefore some kind of variable speed has to be used together with pitch controlled turbines. For stall controlled turbines, power limitation occurs due to the physics of the aerodynamics of the stall principle.

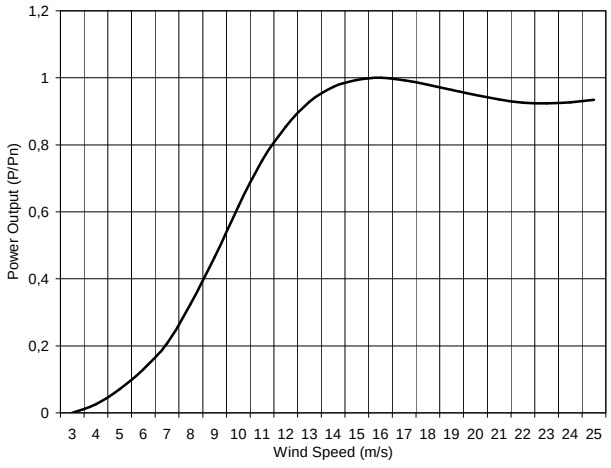

Fig. 2.3. Power curve for a stall controlled wind turbine.

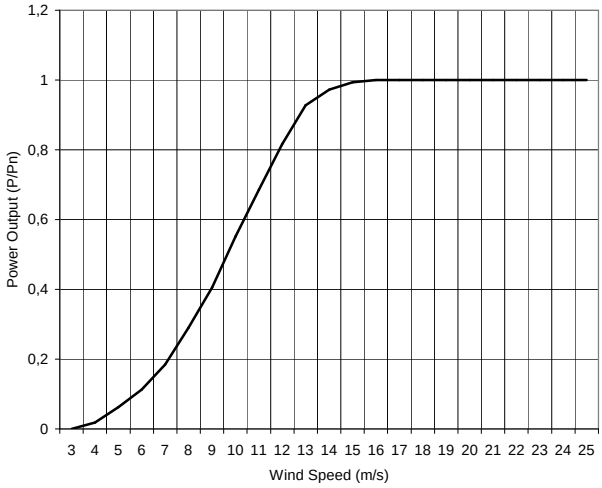

Fig. 2.4. Power curve for an active stall controlled wind turbine.

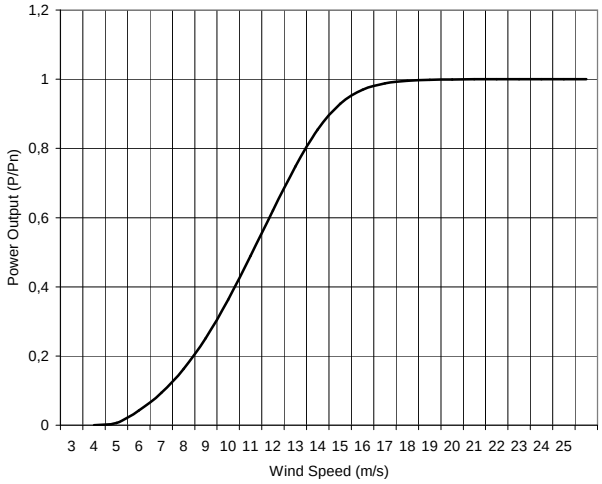

Fig. 2.5. Power curve for a pitch controlled wind turbine.

2.4 Power Quality of Wind Turbines

Ideal power quality is met when the voltage is purely sinusoidal with constant amplitude and frequency. In some cases voltage harmonics must be considered as a problem. Power quality can be expressed in terms of the physical characteristics of electricity.

Grid connected wind turbines have an effect on power quality, and this effect is of course dependent on the amount of wind energy supplied to the grid, but also on the quality of power from each individual turbine. Due to the large penetration of wind energy into the Danish and German utility grid, the power quality issue attracts more and more focus. The German utility company E.on. has one of the most restricted grid connection requirement at moment [8]. Today, wind turbines are a significant part of electrical production units, so during grid faults it is no longer a *de facto* standard that wind turbines automatically disconnect from the grid until the situation has stabilized. Instead, they have to stay connected and ride through the fault condition, perhaps also helping to stabilize the grid with reactive power during the fault.

Power quality has to follow national and international standards e.g. IEC 61400-21 [9]. Various measures are covered by the standard, such as reactive power, voltage fluctuation and harmonics.

2.4.1 Voltage Fluctuations

The voltage fluctuations imposed by a wind turbine are mainly due to variations in load and power production. Voltage fluctuations are defined as changes in the RMS value of the voltage over different time periods, depending on the standards the turbine has to fulfill.

The voltage fluctuation can be calculated by this simplified expression

$$\frac{\Delta u}{U} = \frac{R \cdot P + X \cdot Q}{U} \tag{2.3}$$

where R is the resistance, X is the reactance of the line, P is the produced active power and Q is the produced reactive power. U is the line voltage. Since the impedance of the line is more inductive or capacitive than resistive, the voltage is more sensitive to variations in the reactive power than to variations in the active power.

One of the main concerns about voltage fluctuations is flicker. Flicker is a way of quantifying voltage fluctuations. The fluctuations are weighted by two different filters. One filter corresponds to the response of a 60W light

bulb and the other to the response of the human eye and brain to variations in luminance of the light bulb [10]. According to the IEC 61400-21, flicker emission should not be determined purely from voltage measurements. In order not to measure background flicker, a set of 3 current and 3 voltage measurements are used to measure flicker.

2.4.2 Harmonics

Wind turbines equipped with power electronic converters will cause some sort of higher harmonics. Eventhough IEC 61400-21 does not have any requirements for turbines without power electronics, the generator itself will cause some harmonics. For turbines with converters, the harmonics are specified for frequencies up to the 50th harmonic of the fundamental grid frequency, plus there are some restrictions on the level of interharmonics.

3

Generator Topologies in Wind Turbines

As discussed in last chapter wind turbines are working either at fixed speed (small speed changes due to the generator slip) or variable speed. Variable speed is here understood as 5% to 100% variation of norminal speed. On variable speed turbines, energy can be stored in the rotor as increased rotational energy, this is not the case for fixed speed turbines. Therefore will the turbulence of the wind cause fluctuations in the instantaneous power from a fixed speed turbine. The variable speed turbines are usually controlled by power electronic converters together with the generator. By means of power electronics the rotor speed is controlled, the turbulence of the wind is accumulated in the rotor speed. Hence, the power quality impact from the wind turbine is improved by using variable speed [11].

In the following there will be a short overview of various wind turbine generator topologies, it is not complete and detailed.

3.1 Constant speed system

The generator in the constant speed system is most often an induction generator, see Fig. 3.1, connected directly to the grid, and mechanically the rotor is connected through a gear box. In order to reduce power fluctuations the induction generator in this setup is designed with a higher slip than normal.

These turbines are only compensated for its no-load reactive power, mainly to avoid trouble with over compensation. An overcompensated turbine, can if disconnected from the grid cause over voltages.

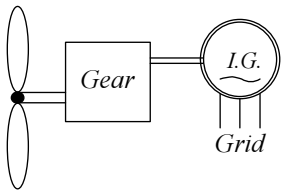

Fig. 3.1. Constant speed generator

This system will also work if equipped with a synchronous generator with excitation, but this is not used in large volumes, and use of a synchronous generator may cause problems during grid faults.

The rotor blade used together with a constant speed generator is a stall or active stall controlled rotor blade.

3.2 Variable speed systems

Since the late 1990's the trend throughout the hole wind turbine business have been to implement variable speed in their larger turbines. Using variable speed makes the electrical system of the turbine more complex, compared to a fixed speed turbine. Newer grid requirement need advanced power regulation, that might include some kind of power electronics even in a fixed speed turbine, due to reactive power compensation.

When the rotor speed is variable it is most optimal to use pitch controlled rotor blades .

3.2.1 Full range variable speed system

This system uses a conventional wind turbine setup plus an inverter connected to the stator, Fig. 3.2. The inverter used has to have active switches in both the grid and the generator side converters, allowing the converter

at the generator side to supply reactive power to the generator, while active power is flowing from the generator. This differs from a conventional industrial drive made with motors, where the grid side converter nearly always is a simple passive diode rectifier, and only the motor side converter is equipped with active switches. With this system, the turbine has full speed range, from zero RPM to well above synchronous speed, if desired. The generator can be a normal induction generator, a synchronous generator or a permanent magnet synchronous generator. It is possible to make this system with a simple passive rectifier at generator side. This requires powerful magnets or some kind of external excitation of the generator in order to magnetize the generator.

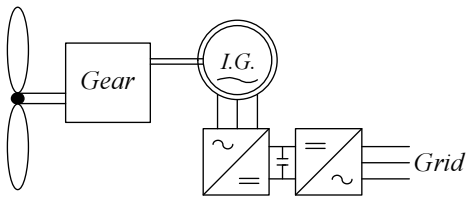

Fig. 3.2. Variable speed generator

Compared to the DFIG system in Fig. 3.4 the full speed range system needs a converter rated at full power, where as the rating of the converters of the limited range variable speed system could be only 20-30% of full power.

In order to utilize the variable speed, this system need blade rotation in the pitch region, since variable speed and stall control doesn't go together, due to the fact that an increase in speed, would push the stall region further up and increase maximum power. The disadvantage for the full speed range system is that all the power has to be converted in the inverter.

3.2.2 Full range variable speed system, without gear

The generator used here is a multiple pole synchronous machine, either with excitation system or with permanent magnets. The lack of gear box

losses partly compensates for the large losses in the full power converters.

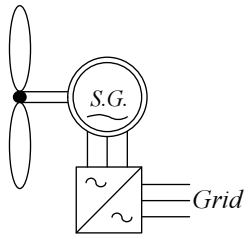

Fig. 3.3. Variable speed synchrounous generator

Normally the mechanical structure of multiple pole generators have rather large diameters, and the weight of the system is well above the weight of a 4-6 pole generator plus a gear box, but if the multiple pole machine is integrated in the turbine nacelle, so that the main bearing etc. are part of the generator, it might break even.

3.2.3 Limited range variable speed system

This system is also known as the doubly fed induction generator system. It is a variable-speed constant-frequency induction generator, where the stator is connected directly to the grid while the rotor via slip rings is connected to a inverter. The system consist of a gear box, a generator and a rotor inverter, see Fig. 3.4.

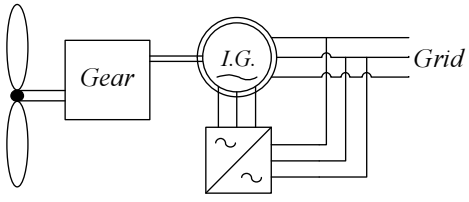

Fig. 3.4. Variable speed with doubly fed induction generator

The limitation in the speed range is limited by the frequency converter, since the speed range is proportional to the power flowing in the rotor. The rotor blades in the system are pitched controlled.

A more in depth coverage of the doubly fed induction generator will be presented in the following chapters.

4

Reference Frame Conversion

When working with three phase systems, it is often more convenient to do a transformation to a two phase system in the complex plane. Doing this for a system without a zero connection, all the information is kept. Using the signals from the two phase system in feedback control is not desirable due to the sinusoidal property of the signals. In order to overcome this, a transformation from the stationary reference frame to a rotating reference frame is used. As a result, the fundamental part of the signal appear as constant values in steady state.

The content of this chapter was first intended to be in the appendix. However, many definitions stated here are used in the following chapters, thus this topic is covered here.

4.1 Transformation from a Three Phase to a Two Phase System

The three quantities (s_a, s_b and s_c) can be transformed to a two phase vector system by

$$\vec{s}_{\alpha\beta} = s_\alpha + j s_\beta = c\left(s_a e^{j0} + s_b e^{j\frac{2\pi}{3}} + s_a e^{j\frac{4\pi}{3}}\right) \tag{4.1}$$

or expressed in matrix notation

$$\begin{bmatrix} s_\alpha \\ s_\beta \end{bmatrix} = c \begin{bmatrix} 1 & -\frac{1}{2} & -\frac{1}{2} \\ 0 & \frac{\sqrt{3}}{2} & -\frac{\sqrt{3}}{2} \end{bmatrix} \cdot \begin{bmatrix} s_a \\ s_b \\ s_c \end{bmatrix} \tag{4.2}$$

If extended with a zero system the matrix notation is given by

$$\begin{bmatrix} s_\alpha \\ s_\beta \\ s_o \end{bmatrix} = c \begin{bmatrix} 1 & -\frac{1}{2} & -\frac{1}{2} \\ 0 & \frac{\sqrt{3}}{2} & -\frac{\sqrt{3}}{2} \\ \frac{\sqrt{2}}{2} & \frac{\sqrt{2}}{2} & \frac{\sqrt{2}}{2} \end{bmatrix} \cdot \begin{bmatrix} s_a \\ s_b \\ s_c \end{bmatrix} \tag{4.3}$$

where c is a constant. If the value $c = \frac{2}{3}$ is chosen, then the length of the voltage and current vectors are maintained. If, instead the value $c = \sqrt{\frac{2}{3}}$ is selected, then power calculated in the $\alpha\beta$-frame is the same as in the *abc*-frame, and the $\alpha\beta$-system is said to be power invariant. In the following, $c = \frac{2}{3}$ is used, and the system is then non-power invariant.

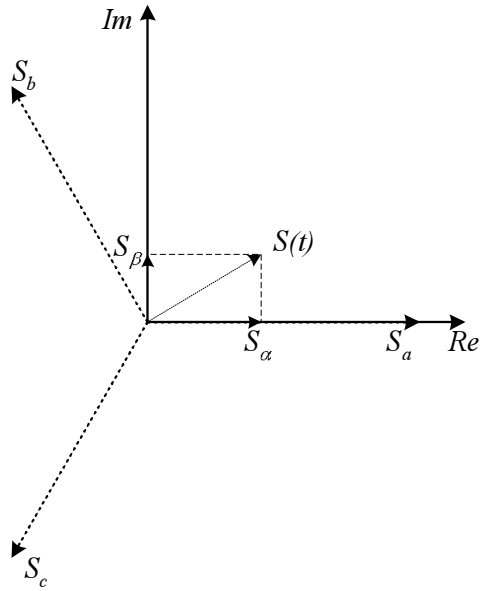

Fig. 4.1. A space vector in the stationary reference frame in the complex plane.

For (4.1) or (4.2) it applies that the three phase quantities are sinusoidally varying with RMS value S, angular frequency ω_1 and phase shifted

$\frac{2\pi}{3}$ in time given by

$$\begin{cases} s_a = \sqrt{2}S\cos(\omega_1 t) \\ s_b = \sqrt{2}S\cos(\omega_1 t - \frac{2\pi}{3}) \\ s_c = \sqrt{2}S\cos(\omega_1 t - \frac{4\pi}{3}) \end{cases} \tag{4.4}$$

The RMS value S can then be expressed as

$$\vec{s}_{\alpha\beta} = \sqrt{3}Se^{j\omega_1 t} \tag{4.5}$$

The transformation in (4.2) and (4.3) is valid for voltage u, current i and flux ψ in any measuring system: stator, rotor or magnetizing flux.

When the voltage measurements are done using two line to line measurements, the equations are

$$\begin{bmatrix} u_\alpha \\ u_\beta \end{bmatrix} = \begin{bmatrix} \frac{1}{3} & -\frac{1}{3} \\ -\frac{1}{\sqrt{3}} & -\frac{1}{\sqrt{3}} \end{bmatrix} \cdot \begin{bmatrix} u_{BA} \\ u_{AC} \end{bmatrix} \tag{4.6}$$

where

$$u_{BA} = u_A - u_B \tag{4.7}$$

$$u_{CB} = u_B - u_C \tag{4.8}$$

$$u_{AC} = u_C - u_A \tag{4.9}$$

$$u_A + u_B + u_C = 0 \tag{4.10}$$

4.2 Transformation from Stationary to Rotating System

A vector in the stationary reference $\alpha\beta$-frame is transformed into the synchronously rotating reference dq-frame oriented in the direction given by the angle θ

$$\vec{s}_{dq} = s_d + js_q = \vec{s}_{\alpha\beta}e^{-j\left(\omega_1 t - \frac{\pi}{2}\right)} = \vec{s}_{\alpha\beta}e^{-j\theta} \tag{4.11}$$

This can also be written in matrix form

$$\begin{bmatrix} s_d \\ s_q \end{bmatrix} = \begin{bmatrix} \cos\theta & \sin\theta \\ -\sin\theta & \cos\theta \end{bmatrix} \cdot \begin{bmatrix} s_\alpha \\ s_\beta \end{bmatrix} \tag{4.12}$$

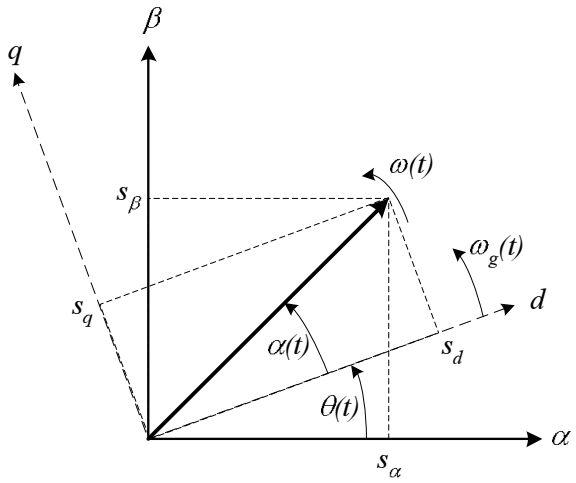

Fig. 4.2. The relation between the $\alpha\beta$-frame and the dq-frame.

The inverse transformation, from the synchronously rotating reference dq-frame to the stationary reference $\alpha\beta$-frame is given by

$$\vec{s}_{\alpha\beta} = \vec{s}_{dq} e^{j\theta} \tag{4.13}$$

and in matrix form

$$\begin{bmatrix} s_\alpha \\ s_\beta \end{bmatrix} = \begin{bmatrix} \cos\theta & -\sin\theta \\ \sin\theta & \cos\theta \end{bmatrix} \cdot \begin{bmatrix} s_d \\ s_q \end{bmatrix} \tag{4.14}$$

4.2.1 Definition of the System

In the literature, there are many ways of defining the synchronously rotating system. When used with a grid connected rectifier application, it is common to have $u_q = 0$, so that information about active current is given in i_d, and reactive current in i_q. The system with $u_d = 0$ is also often used. In motor application, there are more consensus about $d-q$, here i_d is the field producing current, and i_q is the torque producing current.

In this text, the definition where $u_q = 0$ is used for the grid rectifier, while the standard definition is used for the rotor inverter. It may seem inconsistent to use two definitions for basically the same thing. However, the reason for this is that the grid rectifier was implemented first, and defined as mentioned, whereafter the rotor inverter was implemented, and there it was most correct to use the other definition.

The following notation is used for the transformation of the rotor side to the dq-frame

$$\begin{bmatrix} u_{r\alpha} \\ u_{r\beta} \end{bmatrix} = \begin{bmatrix} \cos\theta & \sin\theta \\ -\sin\theta & \cos\theta \end{bmatrix} \cdot \begin{bmatrix} u_{rd} \\ u_{rq} \end{bmatrix} \tag{4.15}$$

and the inverse transformation

$$\begin{bmatrix} u_{rd} \\ u_{rq} \end{bmatrix} = \begin{bmatrix} \cos\theta & -\sin\theta \\ \sin\theta & \cos\theta \end{bmatrix} \cdot \begin{bmatrix} u_{r\alpha} \\ u_{r\beta} \end{bmatrix} \tag{4.16}$$

4.3 Instantaneous Power

When defining the voltage and current in 2-phase systems (rotating and stationary), the power equations for both cases are the following

$$P = \frac{3}{2}(u_d i_d + u_q i_q) = \frac{3}{2}(u_\alpha i_\alpha + u_\beta i_\beta) \tag{4.17}$$

$$Q = \frac{3}{2}(u_d i_q + u_q i_d) = \frac{3}{2}(u_\alpha i_\beta - u_\beta i_\alpha) \tag{4.18}$$

for a system with $u_q = 0$, this simplifies the power equations to

$$P = \frac{3}{2} u_d i_d \tag{4.19}$$

$$Q = \frac{3}{2} u_d i_q \tag{4.20}$$

4.4 Positive, Negative and Zero Sequence

In an unsymmetrical three phase system, the vectors can be split into:

- Positive sequence

- Negative sequence
- Zero sequence

Using (4.5), a balanced system with positive sequence, *abc* sequence, and RMS value U can be represented as a vector in the stationary reference $\alpha\beta$-frame as

$$\vec{u}_{\alpha\beta p} = \sqrt{3}Ue^{j\omega_1 t} \tag{4.21}$$

For a balanced system with negative sequence, *acb* sequence, the vector is according to

$$\vec{u}_{\alpha\beta n} = \sqrt{3}Ue^{-j\omega_1 t} \tag{4.22}$$

Equations 4.21 and 4.22 show that the positive system is equal to the symmetrical system and rotates in the same direction, while the negative system is rotating in the opposite direction of the positive system.

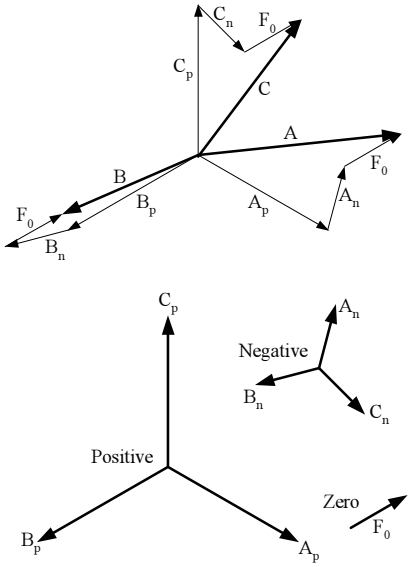

Fig. 4.3. Three phase system, split into positive, negative and zero sequence

When applying the same transformation on a balanced system with zero sequence it gives

$$\vec{u}_{\alpha\beta z} = 0 \tag{4.23}$$

So the zero sequence components are not represented in the stationary reference $\alpha\beta$-frame. The zero sequence contain information about the displacement from the zero point. In order to keep the information the extended $abc \rightarrow \alpha\beta 0$ transformation (4.3) are needed, though this gives no reduction in number of scalars. For the three phase systems, zero sequence will not be present. Unless there is a neutral conductor, in which the zero sequence can flow.

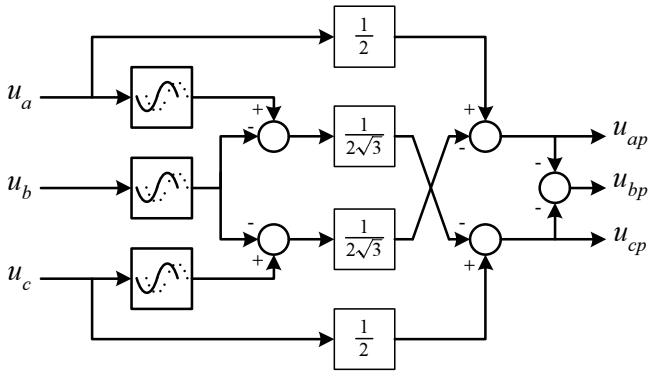

Fig. 4.4. Positive sequence computation

4.4.1 Extracting the Positive Sequence

Equation 4.24 is used to find the positive sequence for all three phases.

$$\begin{aligned}\begin{bmatrix} u_{ap} \\ u_{bp} \\ u_{cp} \end{bmatrix} &= \frac{1}{3}\begin{bmatrix} 1 & a & a^2 \\ a^2 & 1 & a \\ a & a^2 & 1 \end{bmatrix} \cdot \begin{bmatrix} u_a \\ u_b \\ u_c \end{bmatrix} \\ &= \begin{bmatrix} \frac{1}{2}u_a - \frac{1}{2\sqrt{3}j}(u_b - u_c) \\ -(u_{ap} + u_{cp}) \\ \frac{1}{2}u_c - \frac{1}{2\sqrt{3}j}(u_a - u_b) \end{bmatrix}\end{aligned} \tag{4.24}$$

where $a = e^{j\frac{2\pi}{3}} = -\frac{1}{2} + j\frac{\sqrt{3}}{2}$.

A practical implementation of this requires a filter with a 90° phase shift and constant gain. This can accomplished by using a Hilbert transformation [12]. The Hilbert transformation can be implemented as a high order FIR filter, and the rest is simple calculations, see figure 4.4.

5

Doubly Fed Induction Generators

The doubly fed induction generator (DFIG) is, as the name indicates, an induction generator where both stator and rotor terminals are available for power flow. When the machine works as a generator, the power flow in the machine is as shown in Fig. 5.1, where input is mechanical power. The active power transmitted to the grid is the sum of stator power P_s

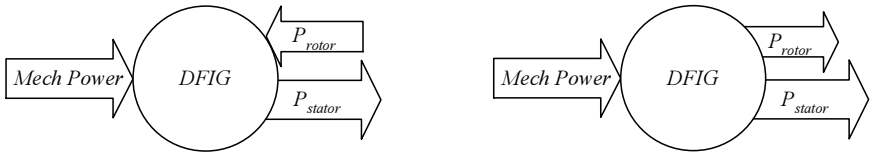

(a) $\omega < \omega_0$ (b) $\omega > \omega_0$

Fig. 5.1. Power flow of DFIG below and above synchronous speed.

and rotor power P_r, assuming the power inverter is loss less, $P_r = P_{grid}$. P_{grid} is the active power from the grid side converter.

The total power of the loss less system is simply the sum of stator and rotor power

$$P_{total} = P_s + P_{grid} \tag{5.1}$$

The active power from the rotor is proportional to the slip s of the generator

$$P_r = -s \cdot P_s \tag{5.2}$$

where the slip here is defined as

$$s = \frac{\omega_s - \omega_r}{\omega_s} \tag{5.3}$$

5.1 Classification of DFIG

In the literature, many different kinds of DFIGs have been presented and many of are also used in practice. DFIGs can be grouped into brushed or brushless, and then again into other subgroups. Hopfensperger and Atkinson have made a classification of the different types [13].

5.1.1 Standard DFIG

The standard DFIG is a wound rotor generator with slip-rings for the rotor circuit. Fig. 5.2 shows a principle diagram of the setup. The stator circuit is connected to the grid, while the rotor circuit is connected to a frequency converter, which is then connected to the grid [14]- [18].

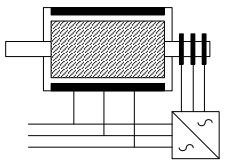

Fig. 5.2. Principle schematics of a standard DFIG.

This type of generator is referred to as DFIG in the rest of the thesis. Other types mentioned here will not be covered in more detail.

5.1.2 Cascaded Doubly Fed Induction Generator (CDFG)

The cascaded DFIG consist of two doubly fed induction machines, connected mechanically and electrically through the rotor. The stator terminals of one side are connected directly to the grid, while the other stator is connected to a frequency converter, see Fig. 5.3.

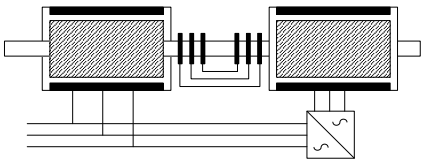

Fig. 5.3. Principal schematics of a cascaded DFIG.

The rotor voltage of the two machines are equal. The machine connected to the converter controls the other machine. This setup is not practical, since it does not give any advantages compared to the standard solution, while it uses an extra machine. The losses from this setup are expected to be higher than for the standard solution, due to the larger number of windings [13].

Single-Frame Cascaded Doubly Fed Induction Generator (S-CDFG)

The single-frame cascaded doubly-fed induction generator uses a single frame instead of two separate frames. Although this machine is mechanically more robust than the dual framed, it still suffers from comparatively low efficiency [13].

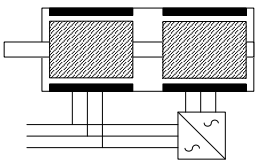

Fig. 5.4. Principal schematics of a single-frame cascaded DFIG.

5.1.3 Brushless Doubly Fed Induction Generator (BFDG)

The brushless doubly fed induction generator is a single frame machine with two stators using the same slots and sharing a common magnetic circuit. One winding is used for power and the other for control. In order

to avoid transformer coupling between the two windings, they must have a different number of pole pairs.

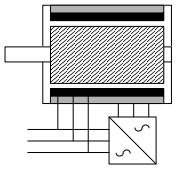

Fig. 5.5. Principal schematics of a brushless DFIG.

To avoid unbalanced magnetic pull on the rotor, the difference in pole pair numbers must be higher than one [19]. The number of pole pairs in the rotor must equal the sum of pole pairs of the two stator windings [19].

5.1.4 Doubly-Fed Reluctance Generator (DFRG)

The doubly fed reluctance generator has the same stator as the BFDG, but instead of a cage rotor it uses a reluctance type rotor, with the same constraints as for the BFDG [19]. This machine has almost the same equivalent diagram as the DFIG [20].

6

Induction Generators

The equations for a doubly fed induction machine and a normal squirrel cage machine are indentical, except that the rotor voltage is different from zero in the DFIG, while it is zero in the squirrel cage machine due to the short circuit of the rotor.

This chapter covers the equations used together with the induction machines. For a more in-depth discussion of the topic, the reader should consult an electrical machinery textbook [21], [22] or [23].

In the following equations, many of the variables are functions of time, but are written without their time variable, e.g. the stator current $i_{as}(t)$, will be displayed as i_{as}.

6.1 Induction Generator Equations

The stator voltage equations in stationary reference frame are

$$u_{as} = R_{as} i_{as} + \frac{d\psi_{as}}{dt} \tag{6.1a}$$

$$u_{bs} = R_{bs} i_{bs} + \frac{d\psi_{bs}}{dt} \tag{6.1b}$$

$$u_{cs} = R_{cs} i_{cs} + \frac{d\psi_{cs}}{dt} \tag{6.1c}$$

Likewise for the rotor voltage equations, they are given as

$$u_{ar} = R_{ar} i_{ar} + \frac{d\psi_{ar}}{dt} \tag{6.2a}$$

$$u_{br} = R_{br} i_{br} + \frac{d\psi_{br}}{dt} \tag{6.2b}$$

$$u_{cr} = R_{cr} i_{cr} + \frac{d\psi_{cr}}{dt} \tag{6.2c}$$

The turn ratio N_r/N_s between the rotor and the stator windings, has to be taken into account when working with an induction motor, since the motor is a coupled magnetic circuit and is related to the transformer. Equations (6.3a) to (6.3e) give the most common rotor quantities expressed at the stator side. They are denoted with superscript s for the stator side. The same can be found for stator quantities expressed at the rotor side. These are denoted with superscript r.

$$\left(\frac{N_s}{N_r}\right) u_r = u_r^s \tag{6.3a}$$

$$\left(\frac{N_s}{N_r}\right) \psi_r = \psi_r^s \tag{6.3b}$$

$$\left(\frac{N_r}{N_s}\right) i_r = i_r^s \tag{6.3c}$$

$$\left(\frac{N_s}{N_r}\right)^2 R_r = R_r^s \tag{6.3d}$$

$$\left(\frac{N_s}{N_r}\right)^2 L_{lr} = L_{lr}^s \tag{6.3e}$$

In most textbooks, when modelling induction machines, the rotor parameters are referred to the stator. For slipring machines the rotor terminals are available and rotor voltages and current can be measured. For the machine used in this project the ratio is $\frac{N_r}{N_s} = \frac{v_s}{v_r} = \frac{400V}{1600V} = 0.25$.

Transforming a rotor quantity to the stator side, when working with a squirrel cage motor is easily done. The same for a DFIG machine raises some questions, e.g. if the rotor voltage u_r is transformed to stator side. Connecting the rotor to a converter supplying the power to the grid, where the stator is also connected. Then the voltages from the two different systems get mixed. The conclusion to this problem is that all parameter are expressed at the side where they belong, except the magnetizing induc-

tance L_m that is in between the rotor and the stator. In the following, L_m seen from the stator will be denoted L_m and from the rotor L_m^r, calculated as

$$\left(\frac{N_r}{N_s}\right)^2 L_m = L_m^r \tag{6.4}$$

$$L_r = L_{lr} + \left(\frac{N_r}{N_s}\right)^2 L_m = L_{lr} + L_m^r \tag{6.5}$$

$$L_s = L_{ls} + L_m \tag{6.6}$$

where L_{ls} is the stator leakage inductance, L_{lr} is the rotor leakage inductance and L_s is the stator inductance.

The stator and rotor flux linkages can be expressed as

$$\vec{\psi}_s = L_s\vec{i}_s + L_m\vec{i}_r^s e^{j\theta_r} \tag{6.7}$$

$$\vec{\psi}_r = L_r\vec{i}_r + L_m^r\vec{i}_s^r e^{-j\theta_r} \tag{6.8}$$

Using (6.1)-(6.2) together with (6.7)-(6.8), the voltage equations for the induction machine are shown as space vectors

$$\vec{u}_s = R_s\vec{i}_s + L_s\frac{d\vec{i}_s}{dt} + L_m\frac{d(\vec{i}_r^s e^{j\theta_r})}{dt} \tag{6.9}$$

$$\vec{u}_r = R_r\vec{i}_r + L_r\frac{d\vec{i}_r}{dt} + L_m^r\frac{d(\vec{i}_s^r e^{-j\theta_r})}{dt} \tag{6.10}$$

When employing the rules of differentiation, the voltage equations becomes

$$\vec{u}_s = R_s\vec{i}_s + L_s\frac{d\vec{i}_s}{dt} + L_m\frac{d\vec{i}_r^s}{dt}e^{j\theta_r} + j\omega_r L_m\vec{i}_r^s e^{j\theta_r} \tag{6.11}$$

$$\vec{u}_r = R_r\vec{i}_r + L_r\frac{d\vec{i}_r}{dt} + L_m^r\frac{d\vec{i}_s^r}{dt}e^{-j\theta_r} - j\omega_r L_m^r\vec{i}_s^r e^{-j\theta_r} \tag{6.12}$$

The stator and rotor equations (6.1) and (6.2) can be expressed in a two phase system using (4.2). This can be displayed in a single matrix

$$\begin{bmatrix} u_{\alpha s} \\ u_{\beta s} \\ u_{\alpha r} \\ u_{\beta r} \end{bmatrix} = \begin{bmatrix} R_s + pL_s & 0 & \frac{N_r}{N_s} pL_m^r \cos\theta_r & -\frac{N_r}{N_s} pL_m^r \sin\theta_r \\ 0 & R_s + pL_s & \frac{N_r}{N_s} pL_m^r \sin\theta_r & \frac{N_r}{N_s} pL_m^r \cos\theta_r \\ \frac{N_s}{N_r} pL_m \cos\theta_r & \frac{N_s}{N_r} pL_m \sin\theta_r & R_r + pL_r & 0 \\ -\frac{N_s}{N_r} pL_m \sin\theta_r & \frac{N_s}{N_r} pL_m \cos\theta_r & 0 & R_r + pL_r \end{bmatrix} . \begin{bmatrix} i_{\alpha s} \\ i_{\beta s} \\ i_{\alpha r} \\ i_{\beta r} \end{bmatrix} \tag{6.13}$$

where p is the differential operator.

Equation (6.13) can be shown in a synchronously rotating reference frame, rotating with the speed ω_g

$$\begin{bmatrix} u_{ds} \\ u_{qs} \\ u_{dr} \\ u_{qr} \end{bmatrix} = \begin{bmatrix} R_s + pL_s & -\omega_g L_s & \frac{N_r}{N_s} pL_m^r & -\frac{N_r}{N_s} \omega_g L_m^r \\ \omega_g L_s & R_s + L_s p & \frac{N_r}{N_s} \omega_g L_m^r & \frac{N_r}{N_s} pL_m^r \\ \frac{N_s}{N_r} pL_m^r & -\frac{N_s}{N_r} (\omega_g - \omega_r) L_m^r & R_r + pL_r & -(\omega_g - \omega_r) L_r \\ \frac{N_s}{N_r} (\omega_g - \omega_r) L_m^r & \frac{N_s}{N_r} pL_m^r & (\omega_g - \omega_r) L_r & R_r + pL_r \end{bmatrix} . \begin{bmatrix} i_{ds} \\ i_{qs} \\ i_{dr} \\ i_{qr} \end{bmatrix} \tag{6.14}$$

The torque equation for the induction machine in the synchronous rotating reference frame is given as

$$t_e = -\frac{3}{2} P L_m \vec{i}_s \times \vec{i}_r^s \tag{6.15}$$

$$= \frac{3}{2} P L_m (i_{qs} i_{dr}^s - i_{ds} i_{qr}^s) \tag{6.16}$$

or as the cross product between rotor current and stator flux linkage

$$t_e = -\frac{3}{2} P \frac{L_m}{L_s} \vec{\psi}_s \times \vec{i}_r^s \tag{6.17}$$

where $\vec{i}_r^s$ is the space phasor of the rotor current expressed in the stationary reference frame, but transformed to the stator side.

The mechanical equation for the machine is given by

$$t_e - t_{load} = J \frac{d\omega_r}{dt} \tag{6.18}$$

where t_e and t_{load} are the electrical and load torque, respectively, and J is the inertia.

Fig. 6.1 shows the steady-state equivalent diagram for the induction machine.

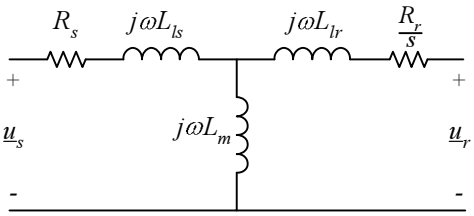

Fig. 6.1. Standard steady state equivalent diagram of an induction machine.

6.2 Turn Ratio and Modified *dq* Models

The equivalent in Fig. 6.1 can be reduced to a less complex model by introducing an arbitrary constant b. By doing so, one of the leakage inductances is eliminated in the equivalent digram. The voltage equations with the constant b are given as

$$\vec{u}_{dqs} = (R_s + L_s(p + j\omega))\vec{i}_{dqs} + bL_m(p + j\omega)\frac{\vec{i}_{dqr}}{b} \tag{6.19}$$

$$b\vec{u}_{dqr} = bL_m(p + j(\omega - \omega_r))\vec{i}_{dqs} + b^2(R_r + L_r(p + j(\omega - \omega_r)))\frac{\vec{i}_{dqr}}{b} \tag{6.20}$$

where b can be any value, except $b = 0$ or $b = \infty$. In Fig. 6.2, the constant b is used together with (6.19) and (6.20) for a general case.

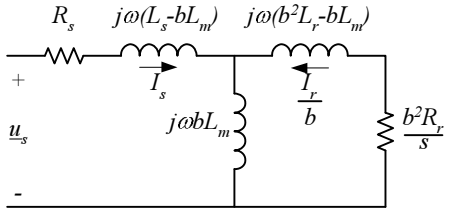

Fig. 6.2. Equivalent diagram for any values of b.

Selecting b so either the stator or the rotor leakage inductances cancel out, the equivalent diagrams are shown in Fig. 6.3 and 6.4. Grouping the inductances becomes very practical later when vector control of induction machines is discussed.

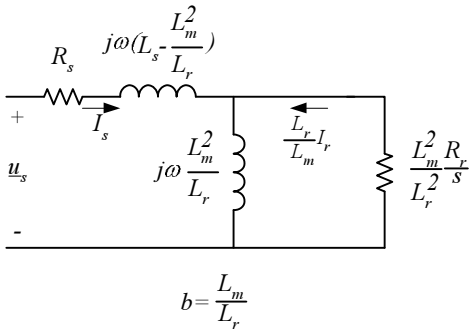

Fig. 6.3. Equivalent diagram where the rotor leakage inductance is not present in the rotor branch.

For rotor flux oriented control, Fig. 6.3 is useful. Fig. 6.4 is the same for stator flux oriented control.

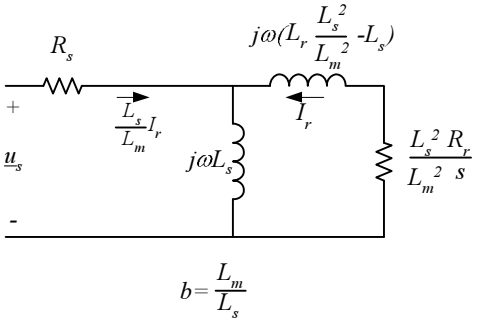

Fig. 6.4. Equivalent diagram where the stator leakage inductance is not present in the stator branch.

7

Inverter Topologies

This chapter gives a short overview of the different inverter topologies that apply to the field of variable speed wind turbines. It is not meant to be a complete list of all published topologies. All topologies mentioned here are voltage source inverters (VSI), oppose to a current source inverter (CSI). As mentioned previously, the type of generator is not limited to an AC generator. Basically inverters can be grouped into conventional 2-level inverter or multilevel inverters.

All the topologies are presented with a standard type switch. Different types of power electronic switches can be used, though the Insulated Gate Bipolar Transistor (IGBT) is the most commonly used power electronic switch together with 2-level topologies and AC-voltages below 1kV. The Integrated Gate Commutated Thyristor (IGCT) or other medium/high voltage self-commutated switches are often used with multilevel inverters [24]. Which type of switch should be used with the different topologies, depends on voltage, current and other parameters.

At the beginning of this Ph.D. project a DFIG machine with medium voltage rotor was still a possibility. Today most generator manufactures do not recommend rotor voltages above 1000 V due to insulation of the slip rings. With this in mind, the use of a 3-level inverter together with a DFIG system may not be the optimal solution. It was also important that the inverter topology could be used in a full speed range system (p16). For such a system, the multilevel inverter is very competitive due to the

high power level used in modern wind turbines. These considerations had an influence on the studied topologies.

7.1 2-level Inverters

For three-phase systems the most widely used inverter topology is the 2-level inverter, consisting of 3 half-bridge inverters with a common DC-capacitor.

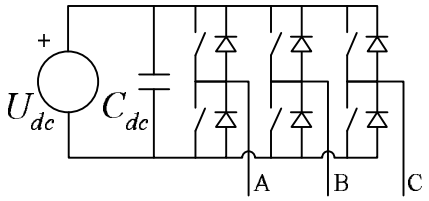

Fig. 7.1. 2-level inverter

This type of inverter can produce an output voltage to each phase that is either connected to the negative side of the DC-link or to the positive side, thus the name 2-level inverter. When using a 2-level inverter, each switch must as a minimum be able to withstand the DC-link voltage U_{DC}, which is the voltage over the non-conducting switch, when the other switch is conducting.

There are some drawbacks to this inverter type. Because the inverter must switch with relatively high frequency, the switching losses are much higher than the devices conduction losses. This applies in particular to large MW inverters. Mega Watt inverters will probaly be the size used in future DFIG wind turbines, and definitely the type used in full scale inverter turbines. Other problems include high dV/dt and voltage surges due to switching. This may cause motor/generator bearing current, dielectric stresses and corona discharges [25].

7.2 Resonant DC Link Inverters

Divan [26] presented this topology in 1986, and since then many new types have been proposed e.g. [27]. The resonant DC link uses one resonant circuit to provide soft switching for the entire converter, see Fig. 7.2. The DC link is forced to oscillate, so the resonance circuit is located on the DC link side and not on the load side, since only one resonant circuit is required instead of one for each phase.

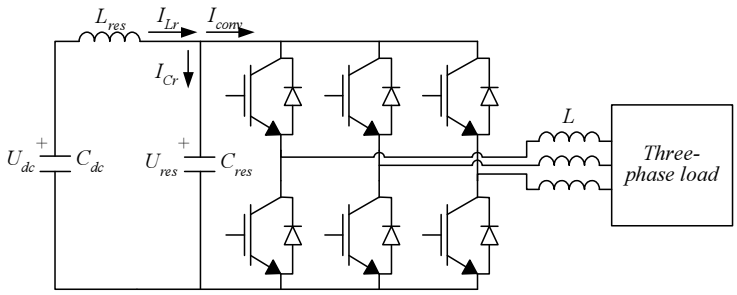

Fig. 7.2. Resonant DC-link converter

The idea with the resonant converter is that ideally the converter should only change state at zero link voltage. The resonant circuit is formed by L_{res} and C_{res}, where the resonant capacitor is many times smaller than the DC link capacitor C_{dc}. The resonant link voltage swings between zero and twice the DC link voltage, which means that the voltage rating of the switches has to be higher. The modulation strategy for this topology requires that the resonance frequency is much higher than the switching frequency.

7.3 Multilevel Inverters

In the literature, three topologies for multilevel inverters have been presented: the cascade inverter, the neutral point clamped inverter, and the flying capacitor inverter.

7.3.1 Cascade Multilevel Inverters

The cascaded multilevel inverter is often in the literature called a H-bridge, due to the "H" formed by the four switches in the diagram. Each switch has an anti-parallel diode. One single H-bridge can form three different voltage levels, by switch combinations. Fig. 7.3 shows a 5-level single phase

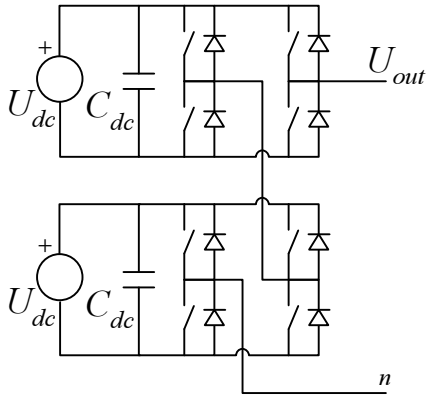

Fig. 7.3. 5-level H-bridge inverter single phase

inverter based on two H-bridges [28]. To construct a three phase inverter requires 3 times of that shown in the figure. Each voltage source/capacitor has to be electrically isolated from the rest, so the complexity of the system is high. The number of output phase voltage levels in a H-bridge inverter is defined by $m = 2n + 1$, where n is the number of DC sources.

7.3.2 Neutral Point Clamped Inverters

The Neutral Point Clamped (NPC) inverter was first proposed by Nabae et. al. [29]. Since then many publications have been based on this topology. The NPC consists of four switches, each with a free wheeling diode and two clamping diodes, see Fig 7.4.

The principle of the NPC inverter is that half of the switching elements are turned on, the other half are turned off. For a 3-level topology, either s1+s2, s2+s3 or s3+s4 are on to generator positive, zero or negative output, respectively. Each active device is only switched once every

cycle. As with the 2-level topology, each switch is required to block one voltage level (C_{dc}), or half the DC-link voltage, for the 3-level case. The clamping diodes (DC) on the other hand requires different voltage ratings, depending on their location. Fig. 7.4 shows that with s3+s4 conducting diode dc2 must block the upper DC source, only one source. For one level higher, the corresponding situation would require a blocking of two voltage levels. If the inverter is designed such that each clamped diode has the same voltage rating as the free wheeling diodes, some of the clamping diodes will require a series connection of 2 or more diodes depending on the number of levels, see Fig. 7.5(a).

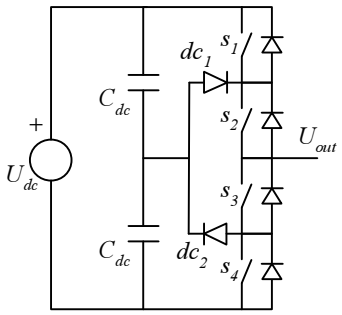

Fig. 7.4. 3-level Neutral Point Clamped inverter single phase

A method to avoid the series connection of diodes in five or more level inverters has been presented by Yuan and Barbi [30]. With this topology are both the switches and the clamping diodes clamped. A detailed description of this topology will not be covered here. The diagrams of a traditional 7-level NPC and the modified NPC are shown in figure 7.5.

7.3.3 Flying Capacitor Multilevel Inverter

The flying capacitor topology was presented by Meynard and Foch [31]. Fig. 7.6 shows the schematics of a 3-level flying capacitor, but this can be expanded to higher levels.

The voltage level of the DC sources must have the following values,

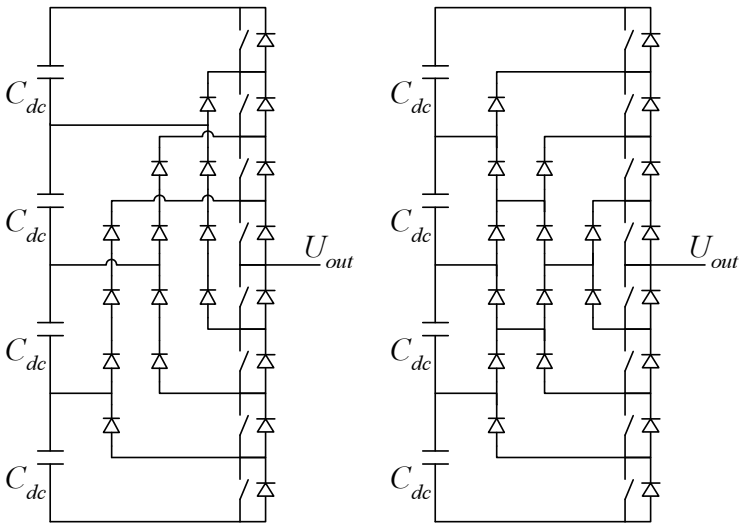

(a) Standard NPC (b) Modified NPC

Fig. 7.5. Two different types of 7-level NPC with the same number of diodes, single phase

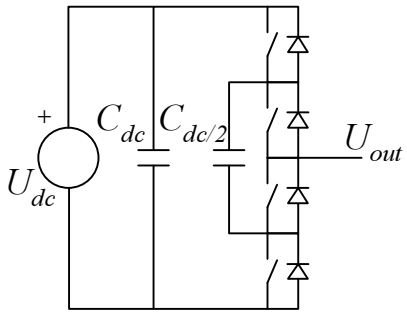

Fig. 7.6. Three-level flying capacitor, single phase

$$U_{DCk} = \frac{kE}{n} \tag{7.1}$$

where n is the number of DC sources and $k = 0...n$.

The control system of the inverter has to maintain the relation given in (7.1). If this is fulfilled the maximum voltage across each switch is U_{DC}/n.

7.3.4 The Hybrid Multilevel Inverter

The NPC inverter and the H-bridge inverter described above all have two or more DC levels. The NPC uses a stacked DC-capacitor battery and the H-bridge uses a single capacitor battery connected to the H-bridge. The voltage level on each bridge is the same in steady state, unless there is a problem with stability.

In 1998, Manjrekar and Lipo presented a new topology, a hybrid multilevel inverter [32]. The hybrid multilevel inverter is based on the H-bridge, but instead of connecting H-bridges with the same DC-voltage, they proposed a concept using a binary combination of the voltage levels.

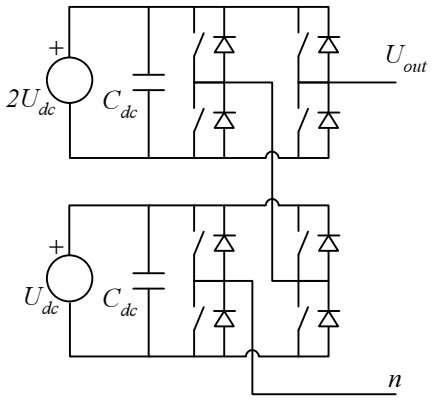

Fig. 7.7. 7-level hybrid H-bridge inverter single phase

An example could be an inverter with two H-bridges. The first bridge uses IGCTs with a low switching frequency and a DC link voltage of 3 kV. The second bridge is made of IGBTs with a high switching frequency and 1.5 kV at the DC link. By doing this, the output phase voltage level is from zero to 4.5 kV. The high frequency of the IGBT bridge makes it possible to reduce the harmonic distortion without having to switch the IGCT bridge that often. This of course reduces the losses significantly, since commutation losses for the IGBTs are less than for the IGCTs.

7.4 DC-balancing

When using several DC sources, series connected or isolated, voltage balancing will always be an issue. The problem evolves when the net energy to one DC source is different from the net energy to the other sources. The voltage across that DC source or capacitor will then either raise or drop from its intended value. In order to maintain the same voltage, the real power flow into a capacitor must be the same as the real power flow out of a capacitor. As it will be shown in chapter 8, the use of multilevels inverter gives a series of redundant switching vectors. The voltage on the output terminals is the same, but produced from different switching vectors, and the energy comes from different DC sources.

In an ideal system with large capacitors and complete symmetrical load, DC-balancing is not a problem. Coverage of this topic will continue in the next chapter on modulation techniques (see page 61).

7.5 Comparison of different multilevel topologies

Each of the different topologies has its advantages and disadvantages some of which have been covered above. Another approach to comparing topologies could be by making a simple component count [32]. The number of different components that are used in a three phase 7-level inverter is listed in Table 7.1. The table shows that the most optimal topology is the Hybrid H-bridge. It uses fewer switches than the NPC inverter and the same number of DC-busses. A comparison of the DC-busses is difficult since the NPC inverter uses a number of series connected DC sources, whereas the

Table 7.1. Comparison of different multilevel topologies general

Topology	Switch elements	DC busses	Output levels
NPC	36	6	7
Flying Cap.	36	16	7
H-bridge	36	9	7
Hybrid H-bridge	24	6	7

Hybrid H-bridge uses two individual isolated DC sources for each phase. Table 7.2 lists the general number of components for any level inverter.

Table 7.2. Comparison of different multilevel topologies general

Topology	Switch elements	DC busses	Output levels
NPC	6N	N	N+1
Flying Cap.	6N	3N-2	N+1
H-bridge	12N	3N	2N+1
Hybrid H-bridge	12N	3N	2^{N+1}-1

Compared to a 2-level inverter, the conduction losses for a 3-level topology are based on twice as many conducting switches plus clamp diodes. For the same phase voltage, however, the rated voltage for each switch in the 3-level topology can be approximately half of that the rated voltage required for the 2-level topology.

Studies of the inverter system together with a DFIG machine [33] have shown, that for the grid side inverter, the 3-level inverter has fewer losses when taking the line filter into account. For the rotor inverter, however, losses were significantly higher for the 3-level than for the 2-level. This comparison is made for IGBTs with the same voltage rating for both the 2- and the 3-level. If these studies had been based on the appropriate voltage ratings, the conducting losses of the 3-level would have been lower. Other studies support this theory [34].

7.6 Selection of inverter topology

The topology selected for implementing in the laboratory model is the 3-level NPC inverter. This decision was made before the publication of [33].

There were many reasons for choosing the NPC inverter. One of the main reasons was the possibility of increasing voltage level well above that which was realistic in 1999 with a 2-level IGBT based inverter. The simplicity of the NPC, compared to the normal H-bridge was also a factor. The hybrid H-bridge solution would have been an option if this topology was not patented (PCT WO9941828-A1).

8

Modulation

Conversion of DC power to AC power has to be performed in the switched mode. This can be done by temporary connection of power semiconductors with fast repetition, which enable a fast and highly efficient electronic control. The modulation of the three phases of a motor drive or a grid connected inverter can most simply be done by using a 2-level inverter as shown in Fig. 8.2(a)a. The desired current waveform can be achieved by controlling the changing of the duty cycles sinusoidally with time. This is the technique called Pulse Width Modulation (PWM).

The modulation strategy is an important factor for the performance of the power converter. Research has been done in the field of modulation technique with a focus on reducing the switching frequency, without increasing the distortion of the current [35].

When considering the performance of a given modulation technique the harmonic currents are used to get the loss factor. The harmonic currents are:

$$I_{h,rms} = \sqrt{\frac{1}{T}\int_T \left[i(t) - i_1(t)\right]^2 dt} \tag{8.1}$$

where $i(t)$ and $i_1(t)$ are the total current and the fundamental current, respectively. The loss factor is

$$d^2 = \frac{I_{h,rms}^2}{I_{h,rms,sixstep}^2} \tag{8.2}$$

The loss factor is independent of the load induction due to normalization with the harmonic distortion of the sixstep operation.

In the following, the main focus is on carrier-based modulation, especially the suboscillation PWM and the space vector method, the suboscillation is a phase modulation technique, while space vector works with the voltage space vector.

8.1 Suboscillation PWM

Before signal processors and micro controllers became cheap enough to be used together with PWM unit, the most commonly used modulation principle was the carrier based PWM. Each phase needs an individual carrier modulator, whereas the triangular carrier can be shared. The carrier signal is divided into two subcycles with duration $T_0 = \frac{f_s}{2}$. During each subcycle, every half-bridge will switch once, and then be switched back in the next subcycle.

The frequency modulation ratio is defined by

$$m_f = \frac{f_s}{f_1} \tag{8.3}$$

where f_1 is the fundamental frequency of the inverter output voltage.

The harmonics in the inverter output voltage are located as sidebands centered around the switching frequency f_s, and multiples there of [3]. The following is valid for $m_f \geqq 9$.

The frequency of the voltage harmonics is

$$f_h = (jm_f \pm k)f_1 \tag{8.4}$$

where h is the harmonics order, k is the sideband number and j times the frequency modulation ratio m_f. The different harmonics are given as

$$h = j(m_f) \pm k \tag{8.5}$$

If j is even, there exist only harmonics of odd values of k, while for odd values of j there exist only harmonics of even values of k.

For $m_f < 9$, subharmonic components can occur if there is no synchronization between the carrier and the reference signals.

The limitation of the amplitude of the converted AC signal is given by

$$U_{max} = \frac{4}{\pi}\frac{U_{dc}}{2} \tag{8.6}$$

When the modulation increases to $U_{max} = \frac{2}{\pi}U_{dc}$, the output signal of the inverter is a square-wave. This is called $U_{max,sixstep}$ in the literature. That is the absolute maximum possible voltage.

The modulation index is defined with respect to $U_{max,sixstep}$ as:

$$m = \frac{|U_{ref}|}{U_{max,sixstep}} = \frac{\pi}{2} \cdot \frac{U_{ref}}{U_{dc}}, \quad 0 \leq m \leq 1 \tag{8.7}$$

For the normal carrier modulation, the amplitude of the carrier should not exceed the amplitude of the reference signal, U_{ref}. This gives a $m_{max} = \frac{\pi}{4} = 0.7854$.

The upper graph in Fig. 8.1 shows the carrier and one phase with maximum amplitude. The lower graph shows the output signal.

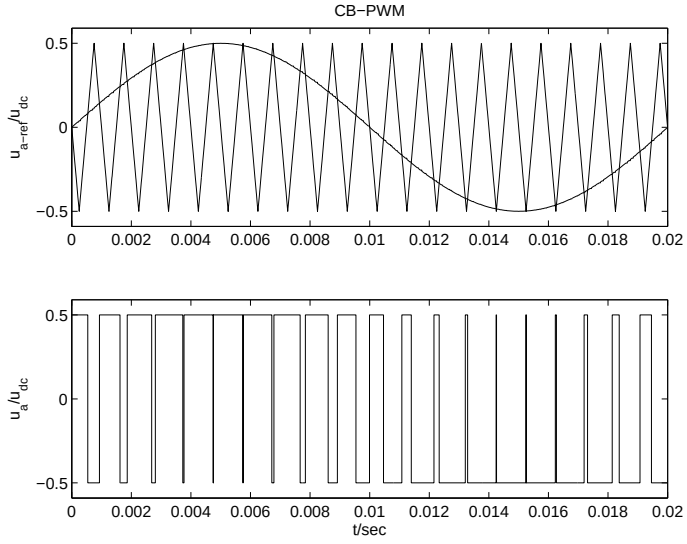

Fig. 8.1. CB-PWM with m_i =0.7854, $m_f = 20$

8.2 Space Vector Modulation

With the space vector modulation (SVM) technique the reference voltage is treated as a space vector $\vec{u}_{ref}$ instead of three scalers. The space vector is rotating in the complex plane as shown in Fig. 8.2(b). With a three phase 2-level voltage source inverter, see Fig. 8.2(a), there are eight switching states, six active states ($\vec{u}_1$ to $\vec{u}_6$) and 2 zero states ($\vec{u}_0$ and $\vec{u}_7$), see Fig. 8.2(b). The polygon is divided into 6 sectors. The active vectors can be represented by:

$$\vec{u}_k = \tfrac{2}{3} U_{dc} e^{j(k-1)\frac{\pi}{3}} \qquad k = 1, \ldots, 6 \tag{8.8}$$

where U_{dc} is DC-link capacitor voltage.

$\vec{u}_{ref}$ is defined as the mean space vector over one switching period T_s. Assuming the switching period is sufficiently small, $\vec{u}_{ref}$ can be considered a constant during the interval of the switching. The principle of space vector modulation is based on this assumption, since the switching pattern is a weighted average of three vectors; two active vectors and one of the zero vectors.

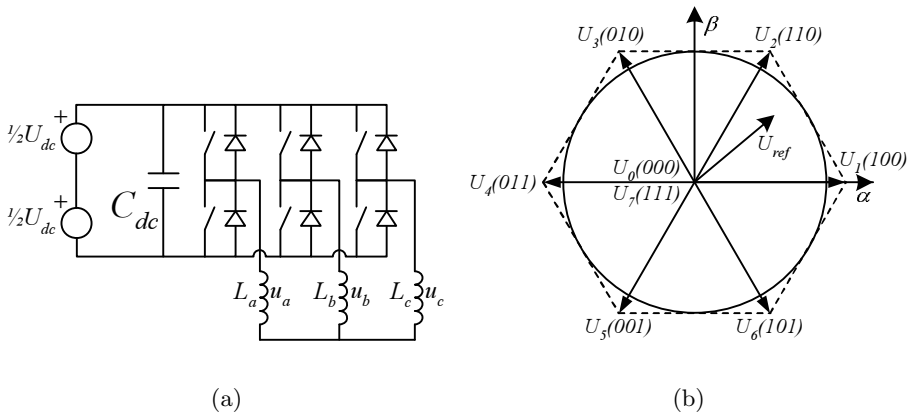

(a) (b)

Fig. 8.2. 2-level inverter and its space vectors

$$\vec{u}_{ref} = 2f_s \cdot (t_1\vec{u}_a + t_2\vec{u}_b) \tag{8.9}$$

$$t_0 = \frac{1}{2f_s} - (t_1 + t_2) \tag{8.10}$$

where $\vec{u}_a$ and $\vec{u}_b$ are the two switching vectors adjacent in space to $\vec{u}_{ref}$. The dwell time at each vector is given by

$$t_1 = \frac{1}{2f_s}\vec{u}_{ref}\frac{3}{\pi}\left(cos\left(\alpha'\right) - \frac{1}{\sqrt{3}}sin\left(\alpha'\right)\right) \tag{8.11}$$

$$t_2 = \frac{1}{2f_s}\vec{u}_{ref}\frac{2\sqrt{3}}{\pi}sin\left(\alpha'\right) \tag{8.12}$$

$$t_0 = \frac{1}{2f_s} - (t_1 + t_2) \tag{8.13}$$

where α' is the angle α transformed to first sector, i.e. $\alpha' = \alpha \bmod \frac{\pi}{3}$.

To achieve the same properties for SVM as for suboscillation PWM, each half-bridge has to change state once in every subcycle. At the end of the cycle, the switches are unchanged. Compared to the normal suboscillation PWM, the SVM utilizes the zero vectors at the beginning and end of every subcycle.

If α is less than 60°, the two non-zero vectors are $\vec{u}_1$ and $\vec{u}_2$. The switching sequence then becomes

$$\vec{u}_0\left\langle t_0/2\right\rangle \rightarrow \vec{u}_1\left\langle t_1\right\rangle \rightarrow \vec{u}_2\left\langle t_2\right\rangle \rightarrow \vec{u}_7\left\langle t_0/2\right\rangle \rightarrow \tag{8.14a}$$

$$\vec{u}_7\left\langle t_0/2\right\rangle \rightarrow \vec{u}_2\left\langle t_1\right\rangle \rightarrow \vec{u}_1\left\langle t_2\right\rangle \rightarrow \vec{u}_0\left\langle t_0/2\right\rangle \tag{8.14b}$$

Each transition from one vector to another requires that only one half-bridge switches state.

8.2.1 Modified space vector modulation

The modified space vector modulation is given by

$$\vec{u}_0\left\langle t_0/3\right\rangle \rightarrow \vec{u}_1\left\langle 2t_1/3\right\rangle \rightarrow \vec{u}_2\left\langle 2t_2/3\right\rangle \rightarrow \tag{8.15a}$$

$$\vec{u}_2\left\langle 2t_2/3\right\rangle \rightarrow \vec{u}_1\left\langle 2t_1/3\right\rangle \rightarrow \vec{u}_0\left\langle t_0/3\right\rangle \tag{8.15b}$$

The modified SVM uses one switching state less compared to the normal SVM. Since it only uses one zero vector at each subcycle, the on times are reduced to $\frac{2}{3}$ of those in the normal SVM. The modified SVM perform better than normal SVM if $m > 0.59$ [35].

Clearly, the largest possible voltage that may be achieved using normal SVM corresponds to the radius of the largest circle that can be inscribed within the hexagon in Fig. 8.2(b). The largest radius must be the radius to the midpoint of the outer line in each triangle

$$|\vec{u}_{ref}|_{max} = \frac{2}{3} U_{dc} \frac{\sqrt{3}}{2} = \frac{U_{dc}}{\sqrt{3}} \tag{8.16}$$

Using (8.16) together with the definition in (8.7), the maximum modulation index can be derived,

$$m_{max,cont} = \frac{|\vec{u}_{ref}|_{max}}{U_{max,sixstep}} = \frac{\frac{1}{\sqrt{3}} U_{dc}}{\frac{2}{\pi} U_{dc}} = \frac{\pi}{2\sqrt{3}} = 0.9069 \tag{8.17}$$

It has been shown that SVM and carrier modulation for two level inverters are the same, when appropriate zero sequence offset are added to the carrier of the carrier modulation [36]. The same applies to space vector modulation for multilevel inverters [37].

8.2.2 Overmodulation

When $m > 0.9069$, the modulation is no longer continuous, which for the CB-PWM means that the triangular carrier is below the reference voltage and some switching cycles are skipped.

Overmodulation can be grouped into two modes. Mode I is where the magnitude of the reference vector is kept inside the hexagon. This extends the modulation index to 0.952. Mode II is for 0.952<M<1. The overmodulation region can be seen in Fig. 8.3.

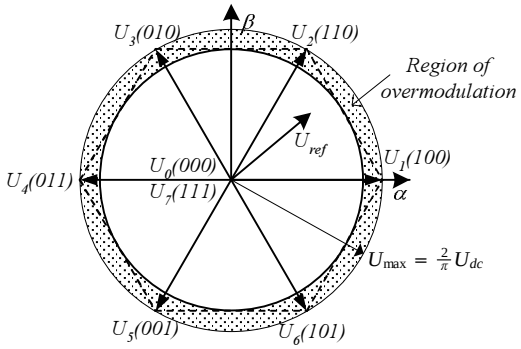

Fig. 8.3. Overmodulation

8.3 Discontinuous Pulse Width Modulation (DPWM)

Discontionuous modulation is formed by having a $\frac{\pi}{3}$ segment unmodulated. This segment can be phase shifted by the angle ψ. The first intersection point of $\vec{u}_a$ and $\vec{u}_b$ sets the angle ψ to zero [38]. The unmodulated segment is realized with a zero sequence offset. This definition of DPWM which gives an infinite possibility of modulations, are called Generalized DPWM, GDPWM [39]. One major advantage of DPWM is lower switching losses (average 33%).

Two special cases of GDPWM are DPWM1 ($\psi = 30°$) and DPWM3 ($\psi = 90°$), see Fig. 8.4. Their zero sequence can be calculated by (8.18) or (8.20).

$$U_{ZS\_DPWM1} = \text{sgn}(U_{off}) - U_{off} \tag{8.18}$$

$$U_{off} = \max[abs(U_a), abs(U_b), abs(U_b)] \tag{8.19}$$

$$U_{ZS\_DPWM3} = \text{sgn}(U_{off}) - U_{off} \tag{8.20}$$

$$U_{off} = \text{mid}[abs(U_a), abs(U_b), abs(U_b)] \tag{8.21}$$

In order to utilize the capabilities of a high performance drive with wide operating range, a combination of two or more PWM methods should be implemented with an on-line selection of the method as a function of the modulation index, m. In the low modulation region, SVM is superior to

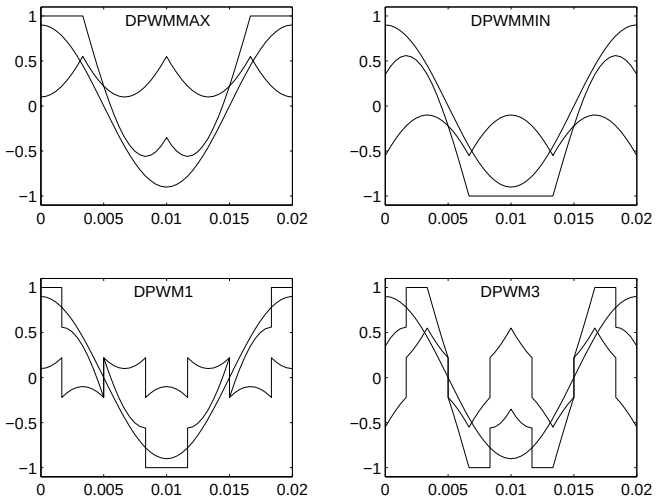

Fig. 8.4. Plot of four different discontinuous modulation schemes

most other methods, while in the higher modulation region DPWM is superior to SVM.

8.4 SVM and Multilevel Inverters

Fig. 8.2(b) showed the eight switching vectors for the 2-level inverter. The number of switching vectors for the n-level inverter increases with the cube of number of levels,

$$N_{vectors} = n^3 \tag{8.22}$$

In the 3-level inverter switching vectors consist of 3 zero vectors, 12 small vectors, 6 medium vectors and 6 large vectors, see Fig. 8.5. Each of the 12 small vectors has a redundant vector, so seen from the voltage produced, there is only 6 vectors with a redundant vector each, one drawing power from the upper DC-source and one drawing from the lower DC-source. This is discussed in detail on page 61. The medium vectors also draw power from only one DC-source, half of them from the upper source and the reminder from the lower source. However they do not have a redundant vector. The large vectors draw equal power from both DC-sources.

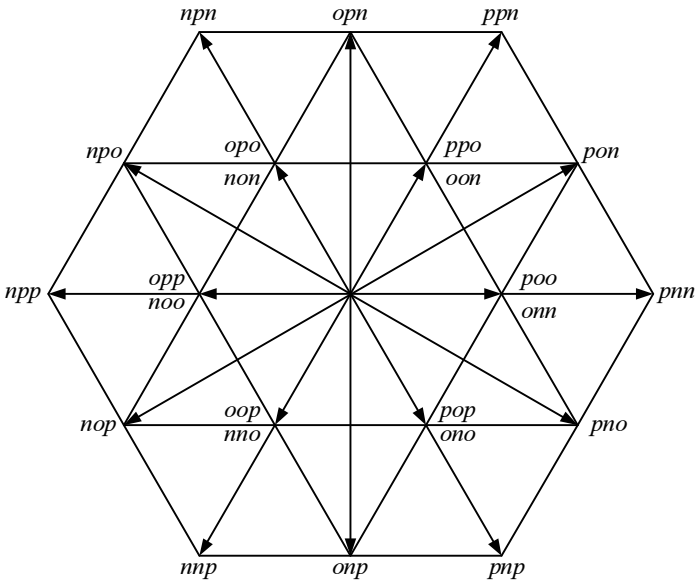

Fig. 8.5. Space vectors of a 3-level inverter

8.4.1 Implementation of SVM

In the laboratory setup, a space vector modulation for a 3-level inverter proposed by Celanovic and Boroyevich [40] has been implemented. This modulation algorithm is simple to implement and uses less computation time than other algorithms. The method uses a coordinate system with 60° displacement between the two axes g and h.

$$\left\{\vec{g}(u_{ab}, u_{bc}, u_{ca}), \vec{h}(u_{ab}, u_{bc}, u_{ca})\right\} = \left\{ \begin{bmatrix} U_{dc} \\ 0 \\ -U_{dc} \end{bmatrix}, \begin{bmatrix} 0 \\ U_{dc} \\ -U_{dc} \end{bmatrix} \right\} \tag{8.23}$$

Transforming $u_{\alpha\beta}$ to u_{gh} is done by using this matrix:

$$\begin{bmatrix} u_g \\ u_h \end{bmatrix} = \frac{2}{U_{dc}} \begin{bmatrix} \sqrt{3} & 0 \\ -\frac{1}{2} & -\frac{\sqrt{3}}{2} \end{bmatrix} \begin{bmatrix} u_\alpha \\ u_\beta \end{bmatrix} \tag{8.24}$$

Due to the fact that the switching states in the gh-coordinate system are normalized with (8.24), all the switching state vectors have integer

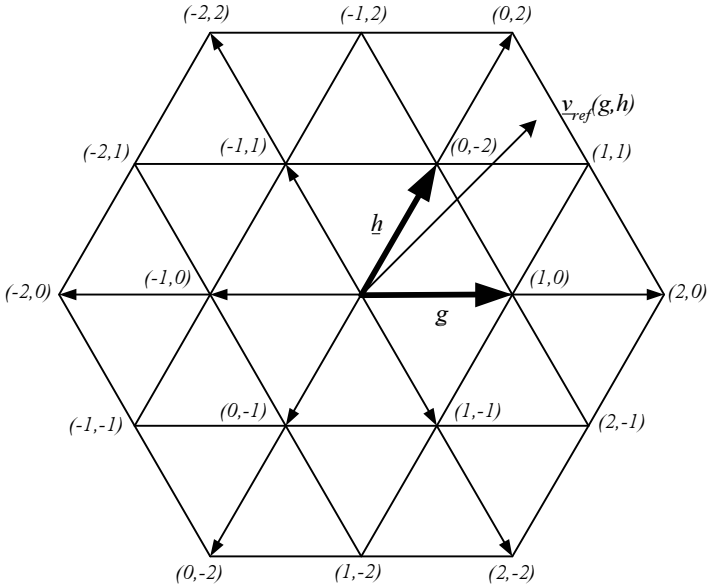

Fig. 8.6. 3-level hexagonal in (g,h)-coordinate system

values. A 2-level SVM has only 6 sectors to choose from, and the sector is selected by the angle α. With a 3-level SVM it becomes more complex. There are 24 sectors and not only the angle of the vector, but also the length of the vector determine the sector.

That the switching vectors are integers is used by the implemented method, to find the nearest three vectors to $\vec{u}_{ref}$. They are found by rounding u_{ref_g} and u_{ref_h} up and down to integer values, as follows

$$\vec{U}_{ul} = \begin{bmatrix} \lceil u_{ref_g} \rceil \\ \lfloor u_{ref_h} \rfloor \end{bmatrix} \tag{8.25a}$$

$$\vec{U}_{lu} = \begin{bmatrix} \lfloor u_{ref_g} \rfloor \\ \lceil u_{ref_h} \rceil \end{bmatrix} \tag{8.25b}$$

$$\vec{U}_{uu} = \begin{bmatrix} \lceil u_{ref_g} \rceil \\ \lceil u_{ref_h} \rceil \end{bmatrix} \tag{8.25c}$$

$$\vec{U}_{ll} = \begin{bmatrix} \lfloor u_{ref_g} \rfloor \\ \lfloor u_{ref_h} \rfloor \end{bmatrix} \tag{8.25d}$$

These four vectors form a parallelogram that divides into two triangles, the diagonal connecting the vectors $\vec{U}_{ul}$ and $\vec{U}_{lu}$. $\vec{U}_{ul}$ and $\vec{U}_{lu}$ are two of the three nearest vectors needed. The last one is found by evaluating the sign of the following equation,

$$0 < U_{ulg} + U_{ulh} - (g + h) \tag{8.26}$$

If the sign is positive, then the third nearest vector is $\vec{U}_{uu}$, and if not the vector is $\vec{U}_{ll}$. This method can be used for any $(n+1)-$level inverter. After identification of the nearest three vectors, what remains is to find the corresponding duty cycles.

For the 2-level inverter (8.9)

$$\vec{U}_{ref} = 2f_s \cdot (t_1\vec{u}_a + t_2\vec{u}_b) \tag{8.27}$$

was used. Similarly for the multilevel inverter we have

$$\vec{U}_{ref} = (d_1\vec{u}_1 + d_2\vec{u}_2 + d_3\vec{u}_3) \tag{8.28}$$

with the constraint that the sum of the duty cycles should be equal to one

$$1 = d_1 + d_2 + d_3 \tag{8.29}$$

The three vectors $\vec{u}_1$, $\vec{u}_2$ and $\vec{u}_3$ are substituted so $\vec{u}_1 = \vec{U}_{ul}$, $\vec{u}_2 = \vec{U}_{lu}$, and $\vec{u}_3 = \vec{U}_{ll}$ or $\vec{u}_3 = \vec{U}_{uu}$.

Because all the switching vectors have integer value coordinates, the duty cycles are simply the remaining fractional part of the $\vec{u}_{ref}$ coordinates,

$$d_{ul} = U_{ref_g} - U_{ll_g} \tag{8.30a}$$

$$d_{lu} = U_{ref_h} - U_{ll_h} \tag{8.30b}$$

$$d_{ll} = 1 - d_{ul} - d_{lu} \tag{8.30c}$$

if $\vec{u}_3 = \vec{U}_{ll}$, or

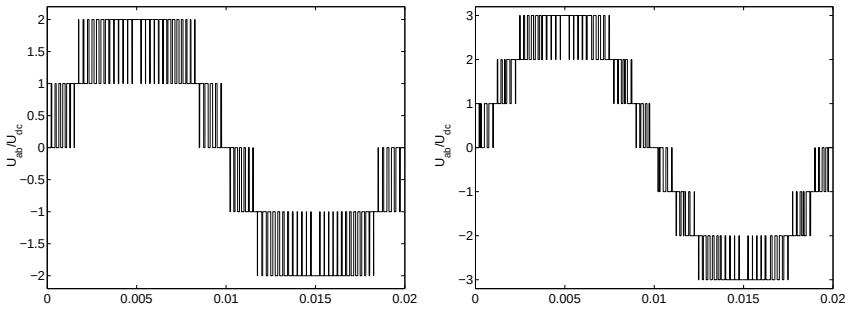

(a) 3-level (b) 4-level

Fig. 8.7. Phase-phase signal of 3-level and 4-level modulation, $F_s = 4kHz$

$$d_{ul} = -(U_{ref_h} - U_{ll_h}) \tag{8.31a}$$

$$d_{lu} = -(U_{ref_g} - U_{ll_g}) \tag{8.31b}$$

$$d_{uu} = 1 - d_{ul} - d_{lu} \tag{8.31c}$$

if $\vec{u}_3 = \vec{U}_{uu}$.

After selecting the nearest three vectors and their duty cycles, a transformation from the gh-coordinate system to a three phase system is necessary. The following expression does this transformation

$$\begin{bmatrix} u_a \\ u_b \\ u_c \end{bmatrix} = \begin{bmatrix} k \\ k-g \\ k-g-h \end{bmatrix}, \text{ where } k, k-g, k-g-h \in [0, n-1] \tag{8.32}$$

Take for example the gh-vector [1,-1]^T. This vector transforms to two redundant switching vectors [2,1,2] or [1,0,1]. Each of the two vectors are given the same outer voltage, but they draw energy from different DC-sources, so the DC-balancing algorithm most handle the selection of the proper switching vector.

In the laboratory setup, a look-up table [41] was used to select the switching vector. The table is printed in the appendix B. By using this table, the transformation in (8.32) is not needed. The switching states are stored as hexadecimal numbers in the table, where the 0 (negative)

equivalent switch is coded with #3, the 1 (zero) is coded with #6, and the 2 (positive) is coded with #C. The small vectors have a fourth digit hexadecimal numbers counted from right to left. This is used to tell which phase the neutral point current is drawn from.

Switch selection is based on this formula,

$$switch\_state = 7(g + h + 2) + (h + 2). \tag{8.33}$$

If the selected *switch_state* is a small vector, there are two switching combinations. The other switching combination is located at the address $switch\_state + 4$.

8.5 DC Neutral Point Balancing

As described earlier the use of multilevel inverters can cause balancing problems with the DC-levels. The following is valid for the 3-level inverter, but also applies to more levels.

There are a series of things to consider in order to balance the DC voltages. The SVM methods described above can be used in many ways to reduce the DC balancing problem [42] and [43]. Snubbers often have to be used together with high power switching devices due to the discharge of the snubber capacitor. A minimum on-time is introduced for the switching. This sets some constraints on how to select an optimal DC balancing. Since it is no longer possible to use vector combinations, with dwell time less than the minimum on-time.

Having back to back inverters that share the same DC-link and also the same neutral point, raises some questions about which inverter is reliable for the neutral point. Since reactive load leads to reduced neutral point control capability [44], the converter with the lowest reactive load should control the neutral point level. This depends on the specific working situation for the DFIG system. Using the redundant switching states for neutral point control might increase the harmonics due to nonsymmetrical harmonic voltage waveform [45]. Thus, neutral point control should not

be done by the grid side inverter unless the rotor side inverter is lagging power.

The laboratory setup uses snubber free switches. Whenever a redundant switch vector is selected, the neutral point level and the current polarity of the phase that affects the neutral point are monitored. This determines which of the two vectors that should be selected, called bang-bang dwell time control [43]. In the last column of Table B.1 in appendix B, the phase and direction the neutral point current comes from, are shown for the small vectors.

It is obvious that the closer the space vector amplitude is to the center of the hexagon, the easier DC balancing will be since it gives more on time for the small vectors. Large space vectors will give less on time to DC balancing. Low fundamental frequency operation results in slower neutral point swing [46], which is more difficult to control. Fortunately, low fundamental frequencies only occur at the rotor side converter. Having a low fundamental frequency at the rotor side, also means that the rotor voltage is low, hence the small voltage vectors are used for a large part of the duty cycle, which help stabilize the neutral point.

Under normal circumstances, the zero sequence is by nature of the SVM balanced. Thus without a neutral conductor, the zero sequence can not flow. Using the redundant switch vectors for neutral point balancing results in lack of control of the zero sequence injected in the phase voltage. The zero sequence will then flow even without a neutral conductor. With a back to back converter, it is obvious that when using the grid side inverter for DC balancing, the inverter will produce a zero sequence that will be reflected as 3rd, 9th, etc. harmonics. The same applies to the machine side, but here the appearance of a zero sequence is less critical, though it will have some effect on a DFIG system, since the zero sequence then will appear in the stator current as well.

8.6 Dead time

When turning off large power electronic devices, there will be some storage effect. The storage time T_{st} is dependent on the current and the operating

temperature. In order to not get a short circuit through the inverter half-bridge when turning one switch off and the other one switch on, some dead time T_d is introduced. This requires that $T_d > T_{st}$. T_d should be large enough to constantly avoid a short circuit, or T_d can be a function of current and temperature plus a safety margin [47].

The effect of dead time depends on the current direction. For a positive load current, the turn-on of the upper switch will be delayed T_d and the turn-off will be delayed with T_{st}. Since $T_d > T_{st}$ the on time for the upper switch T_{on}, will be decreased by $T_d - T_{st}$. Likewise for the negative load current, the upper switch T_{on} will be increased by $T_d - T_{st}$. The dead time produces a nonlinear distortion of the average voltage vector trajectory. This distortion does not depend on the magnitude of the fundamental voltage and hence the effect is more inherent for lower voltage magnitudes i.e. in the lower speed range. Analysis shows that the dead time also depends on the magnitude of the fundamental during the dead time period [48].

Using a hardware solution to compensate for dead time effects gives a fast and simple solution, but it will not be able to consider the actual voltage during the dead time. Software solutions are better and various solutions have been proposed [48].

Eventhough snubber-less switches do not require a minimum on-time, it is advantageous to use some sort of minimum on-time. Short time duration switching states do not affect the output voltage. This is because the semiconductor switch requires some time to reach its on- and off-state, so the switch is barely turned on before it has to be turned off again, resulting of increased switching losses.

8.7 Hysteresis control

In order to use hysteresis control, a feedback of the current in each phase is essential. The principle of hysteresis control is to maintain the current within the hysteresis band. This is done with a nonlinear feedback loop with two level hysteresis comparators [49], see Fig. 8.8.

There are disadvantages to this modulation [35], such as

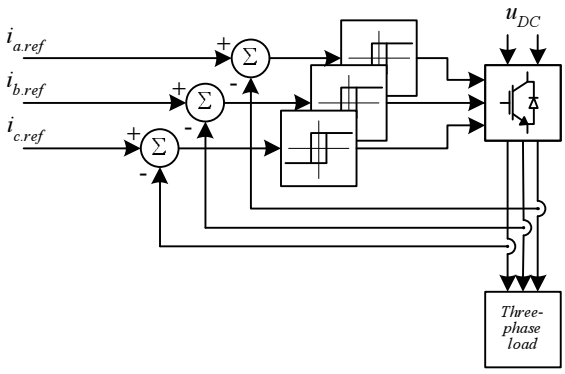

Fig. 8.8. Hysteresis current control

- Lack of communication between the individual hysteresis controllers and hence no strategy for generating zero voltage vectors.
- A tendency to lock into limit cycles of high switching frequency. This occur mainly at low fundamental frequency.
- Generation of subharmonic current components.
- The current is not strictly limited. The signal will leave the hysteresis band whenever the zero vector is turned on and the grid voltage vector (back EMF vector) has a component that opposes the previous active switching vector.
- The switching frequency of the hysteresis control is strongly dependent on the modulation index.

8.8 Sigma-Delta Modulation

Sgima-delta ($\Sigma\Delta$) modulation is often used together with resonance DC-link converters. The modulator uses the error between measured and reference voltage. This error is fed through an integrator and then on to a comparator with a hysteresis band equal to zero. When $\Sigma\Delta$-modulators are used with resonant DC-link converters, the signal must be latched until the resonant link voltage equals zero. This can be done by using another comparator to generate a clock signal to the latch when zero voltage oc-

curs [26] and [12]. Figure 8.9 shows a flow diagram of the $\Sigma\Delta$-modulator for one half-bridge.

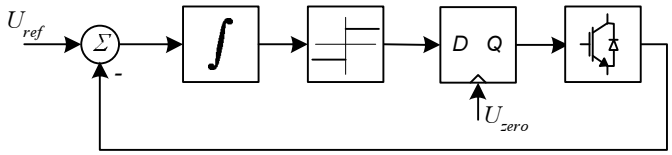

Fig. 8.9. Flow diagram of $\Sigma\Delta$-modulation for one bridge leg.

One disadvantage of the $\Sigma\Delta$-modulator is the switching frequency, F_s, is variable, so it can be difficult to design output filters for this type of converter. On the other hand, since there is no constant frequency, the switching noise is spread over a larger frequency interval, which might make it easier to comply with the international standards [9].

9

Vector Control of Induction Machines

Field orientation vector control was presented by Hasse [50] and Blaschke [51] in the late 1960s. The principle of vector control is based on the desire to control an AC motor in the same way as a DC motor.

9.1 DC Motor Torque Control

When controlling a DC motor two windings are available for control, the field winding and the armature winding. Construction of the DC motor can be made such that the two windings are orthogonal. The field winding maintains a stationary DC excitation. This excitation can also be implemented with permanent magnets. The armature winding is rotating and therefore supplied through a commutator. The current flowing in the armature ensures the armature MMF. The result of the orthogonality is that field flux is unaffected by the armature current.

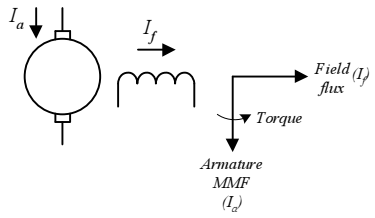

Fig. 9.1. Orientation of the field flux and armature MMF in a DC machine.

The torque equation for the DC machine is

$$T_e = \frac{P}{2}\frac{L_{af}}{L_f} \times \vec{\psi}_f \times \vec{i}_a \tag{9.1}$$

From (9.1) it follows that when the field flux vector and the armature MMF vector are orthogonal, the torque equation is reduced to

$$T_e = c \cdot \psi_f \cdot i_a \tag{9.2}$$

The field flux is controlled independent of the armature current, if the orthogonality is disturbed the two vectors are no longer independent.

9.2 AC Motor Torque Control

From the DC motor torque control, we have to follow some criteria, in order to have AC motor torque control [23]:

- Independently controlled armature current;
- Independently controlled or constant field flux;
- Independently controlled orthogonal angle between flux and MMF axes, to avoid interaction of the flux and the MMF.

If all three requirements are fulfilled, the torque instantaneously follows the current. If the requirements are only met in steady state, steady state torque control will result, while in transient periods, there will not be complete torque control.

A common feature of all vector controlled drives is that the modulus and phase angle of AC excitation are controlled hence the name “vector control”. The implementation of vector control requires an accurate flux-linkage estimation. If incorrect modulus and angle of the flux-linkage space vector are used, the decoupling of torque and flux is lost. This decoupling is, as mentioned above, required for vector control.

When using vector control, an important thing to consider is the reference frame for the flux vector. This frame follows the flux vector synchro-

nously. There are generally three possibilities for selecting the reference frame for the flux vector:

9.2.1 Stator Flux Oriented Control

The stator flux linkage is given by

$$\vec{\psi}_s = \int (\vec{u}_s - R_s \vec{i}_s) dt \tag{9.3}$$

where $\vec{\psi}_s$, $\vec{u}_s$ and $\vec{i}_s$ are expressed in the stationary reference frame. At low frequencies, the stator voltage becomes very small and the ohmic voltage drop is important. Thus an accurate value for the stator resistance is important for this method. Since the resistance varies with temperature, a thermal model may be needed. When using stator flux oriented control in a DFIG machine, there is no problem with low stator voltages since the stator voltage is kept by the grid. The torque equation is

$$t_e = c_s \left| \vec{\psi}_s \right| i^s_{sq} \tag{9.4}$$

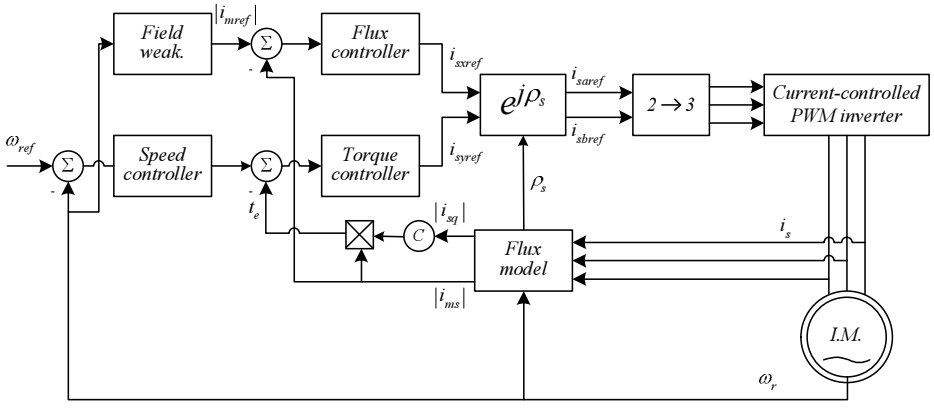

Fig. 9.2. Vector control in stator flux oriented control.

9.2.2 Rotor Flux Oriented Control

The rotor flux linkage can be obtained by applying appropriate modifications to the stator flux-linkage $\vec{\psi}_s$ as shown here

$$\vec{\psi}'_r = \frac{L_r}{L_m}\left(\vec{\psi}_s - \sigma L_s \vec{i}_s\right) \tag{9.5}$$

This model requires accurate knowledge of the motor inductances, which can be difficult since they vary with the saturation level. Figure 9.2 shows an example of rotor flux oriented control. The torque equation is

$$t_e = c_r \left|\vec{\psi}_r\right| i^r_{sq} \tag{9.6}$$

9.2.3 Magnetizing Flux Oriented Control

When selecting the magnetizing flux linkage, either a Hall sensor can be used to obtain the flux or the same approach as for the rotor flux-linkage can be used, where the flux is obtained from the stator flux-linkage $\vec{\psi}_s$ given by

$$\vec{\psi}'_r = \vec{\psi}_s - L_{ls}\vec{i}_s \tag{9.7}$$

where L_{ls} is the stator leakage inductance. The torque equation is

$$t_e = c_m \left|\vec{\psi}_m\right| i^m_{sq} \tag{9.8}$$

9.3 Magnetizing Loss Reduction

For a variable speed system with a stator fed inverter, the magnetizing losses can be reduced by running the generator on a flux that minimizes magnetizing losses in the generator. The DFIG system allows for at least two ways to reduce magnetizing losses. One way is to short circuit the stator of the generator at low power production, and get all the power out of the rotor. This setup works as a normal variable speed system with a shorted rotor. The only difference is that here it is the stator that is short circuited. Another way to reduce losses can be by having the stator Δ-connected at high power levels and Y-connected at low power levels.

9.4 DFIG Equations in Stator Flux Oriented Control

Stator flux oriented (SFO) control was implemented in the laboratory setup. The specific equations are therefore derived and presented here. In order to use SFO, a reference frame rotating synchronously with the stator flux linkage vector has to be employed. The angle of the frame with respect to the stationary frame α-axis is ρ_s.

$$\vec{i}_{s\psi s} = \vec{i}_s e^{-j\rho_s} \tag{9.9}$$

The subscript ψs means stator quantity in stator flux oriented control, adopted from [22]. In Fig. 9.3, the relationship between the stationary reference and the SFO frame is shown.

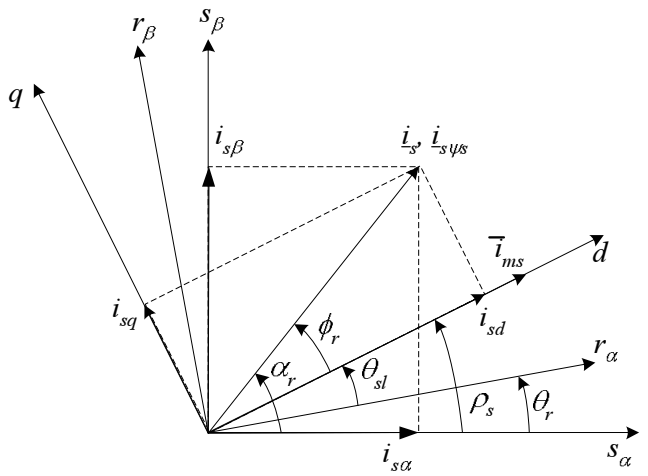

Fig. 9.3. Relationship between the stationary reference frame and the SFO frame.

The magnetizing current $\vec{i}_{ms}$ is given as

$$\vec{i}_{ms} = \vec{i}_{s\psi s}\frac{L_s}{L_m} + \vec{i}^{s}_{r\psi s} \tag{9.10}$$

With the magnetizing current, the torque is simple to get just from looking at Fig. 9.3, since the torque is the product of the magnetizing current and torque producing current. The torque producing current is

the orthogonal vector to the magnetizing current. So if angle ρ_s is correct, we have

$$t_e = \frac{3}{2} P L_m \left|\vec{i}_{ms}\right| i_{sq} \tag{9.11}$$

The stator voltage for the DFIG can be expressed by

$$\vec{u}_{s\psi s} = R_s \vec{i}_{s\psi s} + L_s \frac{d\vec{i}_{s\psi s}}{dt} + L_m \frac{d\vec{i}_{r\psi s}}{dt} + j\omega_{ms}(L_s \vec{i}_{s\psi s} + L_m \vec{i}_{r\psi s}) \tag{9.12}$$

By substituting (9.10) into (9.12), we get

$$\vec{u}_{s\psi s} = R_s \frac{L_m}{L_s}(\left|\vec{i}_{ms}\right| - \vec{i}_{r\psi s}) + L_m \frac{d\left|\vec{i}_{ms}\right|}{dt} + j\omega_{ms} L_m \left|\vec{i}_{ms}\right| \tag{9.13}$$

If the stator time constant is $T_s = L_s/R_s$, the differential equation (9.13) of the stator can be written as

$$T_s \frac{d\left|\vec{i}_{ms}\right|}{dt} + \left|\vec{i}_{ms}\right| (1 + j\omega_{ms} T_s) = u_{s\psi s} \frac{L_s}{R_s L_m} + \vec{i}_{r\psi s} \tag{9.14}$$

If the space vectors are split into two-axis components, the equations are

$$T_s \frac{d\left|\vec{i}_{ms}\right|}{dt} + \left|\vec{i}_{ms}\right| = u_{sd} \frac{L_s}{R_s L_m} + i_{rd} \tag{9.15a}$$

$$\omega_{ms} T_s \left|\vec{i}_{ms}\right| = u_{sq} \frac{L_s}{R_s L_m} + i_{rq} \tag{9.15b}$$

9.4.1 Rotor Voltage Equations for DFIGs

The rotor voltage for the DFIG can be expressed by

$$u_{r\psi s} = R_r \vec{i}_{r\psi s} + L_r \frac{d\vec{i}_{r\psi s}}{dt} + L_m \frac{d\vec{i}_{s\psi s}}{dt} + j(\omega_{ms} - \omega_r)(L_r \vec{i}_{r\psi s} + L_m \vec{i}_{s\psi s}) \tag{9.16}$$

By substitution of (9.10) into (9.16), and given that $\omega_{sl} = \omega_{ms} - \omega_r$ is the angular slip frequency

$$u_{r\psi s} = (R_r + \sigma L_r)\vec{i}_{r\psi s} + \frac{L_m^2}{L_s} p \left|\vec{i}_{ms}\right| + j\omega_{sl}(\frac{L_m^2}{L_s} \left|\vec{i}_{ms}\right| + \sigma L_r \vec{i}_{r\psi s}) \tag{9.17}$$

If (9.17) is split into the two-axis components, we get the two differential equations for the rotor current

$$\sigma T_r \frac{di_{rd}}{dt} + i_{rd} = \frac{u_{rd}}{R_r} + \omega_{slip}\sigma T_r i_{rq} - T_r(1-\sigma)\frac{d\left|\vec{i}_{ms}\right|}{dt} \tag{9.18a}$$

$$\sigma T_r \frac{di_{rq}}{dt} + i_{rq} = \frac{u_{rq}}{R_r} - \omega_{slip}\sigma T_r i_{rd} - \omega_{slip} T_r(1-\sigma)\left|\vec{i}_{ms}\right| \tag{9.18b}$$

where σT_r is the transient rotor time constant, $T_r = L_r/R_r$, and σ is the total leakage factor $1 - L_m^2/L_s L_r$. The rotor voltage equations (9.18) is applied to stator oriented flux control. Similar equations can be derived for rotor flux oriented control. The main difference is that instead of using the rotor parameter in the equations, stator parameters are used. This means that the stator time T_s constant will limit the response of the system in rotor flux oriented control, whereas for the stator flux oriented control it is T_r that is the time constant. The rotor voltage equation in the dq-reference frame is

$$u_{dr} = R_r i_{dr} + \sigma L_r \frac{di_{dr}}{dt} - \omega_{slip}\sigma L_r i_{qr} + L_r(1-\sigma)\frac{d\left|\vec{i}_{ms}\right|}{dt} \tag{9.19a}$$

$$u_{qr} = R_r i_{qr} + \sigma L_r \frac{di_{qr}}{dt} + \omega_{slip}(L_m\left|\vec{i}_{ms}\right| + \sigma L_r i_{dr}) \tag{9.19b}$$

Equation (9.18) shows that the induction generator, with respect to the rotor current, behaves as a first order delay system with the time constant σT_r. From (9.18) or (9.19) it follows that there is a cross coupling between the rotor currents along the selected d and q axes. However, the cross coupling can be eliminated by the decoupling voltage equations

$$u_{dr} = -\omega_{sl}\sigma L_r i_{qr} \tag{9.20a}$$

$$u_{qr} = \omega_{sl}\left(L_m\left|\vec{i}_{ms}\right| + \sigma L_r i_{dr}\right) \tag{9.20b}$$

Equation 9.20 assumes that the stator magnetizing current $\vec{i}_{ms}$ is constant. This assumption requires that the stator resistance R_s can be neglected and stator frequency is constant, i.e. constant grid frequency. This gives

$$|\vec{u}_s| = \omega_{grid} L_m \left|\vec{i}_{ms}\right| \tag{9.21}$$

assuming that $u_{qs} = 0$, $|\vec{u}_s| = u_{ds}$

$$\left|\vec{i}_{ms}\right| = \frac{u_{ds}}{L_m \omega_{grid}} \tag{9.22}$$

9.5 Control of Rotor Inverter

The two degrees of freedom this inverter has are used to control magnetizing current in the rotor circuit and the torque of the machine. This control requires measurements of the stator and rotor current, stator voltage and rotor position [15]. As already mentioned the stator flux (9.3) is stabilized by the grid. Therefore, the effect of stator resistance is limited and can be neglected. The voltage drop due to the resistance is less than one procent.

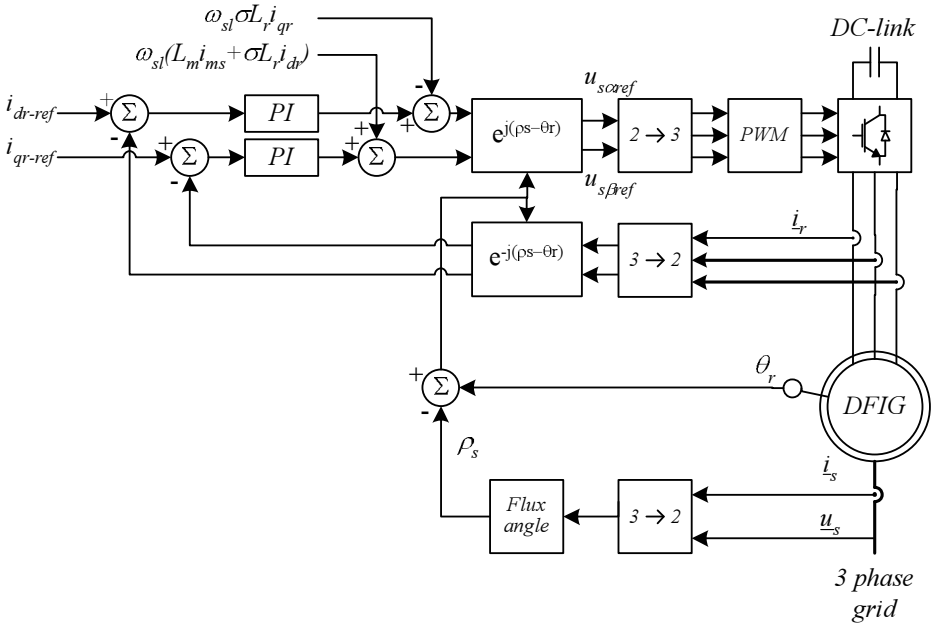

Fig. 9.4. Stator flux oriented vector control for the DFIG system

Figure 9.4 shows a diagram of the structure for the implementation of the stator flux oriented control. The feed forward terms in the upper part of the diagram are the decoupling equations (9.20). The control system is only shown with the control for the rotor current. Additional controllers can be added to the left side of the diagram, so that the active and reactive power can be controlled by means of the rotor current. If implemented, the direct current i_{dr} controls the reactive power and the active power is controlled by the quadrature current i_{qr}. If an extra PI-controller is added in front of the quadrature current i_{qr}, the quadrature current i_{qr} loop can be used in a speed controller instead.

9.6 Dynamics of the DFIG Vector Control

When keeping the flux constant in the machine by a constant magnetizing current, a fast torque response is possible. This is a well known characteristic of vector control for a stator fed induction machine. It means that the direct current has to be kept constant, while quadrature current can change momentarily. With the DFIG, on other hand, the stator is connected to the grid. The magnetizing current can be supplied through the stator or the rotor. The flux level is assumed to be nearly constant, with constant grid voltage. From (9.18) it follows that the time constant for both the direct and the quadrature current is σT_r. This means that changing the flow of reactive power from the inverter is as fast as changing the active power flow, see Fig. 15.9.

10

Control of the Grid Inverter

The grid connected inverter can be controlled with different principles. One is vector control, while another is amplitude-phase control [52]. Finally direct power control [53] is also a possibility, but this will not be covered here.

10.1 Vector Control

Vector control of a grid connected inverter is similar to vector control of a motor/generator. The grid itself can be modeled as a synchronous machine, with constant frequency and constant magnetization. Table 10.1 shows the functions of the control loops of the rotor side and grid side inverter vector control. Vector control gives two degrees of freedom split into a d- and q-component. The d-component is used to control the DC voltage, and the q-component is used for reactive power control. The main

Table 10.1. Similarities of vector control of grid side and rotor side converter control

Control loop	Rotor side	Grid side
Inner loop	Current control	Current control
Active loop	Speed Control	Direct voltage control
Reactive loop	Flux control	Reactive power control

purpose of the grid side inverter is to maintain a constant DC value, either by feeding the active power into the grid or by consuming active

power from the grid, depending on the speed of the DFIG, according to Fig. 5.1. Secondly, the inverter can be used to produce reactive power. A complex strategy can be implemented for the control of the reactive power for the complete system. The generator can be neutral with respect to reactive power, depending on the level of magnetizing. If the generator is not fully magnetized from the rotor, the stator will consume some reactive power. The grid inverter must then produce reactive power to keep the desired $\cos\varphi$ equal to one. Both inverters can help produce reactive power, depending on their active current load.

When considering the whole DFIG system with generator and back to back inverter, the system actually forms an Unified Power Flow Control (UPFC), where the generator is a rotating transformer. The UPFC is made of two back to back inverters, one connected in series with the grid and the other in parallel with the grid [54]. Considering the system as an UPFC gives many possibilities for control. The use of the grid side inverter for reactive compensation is less attractive, because the generator amplifies the current with the turn ratio, and the limiting factor for the inverters are mainly the current.

The voltage equation of the inverter reactors is

$$\begin{bmatrix} u_a \\ u_b \\ u_c \end{bmatrix} = R \begin{bmatrix} i_a \\ i_b \\ i_c \end{bmatrix} + L\frac{d}{dt}\begin{bmatrix} i_a \\ i_b \\ i_c \end{bmatrix} + \begin{bmatrix} u_a^{inv} \\ u_b^{inv} \\ u_c^{inv} \end{bmatrix} \tag{10.1}$$

The DC side of the system is modeled as

$$C_{DC}\frac{dU_{DC}}{dt} = i_{dc} - i_{rotor} \tag{10.2}$$

When transforming (10.1) into dq-reference frame we get:

$$\begin{bmatrix} u_d \\ u_q \end{bmatrix} = \begin{bmatrix} R & 0 \\ 0 & R \end{bmatrix}\begin{bmatrix} i_d \\ i_q \end{bmatrix} + \begin{bmatrix} L & 0 \\ 0 & L \end{bmatrix}\frac{d}{dt}\begin{bmatrix} i_d \\ i_q \end{bmatrix} + \begin{bmatrix} 0 & -\omega_e L \\ \omega_e L & 0 \end{bmatrix}\begin{bmatrix} i_d \\ i_q \end{bmatrix} + \begin{bmatrix} u_d^{inv} \\ u_q^{inv} \end{bmatrix} \tag{10.3}$$

or

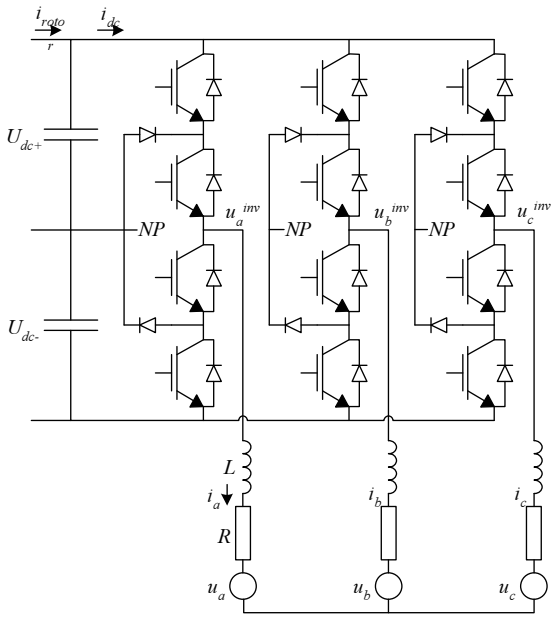

Fig. 10.1. Grid inverter control

$$\vec{u}_{dq}^{inv}(t) - R\vec{i}_{dq}(t) - L\frac{d}{dt}\vec{i}_{dq}(t) - j\omega_1 L\vec{i}_{dq}(t) - \vec{u}_{dq}(t) = 0 \tag{10.4}$$

From (10.3) it can be seen that there is a cross coupling between the d- and q-axis, with the terms $-\omega_e L i_q$ and $\omega_e L i_d$. This cross coupling is not present in the stationary system or in the $\alpha\beta$-frame.

In steady-state, (10.4) can be reduced by setting the derivative terms to zero. The steady-state expression becomes,

$$\vec{u}_{dq}^{inv}(t) - \vec{u}_{dq}(t) = R\vec{i}_{dq}(t) + j\omega_1 L\vec{i}_{dq}(t) \tag{10.5}$$

The state space description of the inverter is given by

$$\frac{d\vec{x}_L}{dt} = \mathbf{A}_L\vec{x}_L + \mathbf{B}_L\vec{u}_L \tag{10.6}$$

where the state vector and the input vector are

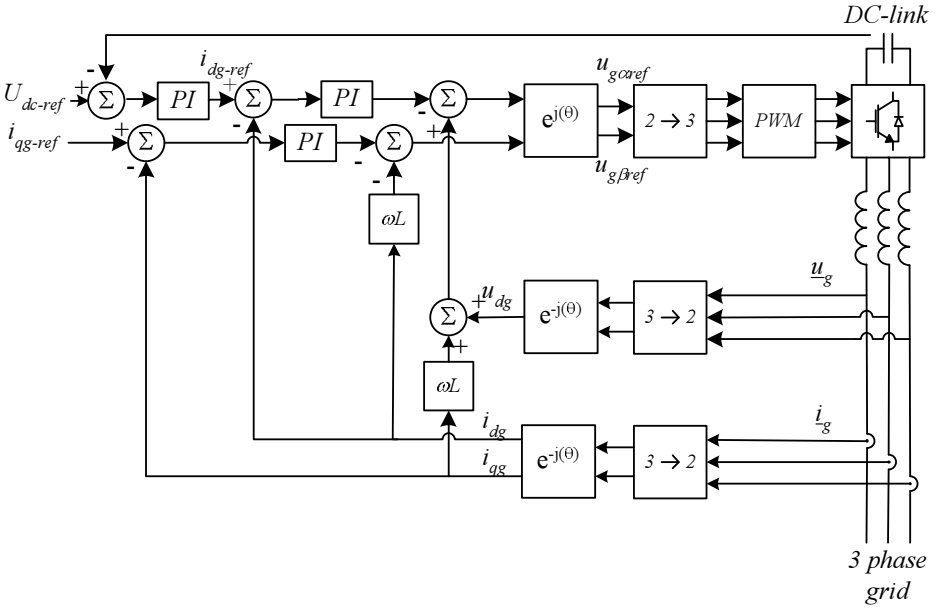

Fig. 10.2. Vector control of grid inverter.

$$\vec{x}_L = \begin{bmatrix} i_d \\ i_q \end{bmatrix} \tag{10.7}$$

and

$$\vec{u}_L = \begin{bmatrix} u_d^{inv} \\ u_q^{inv} \\ u_d \\ u_q \end{bmatrix} \tag{10.8}$$

the system matrix and input matrix are given by

$$\mathbf{A}_L = \begin{bmatrix} -\frac{R}{L} & \omega_1 \\ -\omega_1 & -\frac{R}{L} \end{bmatrix} \tag{10.9}$$

and

$$\mathbf{B}_L = \begin{bmatrix} \frac{1}{L} & 0 & -\frac{1}{L} & 0 \\ 0 & \frac{1}{L} & 0 & -\frac{1}{L} \end{bmatrix} \tag{10.10}$$

The state equation for the AC side of the system is linear as opposed to the DC side (10.2) which is non-linear, as well as time variant due to the switching function. If the DC-link is maintained at a constant value, a linearized small-signal model can be used to obtain the transfer function matrix [55]. When keeping the DC-link at a nearly constant value, the effect of the non-linearities is minor.

The power equations of the system given by (4.17) are repeated here

$$P = \frac{3}{2}(u_d i_d + u_q i_q) = \frac{3}{2}(u_\alpha i_\alpha + u_\beta i_\beta) \tag{10.11}$$

$$Q = \frac{3}{2}(u_d i_q - u_q i_d) = \frac{3}{2}(u_\alpha i_\beta - u_\beta i_\alpha) \tag{10.12}$$

If neglecting harmonics due to switching and due to harmonics in the grid voltage and the losses in the inverter and inductor resistance, we have the AC power and the DC power as

$$P_{AC} = \frac{2}{3}\,\mathrm{Re}\{\vec{u}_{\alpha\beta}\vec{i}^{*}_{\alpha\beta}\} \tag{10.13}$$

$$P_{DC} = u_{DC} i_{DC} \tag{10.14}$$

where the asterisk denotes the complex conjugate. The AC power in synchronously rotating reference frame

$$P_{AC} = \frac{2}{3}(u_d i_d + u_q i_q) \tag{10.15}$$

since $u_q = 0$ we have,

$$P_{AC} = \frac{2}{3} u_d i_d \tag{10.16}$$

Substituting (10.14) into (10.16), this gives an expression for the average DC link capacitor current $i_{C_{DC}}$

$$i_{C_{DC}} = \frac{2}{3}\frac{u_d}{U_{DC}} i_d \tag{10.17}$$

The differential equation of the DC link voltage gives [56]

$$\frac{dU_{DC}}{dt} = \frac{2}{3}\frac{1}{C_{DC}}\frac{u_d}{U_{DC}} i_d \tag{10.18}$$

a linearization of (10.18) around the average DC link voltage $\bar{U}_{DC}$ gives

$$\frac{d}{dt}\Delta U_{DC} = \frac{2}{3}\frac{1}{C_{DC}}\frac{u_d}{\bar{U}_{DC}}i_d \tag{10.19}$$

where ΔU_{DC} corresponds to the DC link voltage ripple and $\bar{U}_{DC}$ is the average DC-link voltage.

$$C_{DC} = \frac{S}{\bar{U}_{DC}\Delta U_{DC}}\frac{1}{2\omega} \tag{10.20}$$

10.2 Amplitude-Phase Control

Amplitude-phase control or voltage angle control is based on the steady state model of the inverter stated in (10.5). The effect of resistance in the filter coils is negligiable for this study, and is set to zero. This reduces (10.5) to

$$\vec{u}^{inv}(t) - \vec{u}(t) = j\omega_1 L\vec{i}^{inv}(t) \tag{10.21}$$

Equation (10.21) shows that the difference between the two voltage sources determines the current flow, so the power can be controlled by the magnitude and phase of the voltage vector of VSI, $\vec{u}^{inv}(t)$. The displacement angle between grid voltage and VSI voltage $\theta(t)$ is proportional to the active power, and the voltage drop over the inductance L is proportional to reactive power. The apparent power from the inverter to the grid

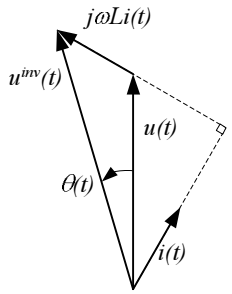

Fig. 10.3. Principle of voltage angle control.

is

$$S = U \cdot I^* = \vec{u}(t) \cdot \vec{i}^{inv}(t)^* = (u_d(t) + ju_q(t))(i_d(t) - ji_q(t)) \quad (10.22)$$

Active power and reactive power can be derived from (10.21) and (10.22),

$$\begin{aligned} P &= \mathrm{Re}(S) && (10.23)\\ &= \frac{U \cdot U^{inv}}{\omega_e L} \sin\theta \\ Q &= \mathrm{Im}(S) && (10.24)\\ &= \frac{U}{\omega_e L}(U - U^{inv}\cos\theta) \end{aligned}$$

Amplitude-phase control is simple to implement in a controller, but the bandwidth of the system is limited, since it is based on a steady state model

10.3 Phase Lock Loop

When connecting a power converter to the electrical grid, it is important to have a fast and accurate measure of the grid phase angle in order to be able control the power flow in or out of the power converter. Therefore, a phase lock loop (PLL) is implemented in the software. The function of the PLL is to keep track of the phase angle under any condition. The difficulty of this task is of course when the grid is distorted. In well balanced grid systems, a zero crossing detection works sufficiently as a PLL. The zero crossing point is sensitive to distortion of the waveform, and the variation of each phase is not considered in this form of angle detection [57]. Using a zero crossing detection in a system with power electronics will cause problems due to noise from the switching.

A simple way to get information about the phase angle is to use the angle of the voltage vector in the $\alpha\beta$-frame

$$\theta = \arctan\frac{u_\beta}{u_\alpha} \quad (10.25)$$

Using arctan of the voltage ratio works well with an ideal grid without disturbances. If the signals are distorted, the output of this method will

also be distorted. Filtering of signals is possible, but reduces the bandwidth of the PLL.

Another approach uses a synchronous dq-reference frame PLL [58], which is synchronized to the input voltage frequency. This method will still produce an angle containing large harmonics when the grid is distorted. Higher order harmonics can be filtered in the PLL, but lower order harmonics, 3rd, 5th, 7th etc. can not be filtered, since the bandwidth of the PLL will then be too low. This is a trade off between fast response and low harmonics for this setup.

If the three phase system is split into positive, negative and zero sequence as described earlier, and the positive sequence part of the signal is used, unbalance in the system will be eliminated [57]. Equation 10.26 shows the voltage signal split into its positive and negative sequence

$$\begin{bmatrix} u_a \\ u_b \\ u_c \end{bmatrix} = u_p \begin{bmatrix} cos(\omega t + \theta_p) \\ cos(\omega t - \frac{2\pi}{3} + \theta_p) \\ cos(\omega t + \frac{2\pi}{3} + \theta_p) \end{bmatrix} + u_n \begin{bmatrix} cos(\omega t + \theta_n) \\ cos(\omega t + \frac{2\pi}{3} + \theta_n) \\ cos(\omega t - \frac{2\pi}{3} + \theta_n) \end{bmatrix} \tag{10.26}$$

where subscript p and n denote positive and negative sequence variables respectively. Zero sequence is not considered. Equation 10.26 can also be written in space vector notation as,

$$u_{abc} = u_p e^{j(\omega t + \theta_p)} + u_n e^{-j(\omega t + \theta_p)} \tag{10.27}$$

If this equation is transformed to synchronous dq-reference frame, the voltages u_d and u_q are obtained as

$$\begin{aligned} u_{dq} = u_d + j u_q &= u_p e^{j(\theta_p - \theta_r)} + u_n e^{-j(2\omega t + \theta_p + \theta_r)} \\ &= (u_p \cos(\theta_p - \theta_r) + u_n \sin(2\omega t + \theta_p + \theta_r)) \\ &\quad + j(u_p \sin(\theta_p - \theta_r) - u_n \cos(2\omega t + \theta_p + \theta_r)) \end{aligned} \tag{10.28}$$

From the last equation, it can be seen that the negative sequence will cause a 2ω ripple.

Figure 10.4 shows the principle of how the PLL works. The PI controller will try to minimize u_q to zero. With this setup, u_d contains a 2ω ripple.

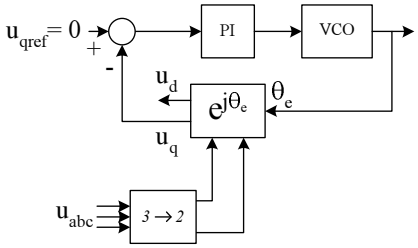

Fig. 10.4. Phase lock loop with full signal

To avoid the ripple, only the positive sequence should be used. Lee [57] has proposed a setup where only the positive sequence part of the voltage signal is used , similar is presented in [59]. Figure 10.5 shows how to use the positive sequence together with PLL.

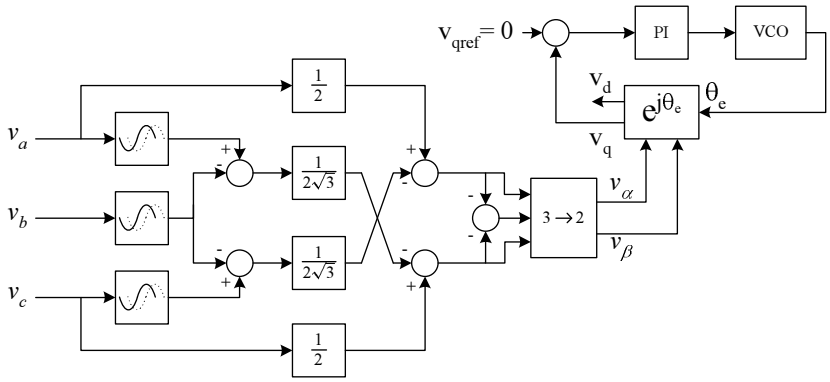

Fig. 10.5. Phase lock loop with positive sequence signal.

Figure 10.6 shows a spectrum of $\sin(\theta_e)$, where θ_e is the measured phase angle with a full PLL system, as in Fig. 10.5, compared with the lower graph which shows similar but with a simple PLL only using the u_β/u_α ratio, as in (10.25). In the lower graph, it is easy to see the grid harmonics, as well as the generator slot harmonics around 1000 Hz, with the generator running at 1300 RPM. The upper graph shows an almost perfect PLL signal, where the harmonics from the grid voltage are rejected, and therefore have no affect on the output of the PLL. The gain and

time constant of the PI control in the PLL system are critical for the performance.

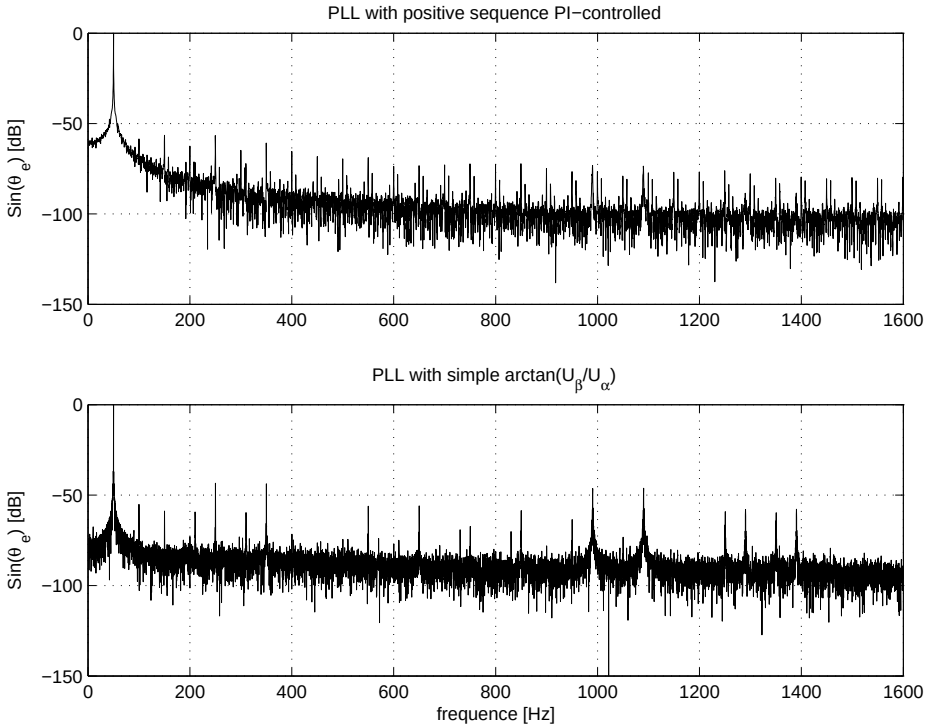

Fig. 10.6. Measured frequency spectrum of two different types of PLL.

Similar measurements where done on another location (see p127). At this location the voltage distortion was only 10% of what was seen at the university in Lyngby. Even with the lower distortion the spectrum looks almost the same, with the full PLL system, as it is shown in Fig E.1, Appendix E.

10.4 Bandwidth of the Inverters

According to Svensson [60], it is important that the control system can damp drive train resonances actively in the wind turbine. This requires a

bandwidth above 10 Hz, which is not the case for amplitude-phase control. Therefore, the control principle used is vector control.

Studies by Blasko et. al. [61] have shown that the bandwidth of a voltage source inverter is approximately 10-30 times smaller than the switching frequency. Sampling of the signal twice in every switch period increases the bandwidth to about 1/10 of the switching frequency. With synchronous sampling once in every cycle, the bandwidth is 1/20. The sampling used in the laboratory model is synchronous once in every sampling.

11

General Harmonic Analysis

Electrical equipment with power electronics connected to the grid cause nonsinusoidal grid currents, due to non-linear characteristics of the power electronics. Since the grid voltage is nearly sinusoidal and the voltage produced by the power electronics is often far from sinusoidal, the current from the power electronics will contain harmonics. According to Fourier analysis, any periodic waveform consists of a sum of sinusoidal waveforms with different frequency and phase, i.e. the fundamental frequency ω_1 and multiples of the fundamental frequency $h\omega_1$.

11.1 An Overview of Harmonics

Harmonics can be grouped into positive, negative and zero sequence:

Harmonics of the order $h = 6k + 1, \quad k = 1, 2, 3, \ldots$ are of a positive sequence. These harmonics will rotate in the direction of the fundamental. The lowest order positive sequence harmonics are 7th, 13th and 19th.

Harmonics of the order $h = 6k - 1, \quad k = 1, 2, 3, \ldots$ are of a negative sequence. These harmonics will rotate in the opposite direction of the fundamental. The lowest order negative sequence harmonics are 5th, 11th and 17th.

Harmonics of the order $h = 3k, \quad k = 1, 2, 3, \ldots$ are of zero sequence. The lowest order of zero sequence harmonics are 3rd, 9th and 15th.

It is practical to have a measure of the distortion of a distorted current waveform. This can be done by calculating the total harmonic distortion

(THD), defined as

$$THD = \sqrt{\sum_{h=2}^{h=h_{\max}} \left(\frac{I_h^2}{I_1^2}\right)} \tag{11.1}$$

where $h_{\max}$ is the maximum number of harmonics to be included, typically 40 or 50, depending on the standards the equipment has to comply with. In (11.1) the THD for the distorted current is found. Similar THD can be calculated for a distorted voltage.

11.1.1 Harmonics in the $\alpha\beta$-reference frame

Harmonics in the three phase system transformed to the $\alpha\beta$-reference frame will rotate in different directions depending on the order of the harmonic. The negative sequence will rotate in the opposite direction of the fundamental harmonic, and the positive sequence will rotate in the same direction as the fundamental harmonic, similar to what was described above.

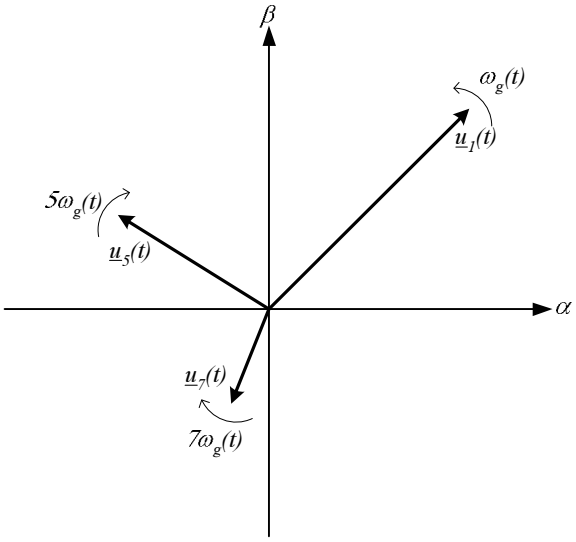

Fig. 11.1. Directions of different harmonics in the $\alpha\beta$-frame.

The load current of a line commutated rectifier can be represented in the stationary reference $\alpha\beta$-frame as [62]

Table 11.1. Harmonic transformation $\alpha\beta$-frame to dq-frame

Harmonic type	Harmonic n	$\alpha\beta$-frame	dq-frame
fundamental	$h = 1$	$\vec{i}_1^{\alpha\beta}(t) = \vec{i}_1 e^{j(\omega_1 t - \frac{\pi}{2})}$	$\vec{i}_{dq1}(t) = \vec{i}_1$
positive sequence	$h = 6k + 1$	$\vec{i}_{\alpha\beta h}(t) = \vec{i}_h e^{jh(\omega_1 t - \frac{\pi}{2})}$	$\vec{i}_{dqh}(t) = \vec{i}_h e^{j(h-1)(\omega_1 t - \frac{\pi}{2})}$
negative sequence	$h = 6k - 1$	$\vec{i}_{\alpha\beta h}(t) = \vec{i}_h e^{-jh(\omega_1 t - \frac{\pi}{2})}$	$\vec{i}_{dqh}(t) = \vec{i}_h e^{-j(h+1)(\omega_1 t - \frac{\pi}{2})}$

$$\vec{i}_{\alpha\beta}^{load} = \sqrt{3} I_1 e^{j(\omega_1 t + \phi_1)} + \sum_{6k-1} \sqrt{3} I_h e^{-j(h\omega_1 t + \phi_h)} + \sum_{6k-1} \sqrt{3} I_h e^{j(h\omega_1 t + \phi_h)} \tag{11.2}$$

11.1.2 Harmonics in the *dq*-reference frame

Transforming vectors from the stationary $\alpha\beta$-frame to a synchronously rotating dq-frame results in a counter-clockwise rotation of the $\alpha\beta$-frame with an angular frequency equal to the fundamental frequency, if the dq-system is synchronous with the rotation of the grid. Transforming the current vector $i_{\alpha\beta}$ gives

$$i_{dq} = i_{\alpha\beta} e^{-j(\omega_1 t - \frac{\pi}{2})}$$

The fundamental current vector in the $\alpha\beta$-frame will be transformed to a stationary vector in the dq-frame. Positive sequence harmonics will rotate with the speed $(h-1)\omega_1$, and negative sequence harmonics will rotate with the speed $(h+1)\omega_1$.

The harmonic transformation from $\alpha\beta$-frame to dq-frame are shown in Table 11.1.

11.2 Analysis of Harmonics and Interharmonics in a DFIG

When a symmetrical three phase induction machine is connected to a system of symmetrical three phase voltages, the air-gap flux will contain harmonics [22]. This is mainly due to none perfect distribution of the windings, both in the stator and rotor.

It has been shown in the literature that a doubly fed induction motor fed by a cycloconverter has a certain amount of harmonic content in

its current, if the stator is connected to a fundamental frequency voltage source [63]. By using modern self-commutated IGBT inverters with a relatively high switching frequency, the inverter will not cause any low harmonic content in the voltage. The lower part of Fig 11.2 shows the spectrum of the rotor current when the rotor is fed by an inverter. In [63] it was assumed that the voltage source was a pure sinus. This is not the case in most electrical grids, where a small content of 5th, 7th, 11th and 13th harmonics are always present.

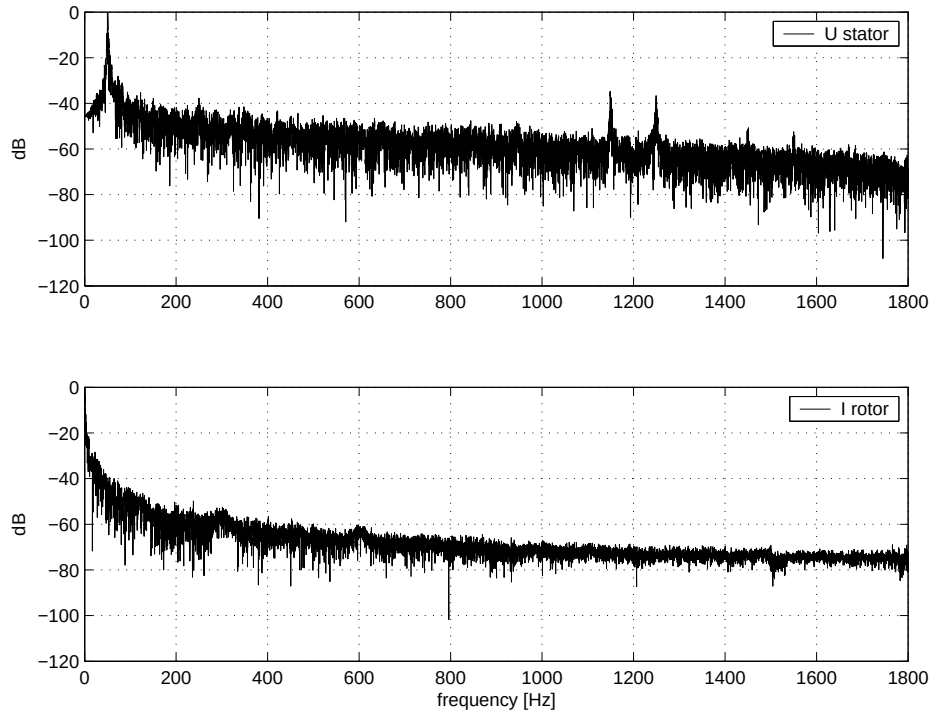

Fig. 11.2. Frequency spectrum of DFIG at synchronous speed without stator conn. to grid (1500 RPM)

Due to the non-sinusoidal distribution of the stator and rotor windings, the air-gap flux will contain higher harmonics, referred to as MMF space harmonics. A normal induction generator with a squirrel cage rotor will cause some 5th, 7th, 11th and 13th harmonics in the stator current, due to the induced voltage in the stator. With a short circuited rotor there

will be no induced voltage in the rotor, resulting in higher harmonics of the rotor frequency. With the DFIG, on the other hand, the rotor circuit is connected to a voltage source, causing a current from the rotor and its higher harmonics. The left side of Table 11.2 shows the harmonics in the stator, the right side shows the harmonics in the rotor. The first term comes from the higher harmonics due to the stator. The second term comes from the harmonics in the rotor. The first two lines are harmonics due to stator harmonics. The last two lines are the harmonics due to the slip, these are called slip harmonics. $n = 1, 2, 3, \ldots$ and $m = 1, 2, 3, \ldots$

Table 11.2. Stator and rotor current harmonics

Stator harmonics	Rotor harmonics
$(6m-1)f_{grid} - 6(n-1)f_{slip}$	$(6m)f_{grid} - (6n-5)f_{slip}$
$(6m+1)f_{grid} + 6(n-1)f_{slip}$	$(6m)f_{grid} + (6n-5)f_{slip}$
$(6m-1)f_{grid} - 6(n)f_{slip}$	$(6m)f_{grid} - (6n-1)f_{slip}$
$(6m+1)f_{grid} - 6(n)f_{slip}$	$(6m)f_{grid} - (6n+1)f_{slip}$

Figure 11.3 shows a frequency spectrum of both the stator and the rotor at 1350 RPM and 1650 RPM. Comparing the spectrums at the different frequencies shows that the slip harmonics change as a function of the slip.

11.2.1 Saturation

If the main flux paths get saturated, a third harmonic voltage is produced in each stator phase voltage [22]. Because these third harmonic voltages all are in phase, they do not cancel out. The third harmonics are present with an amplitude approximately one fifth of the slot harmonics [22].

11.2.2 Slot Harmonics

Slots in the rotor and stator are another source of harmonics in the machine. The slot harmonics are produced by variations in the reluctance due to the slots. The slot harmonics in the air-gap MMF induce slot harmonic

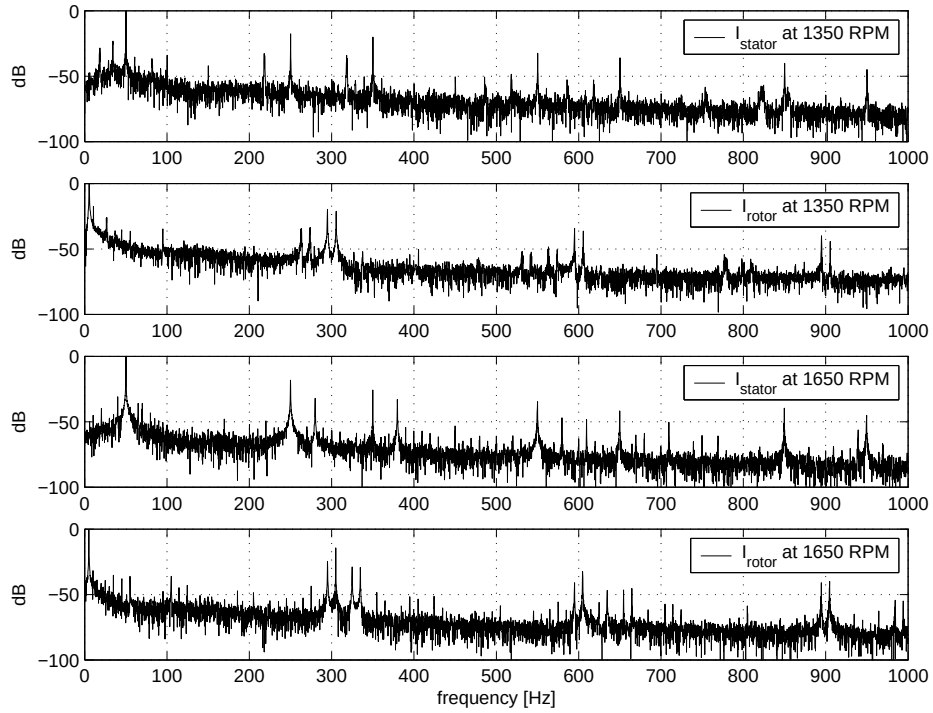

Fig. 11.3. Frequency spectrum of DFIG stator and rotor current measured at ±10% slip.

voltages in the rotor and stator voltages. Every time the magnetic field in the air-gap passes by a stator slot, it increases the rotor and stator voltage in steps, so even with a pure sinus voltage source, the current from the generator contains harmonics.

The slot harmonics in the stationary $\alpha\beta$-frame are given by

$$f_{sh} = f_1(\frac{2S}{P}(1-s) \pm 1) \tag{11.3}$$

S is the number of slots in the stator, P is the number of poles. Figure 11.2 upper graph shows the no load stator voltage when an almost pure sine current is fed into the rotor. The generator used has 4 poles and 48 stator slots. Using (11.3), the slot frequencies at synchronous speed should be at 1150 Hz and 1250 Hz, which is also the case in the Fig 11.2. The same is true when the machine runs at other speeds, see Fig 11.4 and 11.5

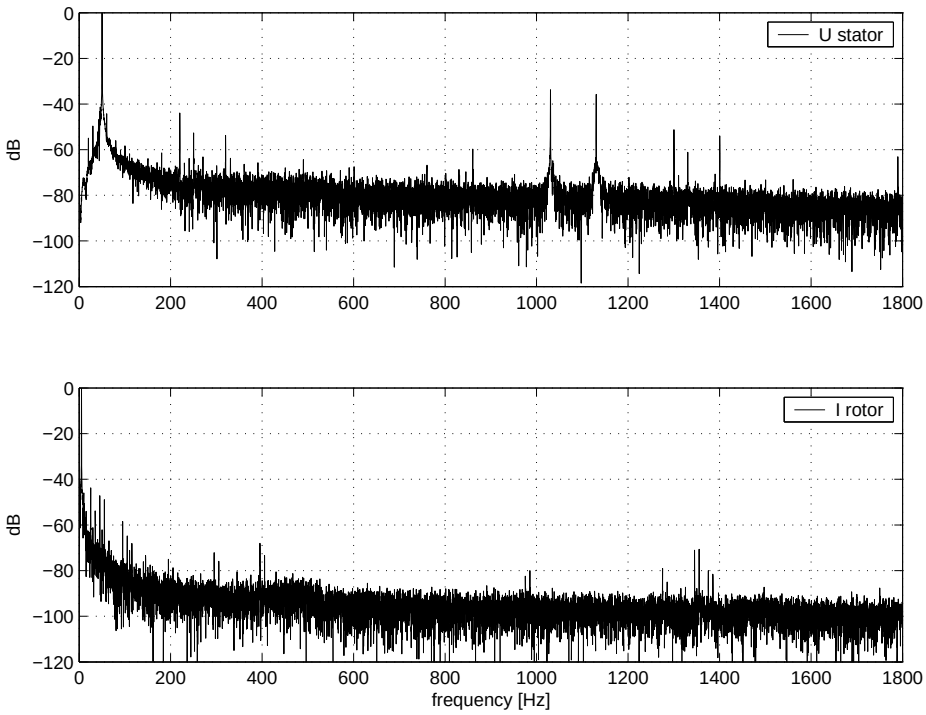

Fig. 11.4. Frequency spectrum of the DFIG at 1350 RPM without stator conn. to grid

Induction machines normally have skewed rotors, but this is not the case for DFIG machines. If the rotor is not skewed, it gives higher amplitude slot harmonics. The slot harmonics can be used in speed sensing [64]. Since the slot harmonics are very distinctive, it is fairly easy to extract them from the frequency spectrum and use the signal for speed prediction.

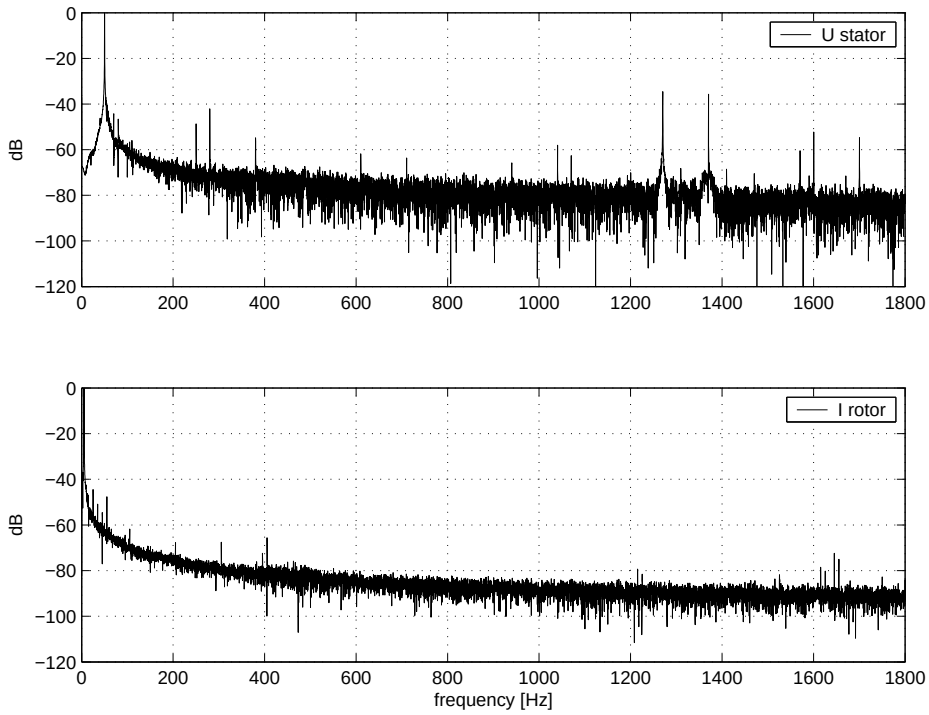

Fig. 11.5. Frequency spectrum of DFIG at 1650 RPM without stator conn. to grid

12

Adaptive Active Filtering

An active shunt filter consists of a controllable voltage source converter with a DC voltage link and a filter inductance, like the grid inverter described in chapter 10. The principle of an active shunt filter is to inject the undesired components of the load current into the load current, in order to eliminate their presence in the line current. In this chapter, an adaptive active filter is implemented.

12.1 The Least Mean Squares Algorithm

The harmonics described in the previous chapter often have to be reduced in some sort of a filter in order to comply with the international standards for wind turbines [9]. A normally tuned passive filter will filter the harmonics from the stator, but the slip harmonics from the rotor vary in frequency as a function of the slip, making a tuned filter useless. Instead an active filter implemented in the power converter will work. The filter will have to change its characteristics when the slip changes. Another approach to reduce the harmonics is to use an adaptive filter, where an adaptation algorithm sets the weights of the filter. A simple and often used adaptation algorithm is the Least Mean Squares (LMS). This algorithm, first presented by Widrow and Hoff [65], is given by the equations.

$$y_k = w_k^T x_k \tag{12.1}$$

$$\varepsilon_k = d_k - y_k \tag{12.2}$$

$$w_{k+1} = w_k + 2\mu\varepsilon_k x_k \tag{12.3}$$

where x_k and y_k are filter input and output, respectively, d_k is the signal with noise and μ the adaptation constant that determines the step size, taken at each iteration, along the estimated negative-gradient direction. The subscript k is the discrete time index.

By choosing a small enough μ, adaptation noise due to error in the gradient estimate is average out.

In other algorithms, one would have to estimate the gradient of $\xi = E[\varepsilon_k^2]$ by taking the difference between the short term averages of ε_k^2. The LMS algorithm needs only the square of the error ε_k^2, and that is the estimate of ξ_k.The gradient estimate can then simply be calculated at each iteration.

$$\tilde{\boldsymbol{\nabla}}_k = \begin{bmatrix} \frac{\partial \varepsilon_k^2}{\partial w_0} \\ \vdots \\ \frac{\partial \varepsilon_k^2}{\partial w_L} \end{bmatrix} = 2\varepsilon_k \begin{bmatrix} \frac{\partial \varepsilon_k}{\partial w_0} \\ \vdots \\ \frac{\partial \varepsilon_k}{\partial w_L} \end{bmatrix} = -2\varepsilon_k \mathbf{X}_k \tag{12.4}$$

This simple estimate of gradient can then be used in a steepest descent type of adaptive algorithm [66]

$$\begin{aligned} \mathbf{W}_{k+1} &= \mathbf{W}_k - \mu\tilde{\boldsymbol{\nabla}}_k \\ &= \mathbf{W}_k + 2\mu\varepsilon_k \mathbf{X}_k \end{aligned} \tag{12.5}$$

From (12.5) it can be seen that LMS is easy to implement, since it does not require any squaring averaging or differentiation. For a more in depth coverage of this topic, see [66].

12.2 Adaptive Filtering of Higher Harmonics

Glover has presented the single frequency adaptive notch filter [67]. This adaptive filtering algorithm consist of two processes:

- a filtering process
- an adaptive process

Use of the Least Mean Square (LMS) algorithm to eliminate higher harmonics in line connected converters has been presented by Blasko [68]. Figure 12.1 shows the method of the adaptive single frequency notch filter

$$x_k^s = \sin(n\omega_0 k T_s) \tag{12.6a}$$

$$x_k^c = \cos(n\omega_0 k T_s) \tag{12.6b}$$

where T_s is the sampling period, ω_0 is the notch circular frequency of the filter, k is the discrete time index, and superscripts c and s relate to sine and cosine, respectively. The LMS algorithm cross correlates the reference inputs x_k^s and x_k^c with the error input ε_k and adjusts w_k according to

$$w_{k+1}^s = w_k^s + 2\mu\varepsilon_k x_k^s \tag{12.7a}$$

$$w_{k+1}^c = w_k^c + 2\mu\varepsilon_k x_k^c \tag{12.7b}$$

where μ is the adaptation gain which regulates how fast the system adapts and the stability of adaptation. Weights are adjusted until the component of noise with frequency ω_0 is eliminated from the error ε_k.

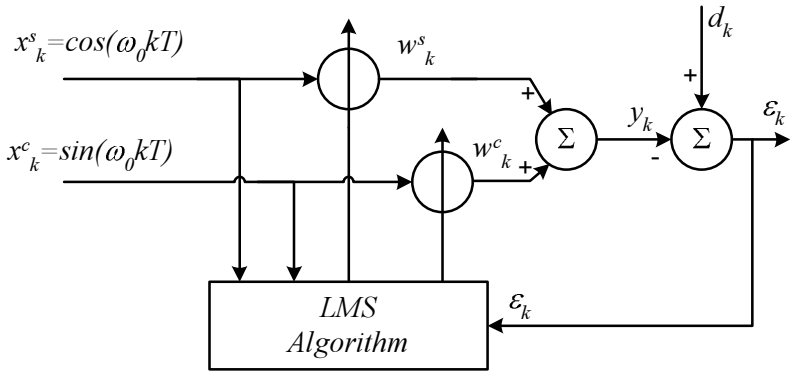

Fig. 12.1. Single frequency adaptive LMS filter

This can be extended to a multi-frequency filter, where the notch filter x_k expands to

$$\vec{X}_k^s = [..x_k^s..]^{\mathrm{T}} = \sin(n\omega_1 kT_s) \tag{12.8a}$$

$$\vec{X}_k^c = [..x_k^c..]^{\mathrm{T}} = \cos(n\omega_1 kT_s) \tag{12.8b}$$

where n is the nth harmonic component to be eliminated from the current (n = 5,7,11,13,17,19...)

For the multi-frequency case, the weight function becomes a weight vector, $\vec{W}_k^s = [..w_{nk}^s..]^{\mathrm{T}}$ and similar for the cosine part $\vec{W}_k^c = [..w_{nk}^c..]^{\mathrm{T}}$, these vector are updated by the LMS algorithm

$$\vec{W}_{k+1} = \vec{W}_k + 2\mu\varepsilon_k\vec{X}_k \tag{12.9}$$

The filter output is

$$y_k = \vec{W}_k^{s\mathrm{T}}\vec{X}_k^s + \vec{W}_k^{c\mathrm{T}}\vec{X}_k^c \tag{12.10}$$

12.3 Implementation

When using the adaptive filtering method together with a DFIG system, it is obvious that the adaptive filter can be applied in both inverters. The grid side converter can be used as a normal active shunt filter [68]. The rotor side converter can be used as an active filter by injecting current into the rotor which is transformed through the air-gap to the stator. This filter is a series filter.

In the laboratory setup, the LMS algorithm was implemented as described in [68] for the grid side inverter. The algorithm in the rotor-stator circuit is implemented, so that the notch filter currents are injected into the rotor current in order to eliminate harmonics in the stator current.

When using the adaptive filter together with the inverters, the error filter input ε_k is instead the inverter current.

12.3.1 Grid Side Filter

The implementation of single frequency notch filters on the grid side converter has to be made in the stationary $\alpha\beta$-frame to avoid cross coupling between the q and d axes [68]. Therefore, the notch filters were implemented in the stationary $\alpha\beta$-frame for the grid side filter. There are mostly some 5th and 7th harmonics in the grid side converter current, as well as some 11th and 13th harmonics. Due to the asymmetrical 3rd harmonic content in the 3 phases, the 3rd harmonic was able to flow without a neutral conductor. Three notch filters were implemented, one for each frequency: 150 Hz, 250 Hz and 350 Hz. Though the effect of the 150 Hz filter properly will be limited since there is no symmetry.

The measured grid side current, transformed to the stationary $\alpha\beta$-frame, is the error input ε_k to the filter.

The filter output y has to be multiplied by the line inductor impedance

$$\begin{aligned} u_n &= y_n \omega_{grid} L \\ &= \left\{ w_n^s \sin(n\omega_{grid}) + w_n^c \cos(n\omega_{grid}) \right\} n\omega_{grid} L \end{aligned} \tag{12.11}$$

where L is the grid side inductor. This gives the signals that are added to the grid side inverter voltage reference in the $\alpha\beta$-frame

$$u_{\alpha ref2} = u_{\alpha ref} + u_{\alpha 3} + u_{\alpha 5} + u_{\alpha 7} \tag{12.12a}$$

$$u_{\beta ref2} = u_{\beta ref} + u_{\beta 3} + u_{\beta 5} + u_{\beta 7} \tag{12.12b}$$

12.3.2 Rotor Side Filter

The notch filters are implemented in the synchronous rotating dq-frame. Although cross coupling between the q and d axes is also present here, it does not affect the filter. In steady state (9.19) is reduced and when neglecting the resistive part, while $R_r \ll n\omega\sigma L_r$, it gives,

$$u_{dr} = -\omega_{slip} \sigma L_r i_{qr} \tag{12.13a}$$

$$u_{qr} = \omega_{slip} (L_m i_{ms} + \sigma L_r i_{dr}) \tag{12.13b}$$

Equations (12.13a) and (12.13b) are used for decoupling between u_{dr} and i_{dr}, likewise for u_{qr} and i_{qr}. There is only the cross coupling between d and q.

The fact that the $(6n \pm 1)$th harmonics in the stationary $\alpha\beta$-frame transform to the $(6n)$th harmonics in the synchronous rotating dq-frame means that one filter is enough to eliminate two harmonics. In the setup, I have tried to eliminate 5th and 7th harmonics at 250Hz and 350Hz, and 5th and 7th slip harmonics at 220Hz and 320Hz with 10% slip.

The measured stator current, transformed to the synchronous rotating dq-frame, is the error input ε_k to the filter.

The filter output y has to be multiplied by the impedance from (12.13a)

$$\begin{aligned} u_6 &= y_6 \omega_{slip} \sigma L_r \\ &= \left\{ w_6^s \sin(6\omega_{grid}) + w_6^c \cos(6\omega_{grid}) \right\} 6\omega_{slip} \sigma L_r \end{aligned} \tag{12.14}$$

$$\begin{aligned} u_{slip} = &\left\{ \begin{array}{c} w_{slip}^s \sin(6(\omega_{grid} - \omega_{slip})) \\ +w_{slip}^c \cos(6(\omega_{grid} - \omega_{slip})) \end{array} \right\} \\ &\cdot \frac{\omega_{grid} - \omega_{slip}}{\omega_{grid}} 6\omega_{slip} \sigma L_r \end{aligned} \tag{12.15}$$

This gives the signals that are added to the rotor converter voltage reference in the dq-frame

$$u_{dref2} = u_{dref} + u_{d6} + u_{dslip} \tag{12.16a}$$

$$u_{qref2} = u_{qref} + u_{q6} + u_{qslip} \tag{12.16b}$$

The results of the filtering are shown in Chapter 15, Measurements.

Part II

Laboratory Setup

One of the main objects of this Ph.D. project was to construct a laboratory model with a doubly fed induction generator. The model was intended to gain information about control of DFIG machines. In order to have a model with dynamics comparable to a full scale system, the generator had to be greater than 25kW, so the machine parameters would be similar. The size of power converters also had to be considered when designing the setup. Again here the parameters have to be similar to a full scale setup.

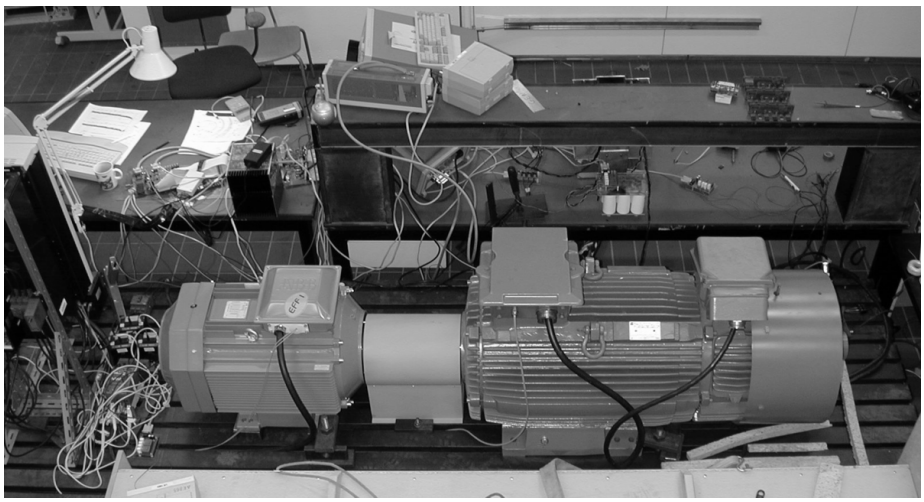

Fig. 12.2. Laboratory setup with torque producing motor to the left and the DFIG machine to the right.

13

Hardware Specifications

The laboratory setup consist of a 40 kW DFIG generator mechanically connected to a torque producing motor. The DFIG is electrically connected to the grid and to a power converter, via the stator and the rotor, respectively. Besides the rotating machinery there are measuring circuits, a frequency converter for the motor, etc. Fig. 13.1 shows the principle schematics of the setup. This chapter will give details about the hardware in the setup.

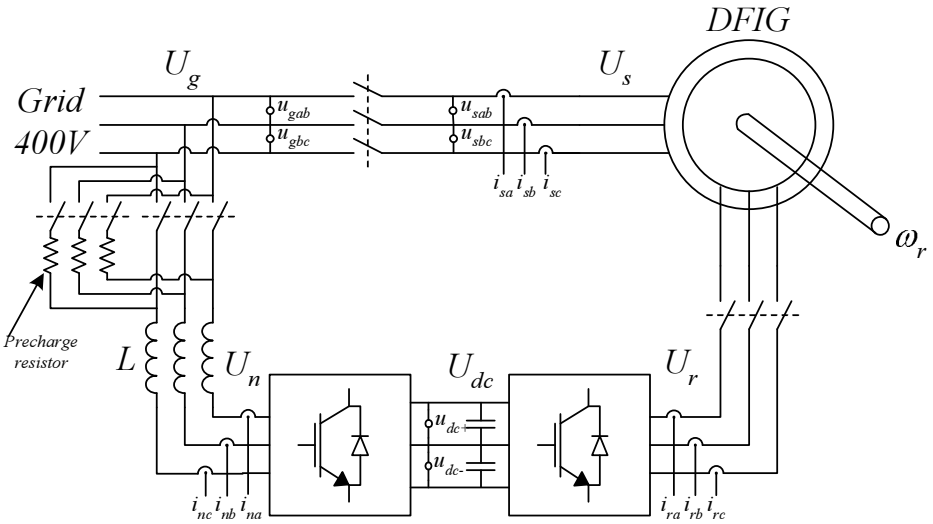

Fig. 13.1. Schematics of the DFIG laboratorie setup.

13.1 The Rotating Machinery

The main component in the setup is a 40kW DFIG produced by Leroy-Somer. It is a 4 pole generator. The generator is connected with a Y-connected stator and rotor.

The torque-producing-motor or load-motor is a 37 kW induction motor made by ABB. The motor is stator fed by a torque controlled frequency converter, ABB ACS601-0037-4.

Data for both machines can be found in the appendix C.

Temperature sensors

Three PT-100 sensors have been placed in the stator windings of the DFIG. The sensors are monitored by a PT-100 transducer (PR-Electronics 2271). Only one single transducer is used for all three sensor. They are connected in series forming a PT-300 sensor. This requires a uniform heating of the stator or reduced maximum allowed temperature. The transducer supply a 4-20 mA output signal. This signal is used to display the actual stator temperature in the control panel, for the load motor's frequency converter (ACS601). The transducer also has a relay, that when activated trip the ACS601 and the control system for the DFIG.

Speed sensor

The DFIG is equipped with an encoder at the non-drive end. The encoder has two channels, each with 1024 pulses. If detecting the edges, it gives a total resolution of 4096 increments per round. The encoder signals are transmitted to a digital interface board. The speed of the DFIG and the load motor is also monitored by the ACS601. If the speed is below 1100 RPM, a relay in the ACS601 will open and the stator contactor will disconnect the DFIG from the grid for safety reasons.

13.2 Power Inverters

The two back to back inverters are designed on the specification in table 13.1 and 13.2.

Table 13.1. Design specifications for grid side inverter

rated power	S_g	14kVA
grid voltage	U_g	400V
grid current	I_g	20A
grid frequency	f_1	50Hz
switching freq.	f_{sw}	4kHz
DC-link volt.	$U_{DC,max}$	720V

Table 13.2. Design specifications for rotor side inverter

rated power	S_r	14kVA
rotor voltage	$U_{r,max}$	400V
rotor current	I_r	20A
rotor frequency	f_r	0-12.5Hz
switching freq.	f_{sw}	4kHz
DC-link volt.	$U_{DC,max}$	720V

As discussed in chapter 7, the power converters used in the laboratory setup are IGBT based 3-level neutral point clamped converters (see p43). The IGBTs are Intersil's HGTG20N120CND. It is a 1200V IGBT with an integrated anti-parallel hyperfast diode [69]. The clamp diodes are Intersil's RHRP15100, a 1000V hyperfast diode [70]. Each single phase NPC inverter is mounted on a PCB, equipped with the four switches, the two clamp diodes and the gate resistors.

Each three phase converter has twelve IGBTs, therefore a normal three phase gate-driver module for a 2-level inverter is not sufficient. Each inverter is equipped with two six-pack driver circuits from Semikron SKHI 61. This driver takes care of interlocking and dead time. Both SKHI 61 modules are mounted on a gate-driver PCB, see Fig. 13.2. Under normal operation, the SKHI 61 has an interlocking function, that sets the dead time to prevent both the top and the bottom IGBT from being switched on simultaneously. This function can be disabled, but then the dead time is set to 0 μs. Otherwise the dead time is between 1-4 μs. Having the two SKHI 61 modules connected to the three phases so that IGBT switch S1 and S2 are driven by one gate-driver module, and similar for S3 and S4,

causes problems because of the interlocking. Therefore, IGBT S1 and S3 are driven by driver module 1 and IGBT S2 and S4 are driven by module 2 for phase A. The same applies for phases B and C. The drivers also provide short circuit protection. This is done by sensing U_{CE} on each IGBT. In addition, the gate driver PCB provides an error input pin and two error output pins. These are used in the safety system together with the DSP.

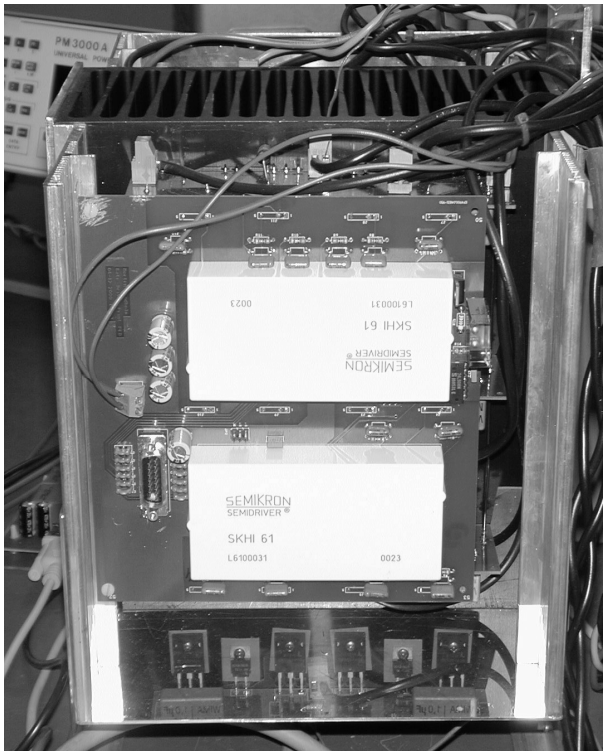

Fig. 13.2. Photograph of the gate driver connected on three single phase inverter PCBs.

The inverters are constructed so they both share the air duct formed by the heatsinks, see Fig. 13.3. The air duct is forced ventilated with two 100 mm fans.

13.3 DC-link

The DC-link capacitor C_{DC} serves as an energy storage

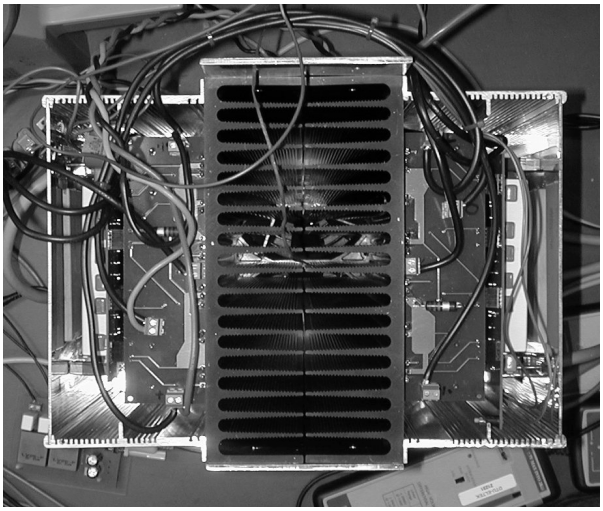

Fig. 13.3. Top view of the power converters.

$$C_{DC}\frac{du_{DC}}{dt} = i_{grid} - i_{rotor} \tag{13.1}$$

The current in the DC-link can be derived from the AC power at either side, since the DC power must equal the power on the AC side when neglecting the losses. The instantaneous power on the AC side and the DC side was already found in (10.13) and (10.14) respectively,

Selecting the size of the DC-link is a trade off. A small capacitance makes fast changes in the DC voltage possible. Fast changes of the DC link voltage may be necessary in case of an erupt voltage drop on the grid. Then the rotor side converter will need as much voltage as possible in order to control the flux in the machine. On the other hand, a small capacitance results in higher ripple and the current flowing in each capacitor module would be high, resulting in a reduced expected lifetime. A large capacitance does the opposite, it has a slow response to voltage changes, but the current in each capacitor can is smaller, thereby increasing lifetime. The relation between ripple voltage and actual size of the capacitance was given in (10.20). One of the design criterias was a ripple voltage below 50 V, which result in a 1300 μF capacitor.

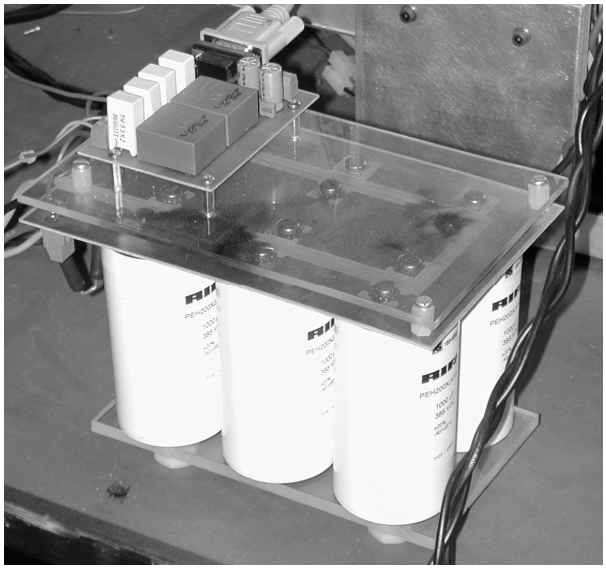

Fig. 13.4. The DC-link capacitor with dual voltage measurement.

The DC link consists of six 1000 μF, 385 V electrolytic capacitors from EVOX-RIFA. To get the DC voltage level high enough, the DC link is made with a series connection of two capacitors, and then three sets of capacitors in parallel. This gives a 1500 μF, 770 V capacitor. When capacitors are series connected it is normal to derate the voltage level due to asymmetry in the capacitors. Derating is not necessary with this DC-link since the neutral point is measured, and kept balanced.

13.4 Line filter

The output line filter between the grid and the converter is a simple inductance L-filter. The line filter reduces the higher harmonic content in the line current, produced by the switching of the inverter.

This type of filter was chosen due to its simplicity. Another option would have been a LC-filter or a LCL-filter, but the frequency response of LCL-filter has a resonance peak. This peak can, however, be damped by a series resistor or the filter can be designed so the peak does not interfere with the frequency response for the inverter output voltage. A

comparison of the LCL-filter with the L-filter. Shows that the LCL has a 60 dB/decade attenuation above and 20 dB/decade below the resonance frequency, whereas the L-filter has a 20 dB/decade attenuation in the full frequency range. The sum of the two inductances in the LCL-filter is smaller than the single inductance used in the L-filter [56]. As a consequence of this, the voltage drop across the LCL-filter is lower. This requires a lower DC-link voltage.

The following equation is a design expression for harmonics in the filter

$$L = \max_{h}\left(\frac{U_{phase,h}}{h\omega_1 I_{h,\max}}\right) \tag{13.2}$$

where $U_{phase,h}$ is the RMS value of the output phase voltage harmonics, and h is the index of the harmonic order. The filter inductors used are ordered with extra terminals, so it is possible to reduce the inductance of the filter. The sizes of the filters are

$$\begin{aligned} L_{\min} &= 3.2mH \\ L_{\mathrm{mid}} &= 4.8mH \\ L_{\max} &= 6.4mH \end{aligned} \tag{13.3}$$

equal to $1\Omega, 1.5\Omega$ and 2Ω.

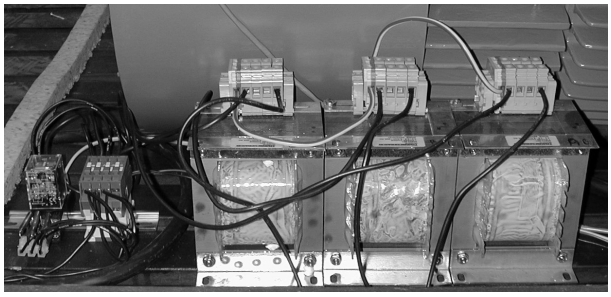

Fig. 13.5. Line filter with contactor and pre-charge contactor.

13.5 Voltage and Current Sensors

The actual signals are measured using hall-effect current transformers made by LEM. In Table 13.3 the measuring signals are listed. All signals are measured with a sampling frequency of 4 kHz. The location of the different sensors are shown in Fig. 13.1.

Table 13.3. Measuring signals.

Signal	Range	Peak range	Transducer
I_{rA}, I_{rB}, I_{rC}	25A_{rms}	±80A	LTS 25-NP
I_{nA}, I_{nB}, I_{nC}	25A_{rms}	±80A	LTS 25-NP
I_{sA}, I_{sB}, I_{sC}	100A_{rms}	±150A	LA 100-P
U_{abn}, U_{bcn}	480V_{rms}	±670V	LV25-P
U_{abs}, U_{bcs}	480V_{rms}	±670V	LV25-P
U_{dc+}, U_{dc-}	480V_{rms}	±670V	LV25-P

For the current sensors, all three phases are measured eventhough two phase would have been sufficient. The additional sensors were made in order to detect whether one of the signals was wrong. It was also intended to be used in an earth leakage protection system, but this was never implemented.

There are three sets of voltage sensors. The first set is for the two DC-link voltages, where the DC neutral point is very important. The second set is used to measure the grid voltage. It measures two phase to phase voltages. By doing so, the information about zero sequence is lost, but it is still possible to split into positive and negative sequence systems. Information about the zero sequence could have been captured by using the ground plane where the machines are standing as a zero point. The last set of voltage sensors are two phase to phase voltages at stator terminals on the generator. These sensors are needed in order to connect the generator in phase with the grid.

The voltage sensors are also based on a current transformer. These sensors use a shunt resistor that is dimensioned so a current of 10 mA

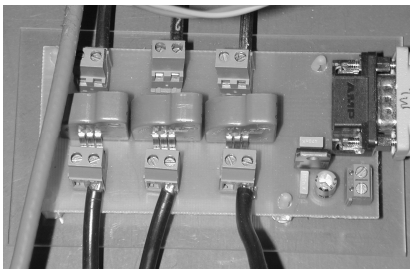

(a) Current measurements.

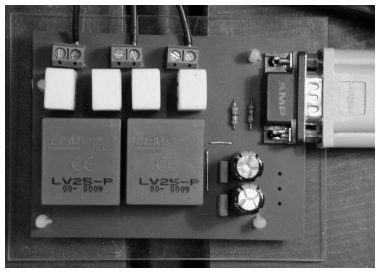

(b) Voltage measurements.

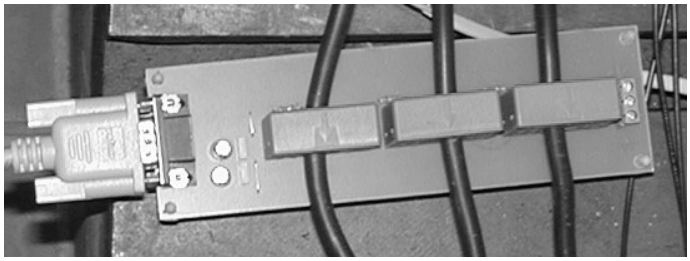

(c) "High" current measurements.

Fig. 13.6. Measurements with Hall elements.

flows through the resistor and the measurement coil of the Hall sensor. For the schematics see appendix D.

13.6 Control hardware

The control system for both inverters is implemented with a single Digital Signal Processor. All communication in/out the DSP goes through an interface board. The interface board is split into two, an analogue board, with the Analog to Digital Converters (A/D converter), which communicates with the other board, the digital board, through a Serial port interface (SPORT), see figure 13.7.

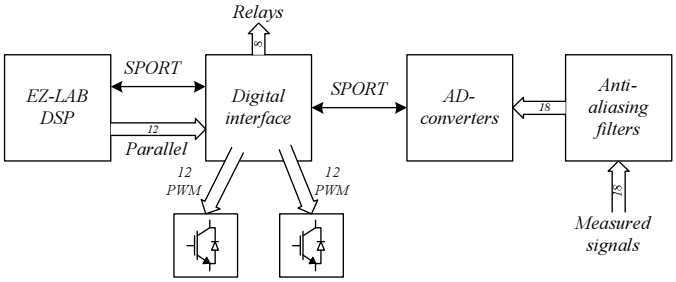

Fig. 13.7. Functional diagram of the control hardware.

The schematics of all the circuits are in the appendix D, except for the DSP EZ-LAB schematics.

13.6.1 Digital Signal Processor board

The Digital Signal Processor (DSP) processor used is the ADSP-21065L from Analog Device©. The DSP is mounted on an evaluation kit (EZ-LAB) from Analog Device©.

The EZ-LAB contains 1M x 32bit of external SDRAM and the DSP itself has 544 Kbit of internal SRAM. There are 12 flags that can be programmed as inputs or outputs. In this setup, flag_0-flag_3 are programmed as inputs, the rest are outputs. Flag_0-flag_3 are controlled by push buttons on the DSP board. Flag_4-flag_9 are wired to LEDs.

There are three external interrupts (IRQ_{0-2}) available plus a large list of internal interrupts. IRQ_0 is connected to a push button. It is used as a main interrupt that controls the flow of the program. The interrupt is edge-triggered so each time the button is activated, the program moves to another state, see figure 14.1. The other two hardware interrupts are used to trip the program in case of inverter failure. The inverter failure signal comes from the gate-driver board.

There are two timers, both used for PWM generation, one for each inverter. They have the same priority in the interrupt vector table, so in order to detect which timer has expired, a status bit is set for the expired timer.

The DSP features two synchronous serial ports (SPORT) with a maximum data rate of 30 Mbit/s. Each SPORT has a primary and a secondary set of transmit and receive channels. Together with the SPORTs, it is possible to initialize a set of cyclic buffers. For this application, a cyclic buffer with 18 entries is used for data transmission from the AD-converters. A SPORT interrupt is raised, whenever all 18 signals from the AD-converter are recieved and the buffer is full. All though it may cause problems with jitter. The execution of the main software starts whenever the SPORT interrupt is raised, this minimize the delay between sampling and execution.

13.6.2 Digital board

The digital board has several functions. These are listed in Table 13.4. There are a few comments to the list in Table 13.4. The aux. optical I/O was never used, but added to better suit unexpected needs for additional I/O's. The PWM signals are generated in the DSP. The parallel bus is used to transfer the PWM signals to a simple latch. The latch maintains the setting until a new switch combination is calculated. This is a simple, but very demanding use off the timers. Both timers in the DSP are used to implement the two PWM generators.

The SPORT interrupt is used as the main interrupt of the program. The interrupt is raised whenever all sampled measurements, have been clocked into the DSP's SPORT buffer.

Table 13.4. Functions of the digital board.

buffering of all I/O's
SPORT from ADC's
PWM latch for net inverter
PWM latch for rotor inverter
encoder interface
4 Relay output for $12V_{DC}$
4 Relay output for $230V_{AC}$
4 Aux optical inputs
4 Aux optical outputs

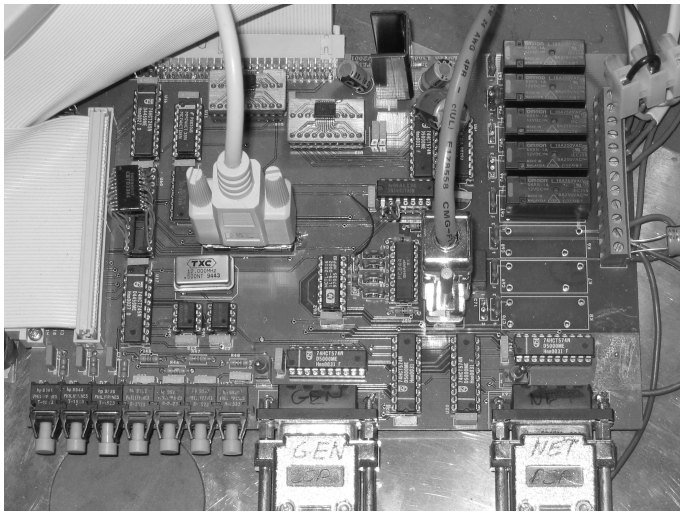

Fig. 13.8. Photograph of the digital interface board.

The pulses from the encoder are handled by a 16-bit Decoder/Counter Interface IC (HCTL-2016). The encoder is galvanically isolated from the digital board by optocouplers and the power supply to the encoder is fed through an isolated DC-DC converter (NME0505s). The encoder counter increments a register when a Ch_A pulse is followed by a Ch_b pulse. The register is reset by the encoder zero pulse. There is a 8-bit parallel interface to the DSP. The high byte is read first and then the low byte. The result is then processed in the software.

13.6.3 Analogue board

On the analogue board, there are three A/D converters with six 16-bit sigma delta converters each (AD73360 from Analog Device). The external clock frequency of the A/D converters is 16.384 MHz (MCLK), that is reduced by a factor of two internally. The internal sampling rate of the sigma delta modulator is then 1.024 MHz. With the desired sampling frequency of 4 kHz the group delay of each channel is 373 μs.

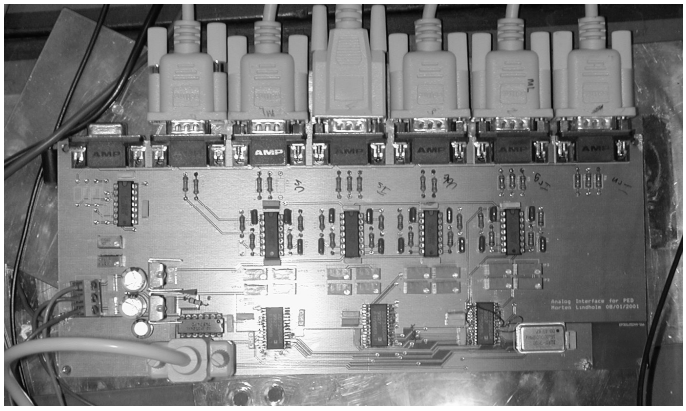

Fig. 13.9. Photograph of the analogue interface with the AD-converters.

In front of each channel on the A/D converters, there is a single pole anti-aliasing filter with a cut-off frequency at 33 kHz. The filter causes a 5μs lag at 4kHz. The filters are made with an op-amp, so the gain of the signal and the DC offset of the signal are fitted with the input range of the A/D converter. The A/D converters have a serial interface, so all three A/D converters are connected in cascade. The clock frequency of the serial port is a quarter of MCLK. The signals from A/D converter#1 go through A/D converter#2 and A/D converter#3 and then to the SPORT in the DSP. This is also the case with the signals from A/D converter#2, which only passes through A/D converter#3. This setup is practical from a wire count perspective, but when three times six 16-bit signals have to be clocked into a SPORT, the disadvantages of the cascade connection become obvious. It takes a minimum of 36 μs, and each sampling period

is equal to 250 μs at $F_s = 4$ kHz. The delays of signal measurements added together give a total of 415 μs (T_{delay}), so when the data is used in the control loop they are about 1.7 T_{samp} old. This will caurse some distortion in the control system, and should be taken care of in the control loop.

In a redesign of the measurement circuit some changes may be required. Instead of using the same sampling frequency as the switch frequency, a high speed A/D converter circuit with digital filter implemented in the DSP would be better.

14

Software

The software developed for the laboratory setup is made with the software environment Visual DSP++® from Analog Device©. Nearly all the programming code is written in the programming language C. This gives an overhead compared to Assembly code, due to processor stack operations. The code optimization is enabled in the compiler and the code produced is quite efficient. A few routines are made in the Assembly language. Programming in Assembly is a long and complicated process, when making programs for new developments. When the fact that C-code is not the fastest is accepted, the disadvantages with programming in C are negligible. The biggest advantage using C-code is a reduction in the development time. Another thing is software up dates. It can be quite a job to work on somebody else's old Assembly code, whereas C-code is often easier to understand right away.

14.1 Program Structure

The structure of the program is controlled by interrupts. As described earlier, there are different interrupt levels. The sampling rate of the analog measurements is 4 kHz, the signals are transmitted to the DSP by a serial port and buffered in a cyclic serial port buffer with 18 entries. Whenever the buffer is full, a serial port interrupt is raised. This interrupt calls the control loop, because whenever the buffer is full all measured signal are ready. When analyzing this setup one of the things to point out is the

fact that this serial port interrupt is completely synchronous, due to some variations in the conversion time of A/D converters. The time variation was not measured.

Table 14.1. The priority of the top six interrupts.

Priority	Sig value	Definition
0	SIG_SOVF	Status stack or loop stack overflow
1	SIG_TMZ0	Timer=0 (high priority)
2	SIG_VIRPTI	Vector interrupt
3	SIG_IRQ2	Interrupt 2
4	SIG_IRQ1	Interrupt 1
5	SIG_IRQ0	Interrupt 0 push button

After initialization of parameters and the A/D converters, the program starts and the serial port interrupt calls the control loop function (*sport_int*). In order to continue with the program, the user is required to push the IRQ_0 button. This will call the *interface* function, which contains a case sequence which increments the value of the variable *state*. Increments of the *state* variable occur every time IRQ_0 is called, but also sometimes within the control loop. The higher value of the *state* variable the more funtions of the control loop is used. Figure 14.1 shows how the different *states* in the program are managed.

In the beginning of the project, the case sequence was convenient to use for debugging, since one hit on the IRQ_0 button would only allow the DSP to start the DC-link precharge. Another hit would close the grid main contactor and so on. Each of the outer arrows in Fig 14.1 is an increment of *state* variable either done by raising IRQ_0 or just by changing the value in the control loop in order to move on. The inner arrows are all is due to some kind of fault that has raised one of the other two hardware interrupts IRQ_1 or IRQ_2.

14.1.1 Program Flow

The flow of the program as shown in Fig 14.1 is described here. First the DC-link precharge contactor is closed, whereafter the DC-link is charged through resistors. When the total voltage $U_{DC} > 500$V, the contactor for the grid inverter is closed. The grid side controller takes over and ramps U_{DCref} up to 680V. The grid inverter is then ready. Magnetizing of the generator can start, but only if the speed is above 1100 RPM. If not the rotor voltage will force U_{dc} above the maximum allowed value. The rotor

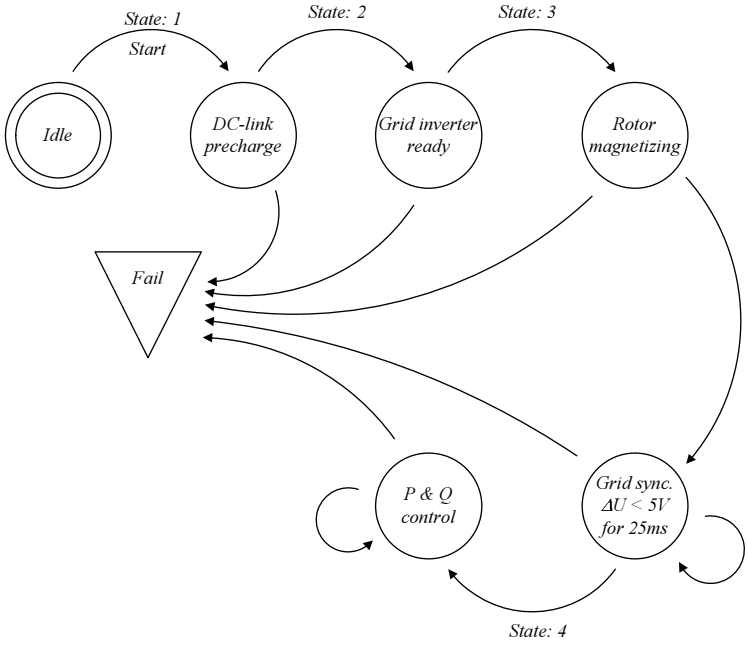

Fig. 14.1. Flow chart of the main program.

voltage is ramped up until the voltage magnitude of the grid $|\vec{u}_{grid}|$ and the stator $|\vec{u}_{stator}|$ are equal. Next $\vec{u}_{rotor}$ is phase shifted until the $\vec{u}_{stator}$ is in phase with $\vec{u}_{grid}$. Now the stator contactor closes and the DFIG is connected to the grid. Active and reactive power control are now tasks for the *dq*-control in the rotor inverter. No matter what state the program is in, it is always possible to exit the program in case of a failure. The

four input flags wired to push buttons are used for changing variables, e.g. control references P_{s-ref}.

A set of ten parameter is logged at the end of the program function and the data are stored in SDRAM on the EZ-LAB board. The parameters are logged for the final four seconds before program termination. Many of the results presented in the next chapter were measured in this way.

14.2 Controller Dynamics

All the controllers implemented in the software are PI-controllers (Proportional-integral). The controller consists of a gain and an integrator, the last in order to avoid stationary errors. There is no derivative element since that would amplify the disturbances, such as higher harmonics and quantization noise.

The transfer function for the PI-controller is [71]

$$D(z) = K\frac{\left(1+\frac{T_s}{2\tau_i}\right)-\left(1-\frac{T_s}{2\tau_i}\right)z^{-1}}{1-z^{-1}} \tag{14.1}$$

It has a pole at $z_p = 1$ and a zero at $z_z \simeq 1 - \frac{T_s}{\tau_i}$

Equation 14.1 can be changed to:

$$D(z) = K\left(\left(1+\frac{T_s}{2\tau_i}\right)+\frac{1}{\tau_i}\cdot\frac{T_s z^{-1}}{1-z^{-1}}\right) \tag{14.2}$$

The PI controllers are implemented as functions, using two arguments: the error and a structure with the parameters and the integral value [72].

14.3 Digital Filters

Two types of filters are used in the software. As mentioned on p28 the Hilbert filters used to extract the postitve sequence of the voltage signals are implemented as high order FIR filters . The FIR filter can be used as a standard function by this expression

```
Vabch[0] = fir(Vabc[0], hilbert_coeffs, hilbert_states0, 401);
```

The coefficients are saved in the second argument and the filter states in the third argument. In order to get unity gain at 50Hz, a 400th order filter is used.

The other type of filters used are the IIR filters. A set of 4th order low pass Butterworth filters with different cut off frequencies are implemented. Again here a standard function is used

```
omega_r=iir(omega_r,a_100_4,b_100_4,encoder_states,4);
```

The IIR filter uses both numerator and denominator coefficient.

In the initial programming phase of the project, most of the measurements where filtered through one of these Butterworth filters. The result was slow response time and problems with the control system. At the end, the filters were only used at two incidents: To filter the speed signal, here a 100 Hz filter was used, and to filter grid and stator voltages in the synchronous rotating reference frame in order to make synchronization. The stator voltage signals are only used for synchronization, and the grid voltage signal are not used filtered in the control loop.

The use of digital filters is convenient, but with a setup where the signals are sampled with the same frequency as the switch frequency, the effect is limited.

14.4 Space Vector Modulation

The software implementation of the space vector modulation is done in the same way as it was described functionally in chapter 8.

Both timers are used, one for each converter. There is only one high priority timer interrupt, and both timers are set to trigger the high timer interrrupt. A sticky bit in the CNT_EXP0 register in the DSP is either set or cleared depending on which timer ended. This bit can then be read to detect which timer ended.

14.5 Neutral Point Balancing

The neutral point balancing algorithm is used in both the grid side and the rotor side inverter, except during some specific measurements. The fourth digit in the switch vector table, column five, in Appendix B stores the information about which phase the neutral point current comes from. The following code is used to select the right switch vector in order to minimize DC neutral point variations,

```
for (i=0; i<=2; i++){
  ..
  NP = states[u0[i]]>>12;//shifts to extract NP curr.
  if (NPL > 0 ){
    if ((NP == 1) & (In[2] < 0))      u0[i]=u0[i]+4;
    else if ((NP == 2) & (In[0] < 0)) u0[i]=u0[i]+4;
    else if ((NP == 3) & (In[1] < 0)) u0[i]=u0[i]+4;
    }
  else if (NPL < 0 ){
    if ((NP == 1) & (In[2] > 0))      u0[i]=u0[i]+4;
    else if ((NP == 2) & (In[0] > 0)) u0[i]=u0[i]+4;
    else if ((NP == 3) & (In[1] > 0)) u0[i]=u0[i]+4;
    }
  }
```

The code shown above is for the grid side inverter, but the rotor side code is identical.

15

Measurements

In this chapter, the measurements made on the laboratory model are presented. As already mentioned, the DSP are programmed to log ten variables for four seconds, or fewer variables for a longer time period. This function was widely used to get data for documentation. It was also useful in the debugging phase. Other measurements were made using an oscilloscope, and some with a power analyzer. The measurements were made at two locations.

The first location was at the Technical University of Denmark in Lyngby. Here the $\text{THD}_{voltage}$ was equal to 4-5% during most of the time the measurements were captured. The voltage harmonics were mainly 5th, 7th, 11th and 13th.

The second location was in Hammel, Denmark at NEG Micon Control Systems. The $\text{THD}_{voltage}$ was about 0.5% during measurements. Also here the distortion was due to 5th, 7th, 11th and 13th harmonics. The measurements were taken before the laboratory equipment was connected to the grid.

Since the grid in Hammel was so much better, I hoped this would yield measurements with a really low distortion in the current. In reality the laboratory setup performed in almost the same way in Hammel as it had done in Lyngby. The setup was moved to Hammel at the end of the project period, because the laboratory setup was financed by NEG Micon Control Systems. Most of the figures presented in this chapter and also previous

chapters are showing measurements from Lyngby. If a Figure show data from Hammel, it is stated.

15.1 General Measurements

15.1.1 DC-link Charge

Figure 15.1 shows a time trace for DC-link charging of both DC sources. The precharge contactor is closed at $t = 0$. After about 5 s, the main contactor is closed. When the sum of both sources U_{DC} is above 560 V, the *dq*-controllers take over. The lower graph shows the charge current. Even with a precharge, the current spikes are rather high, though only a third of the nominal current.

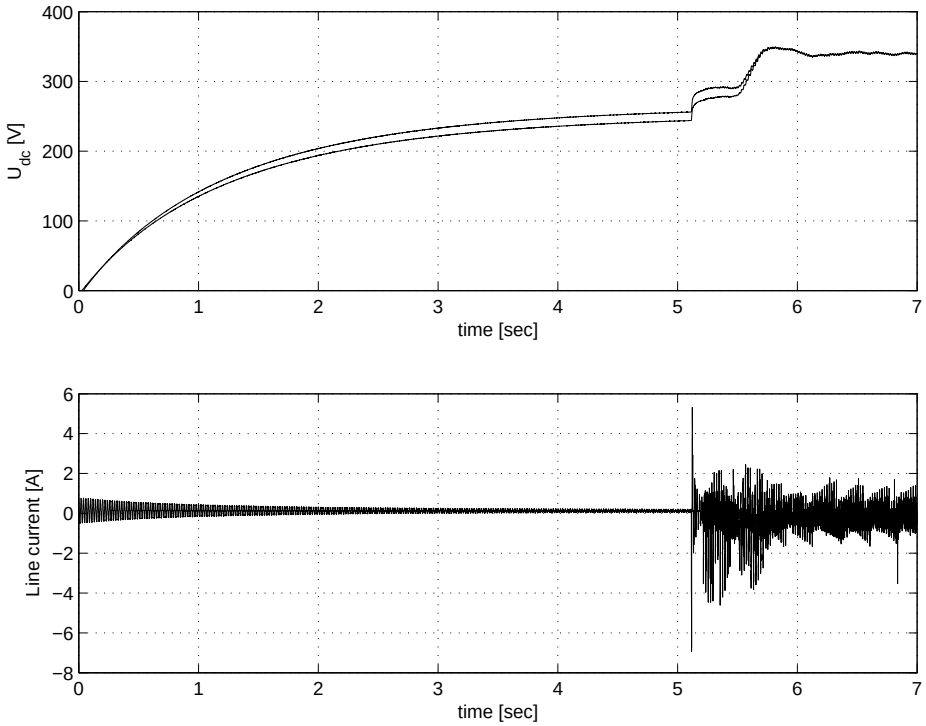

Fig. 15.1. Time trace of DC-link precharge.

15.1.2 Phase and Line Voltages

Figure 15.2 shows the phase voltage of the grid inverter, clearly showing the third harmonic, due to the use of SVM. The measurement is done with an oscilloscope with some averaging enabled. If symmetrical, the third harmonic cancels out with the other phases. This measurement is done without neutral point balancing on the grid inverter in order to show the phase voltage with the theoretically correct zero sequence.

The converter line voltage is displayed in Fig. 15.5. Here there is barely any third harmonic in the line voltage. The same measurements (not shown here) were done when both inverters were taking part in the neutral point balancing. In this case, a lack of control over the third harmonic was apparent.

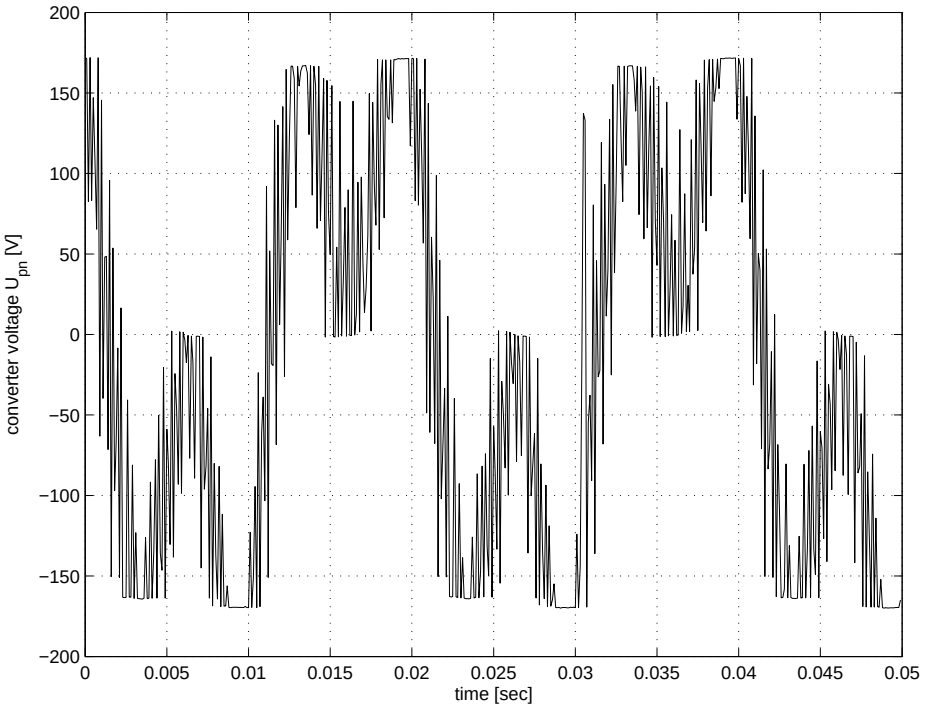

Fig. 15.2. Converter phase to zero voltage.

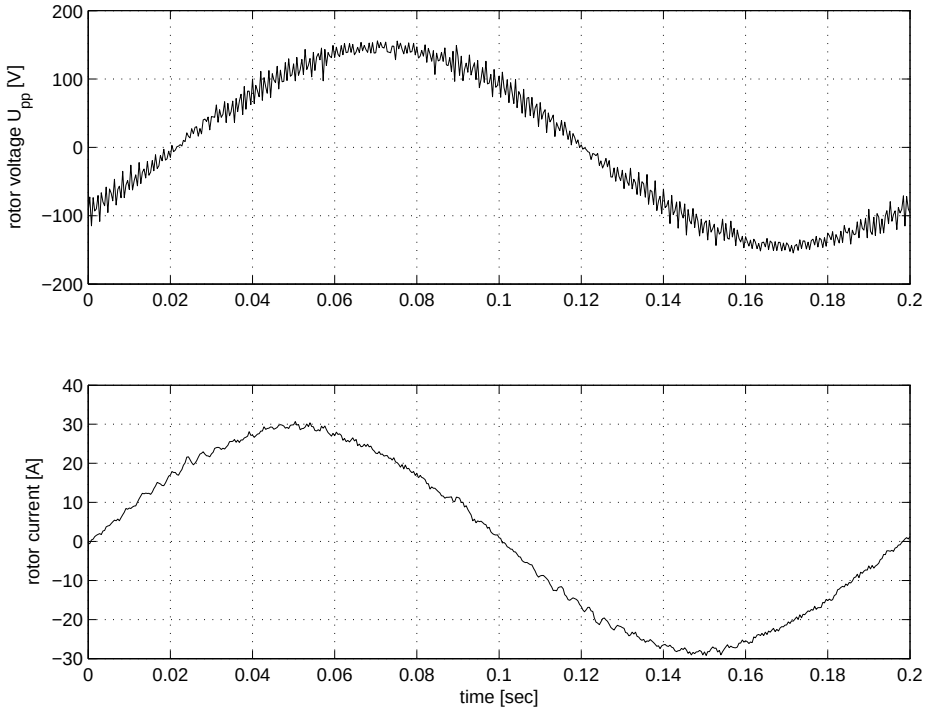

Fig. 15.3. Rotor voltage and current measured with $P_s = 25kW$, 10% slip.

15.1.3 Rotor Measurements

Figure 15.3 shows the rotor voltage and current with 10% slip, meaning that the fundamental frequency of the signals is 5 Hz. Unfortunately, the two measurements are not in phase. The stator power was 25 kW at the time of the measurements. The harmonic content of the current signal can be seen in Fig. 15.14.

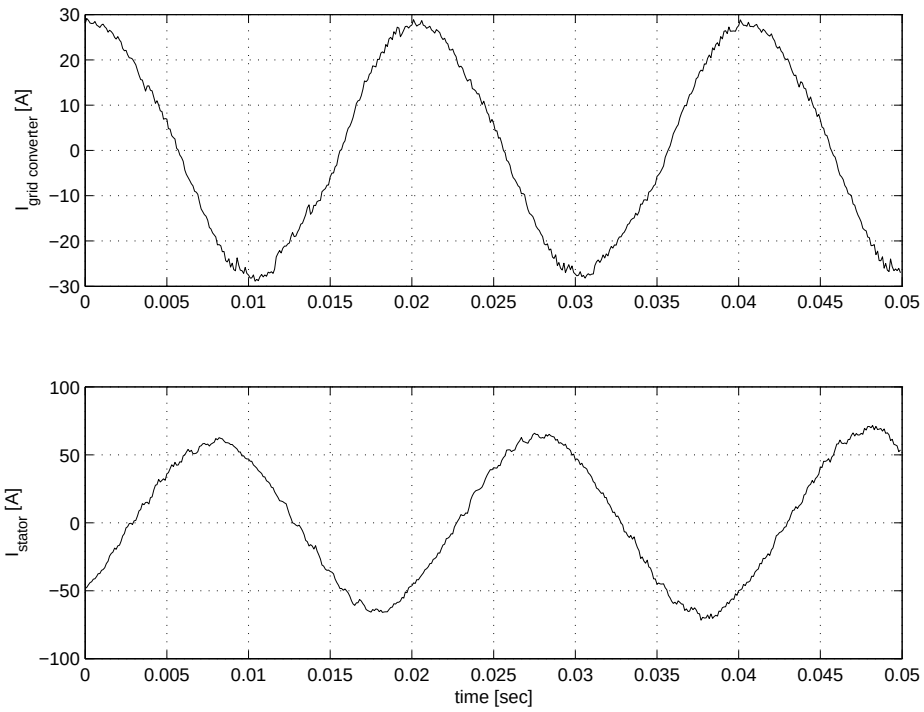

Fig. 15.4. Stator and grid inverter current measured with adaptive filter, 1350 RPM.

15.1.4 Grid Inverter Measurements

Figure 15.4, upper graph, shows the grid inverter current when the inverter is running in inductive mode. The reason for not running the grid side converter in capacitive mode, which would be most obvious, is that the amount of capacitive reactive power is limited by the selected DC voltage level. In order to produce a current close to the specification limit, the inverter is running with low modulation index. The lower graph shows the stator current. The active power from the stator is 27 kW and is consuming 16 kVar. Again, the two measurements are not in phase. The harmonic content of the grid current signal can be seen in Fig. 15.17.

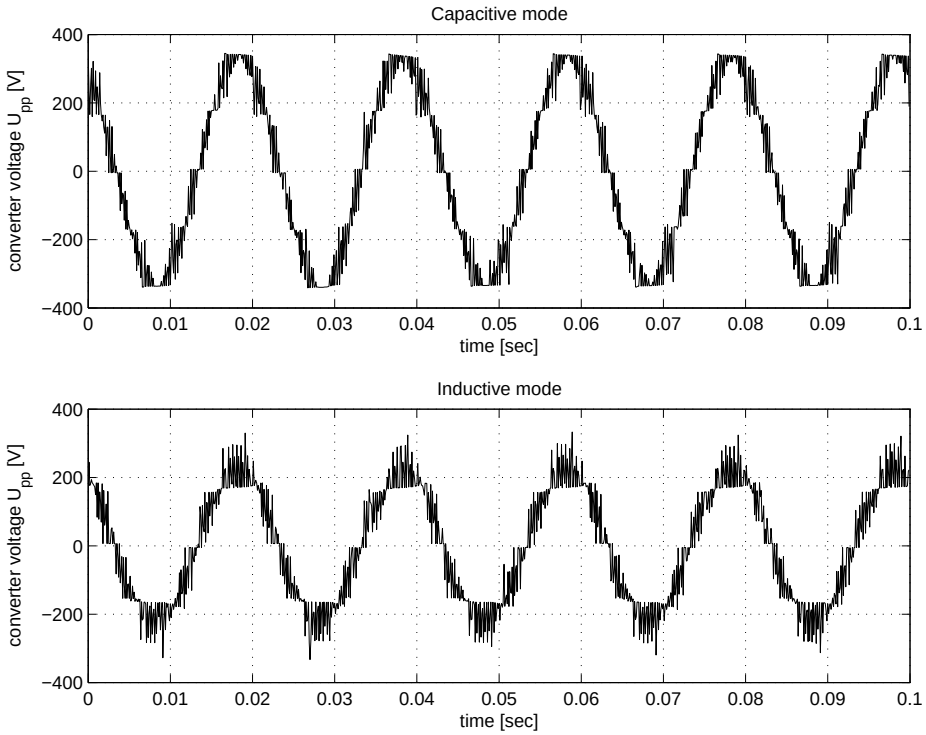

Fig. 15.5. Converter voltages, with the grid side converter working as a STATCOM.

15.2 Reactive Power Compensation with the Grid Converter

In Fig. 15.5, the active power from the DFIG is zero, and the grid side converter is running as a pure static VAr compensator (STATCOM). In the lower graph, the converter is in inductive mode, consuming 12 kVAr, and running with low modulation index. The upper graph shows the converter voltage in capacitive mode supplying the grid with 12 kVAr and running with high modulation index.

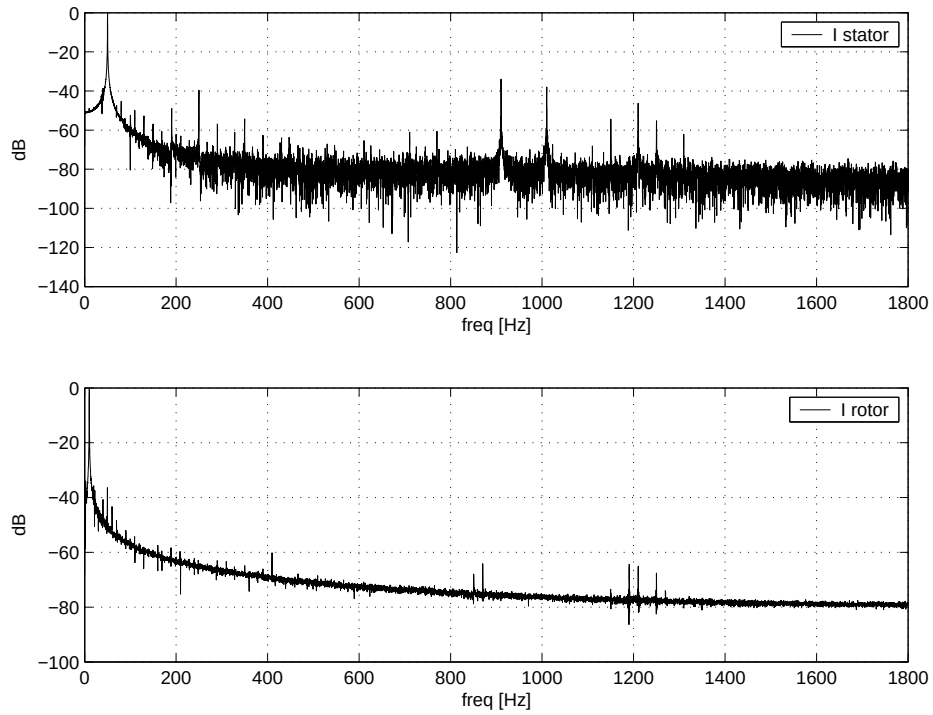

Fig. 15.6. Frequency spectrum of rotor current and stator current, with the stator connected to resistors, $I_s = 6A$. Speed =1200 RPM.

15.3 Generator Measurements without Grid Connection

In search of the origin of harmonics in the generator parameters, some measurements were made without the stator connected to the grid. Some of them are on p92 in Fig. 11.2, 11.4 and 11.5. In Fig. 11.2, the generator is running at synchronous speed. The figure shows that the rotor side inverter is magnetizing the generator with DC current. The spectrum of the stator voltage has only harmonics that refer to the slot harmonics. There are first order slot harmonics at 1200±50 Hz and another set of higher order slot harmonics at 1500±50 Hz. In Fig. 15.6, the stator terminals are connected to resistors so a current can flow. The stator slot harmonics are still present. Now the 5th and 7th harmonics are also present. The frequency of the rotor current is 10 Hz.

15.4 Step Responses

To show the performance of the different controllers, a set of step responses are made.

The induction motor that produces the shaft torque is running in speed control mode, i.e. the motor and frequency converter try to maintain a given speed reference, as oppose to torque control mode, where the frequency controller tries to control the shaft torque at a given reference. In a variable speed wind turbine two means of control are used: One is controlling the blade pitch, another is controlling the rotor speed. The controller outputs are a pitch demand and a torque demand. The torque demand is the reference input to the DFIG rotor side converter (i_{qr_ref}). As already mentioned the other reference input (i_{dr_ref}) controls the reactive power from the generator by controlling the magnetizing.

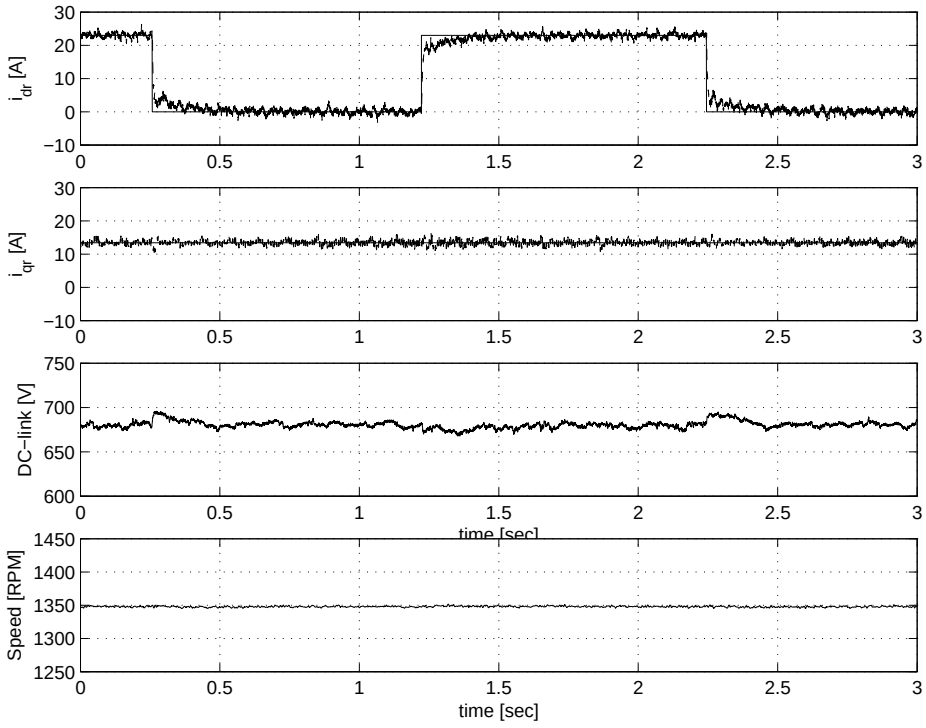

Fig. 15.7. Step variation in the rotor current direct axis.

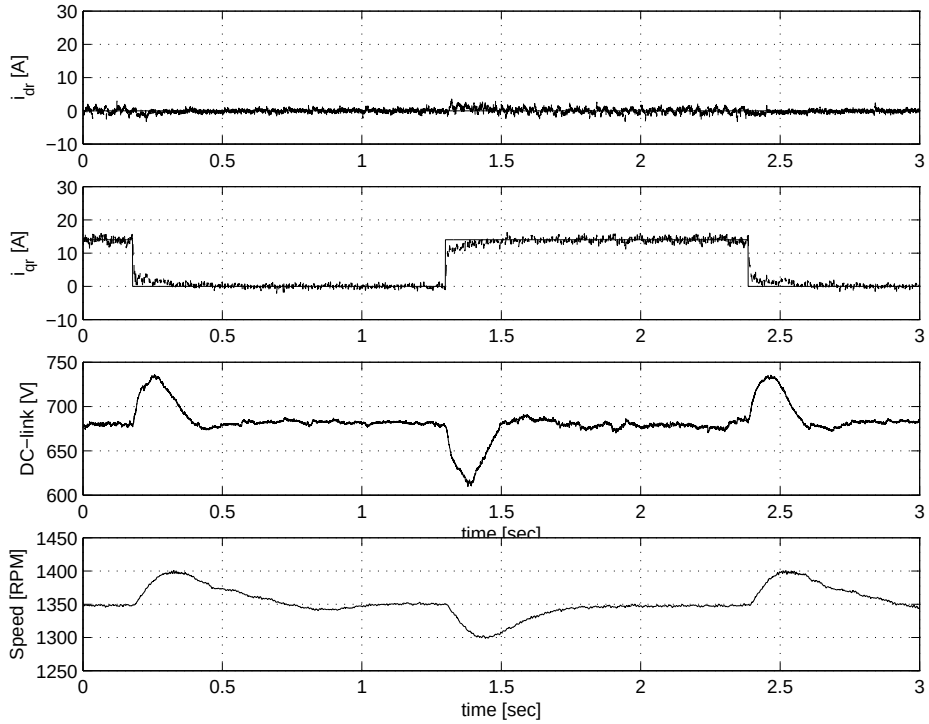

Fig. 15.8. Step variation in the rotor current quadrature axis.

15.4.1 Step in Rotor Current Reference

In the vector control chapter, the differential equations for the DFIG (9.18) are found. These equations show that the step response for both i_{dr} and i_{qr} will result in nearly the same response time. This was tested. The step response for i_{dr} is shown in Fig. 15.7. The figure shows that i_{dr} follows the step in reference, while i_{qr} is maintained at its constant reference value. The DC voltage changes, more than expected, but is still within the limit of being considered constant.

Figure 15.8 shows the step response for i_{qr}. The figure shows that i_{qr} follows its reference, while i_{dr} shows some sign of being coupled with i_{qr}. The DC voltage makes rather big changes when active power is changed. This could be due to a slow controller in the grid inverter, or due to the fact that the load motor is having a hard time following the reference speed. The latter theory is supported by the speed plot. Still, it does not

explain the errors in the DC voltage. This should have been controlled by the grid inverter.

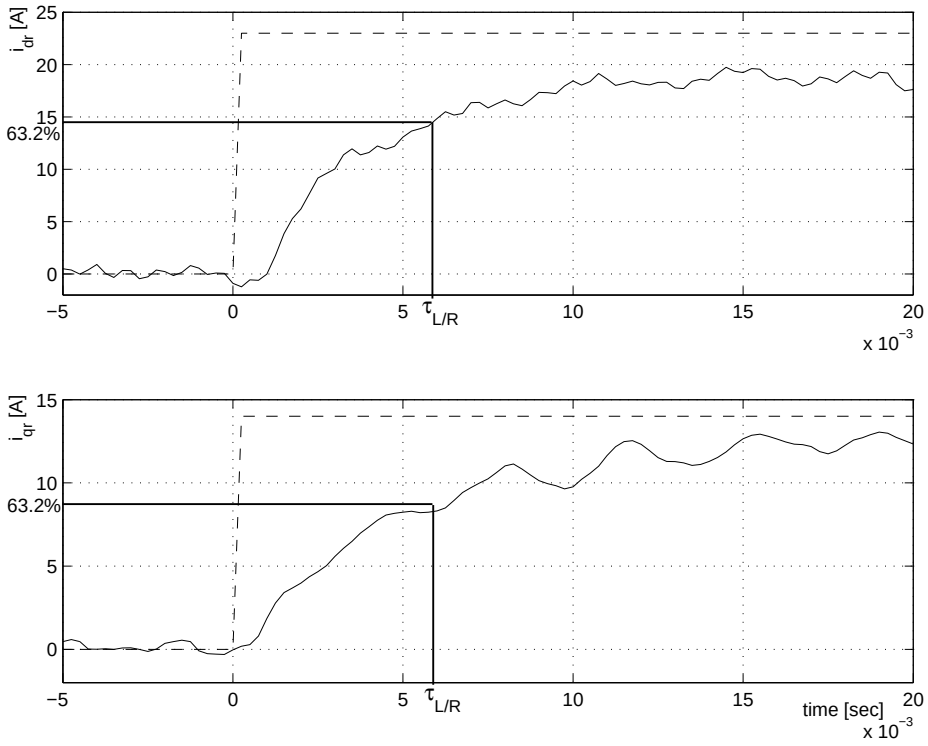

Fig. 15.9. Step responses for d and q zoom of Fig. 15.8 and 15.7.

Figure 15.9 shows the two steps enlarged. The dotted lines are the references, and the thicker black lines shows where 63% of the reference values are, i.e. the time constant τ. Here it is clear that both currents respond with nearly the same time constant $\tau \simeq 6.6$ ms for both curves. The height of the step responses are different, because the largest step allowed for i_{dr} and i_{qr} are used. The time constant is a combination of the time delay T_{delay} (p120) and the transient time constant of the generator σT_r.

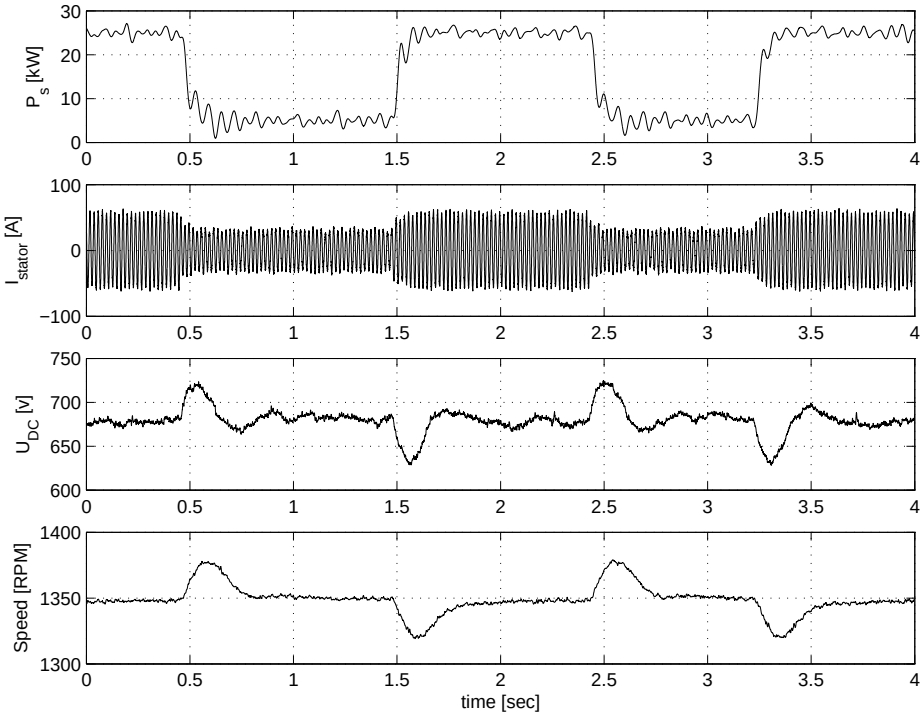

Fig. 15.10. Step response for P_s, 5kW to 25kW, at 1350 RPM.

15.4.2 Step in power reference

As already discussed, the control system can be extended so instead of controlling i_{dr} and i_{qr} directly, an extra control loop can be added, so the input references are the active and reactive power. The time constant for the outer loop is normally larger than for the inner loop (i_{dr}- and i_{qr}-loop). It is often not desirable to have too fast of a response in the power, due to disturbances. Figure 15.10 shows a step response for P_s where the reference is stepped from 5 kW to 25 kW several times. As one could have expected, the graphs show the same weakness as in Fig. 15.8. The time constant is larger than for the outer loop. The second graph shows the stator current.

15.5 Speed Changes

Until now, all the data presented are measured at constant speed. To check the performance of the laboratory model at any allowed speed, some measurements are made while the speed ramps through the speed range.

Figure 15.11 shows a speed variation from 20% to -20% slip. The middle graph shows the relation from (5.2), where the grid side power is proportional to the slip of the generator. The lower graph shows the rotor current. It is clear to see how the rotor frequency changes as a function of the magnitude of the slip. It show that the converter supplies a DC current to the generator around synchronous speed (1500 RPM), i.e. the generator is magnetized from the rotor side. The graph looks like a plot of the stator current of a normal inverter fed induction motor/generator, with around 20% speed reversal.

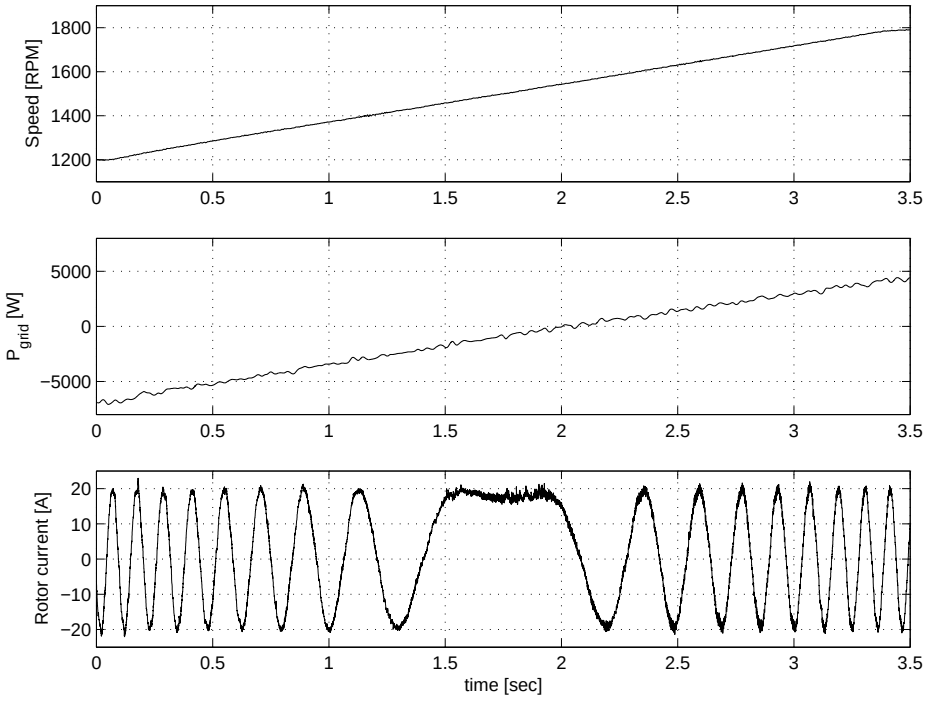

Fig. 15.11. Speed charge 1200 rpm -1800 rpm

Figure 15.12 shows another speed variation, where the speed is ramped down from 10% to -10% slip. The first three graphs show the same as Fig. 15.11 while the fourth graph shows that stator power is kept constant during the speed change. The DC voltage drops 10 volts during the speed changing period. Balance of the neutral point is shown in the last graph.

Running the generator near synchronous speed puts a lot of stress on the neutral point balancing, but here it is far from being unstable during the slip reversal.

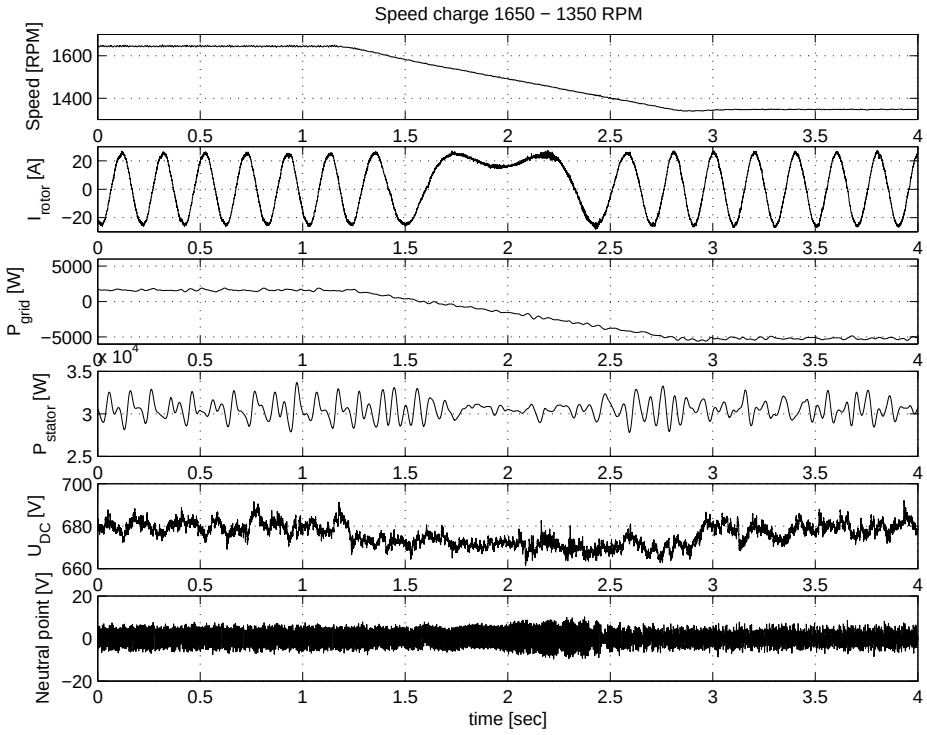

Fig. 15.12. Speed change 1650 - 1350 RPM

15.6 Losses & Efficiency

The slip relation of the DFIG generator described in (5.2) is clearly only true for the ideal lossless system. In a real system, the losses shift the

P_{grid} curve in Fig. 15.11 down. The lossless system would have $P_{grid} = 0$ at synchronous speed.

15.6.1 Generator losses

The generator losses are first of all copper losses due to conduction of the current. Additionally there are a set of losses in the iron due to hysteresis and eddy current Finally, there is a small loss in the dielectrica.

Externally, the generator fan requires some energy as well. In this case, the fan is directly driven on the same shaft, resulting in a higher shaft torque.

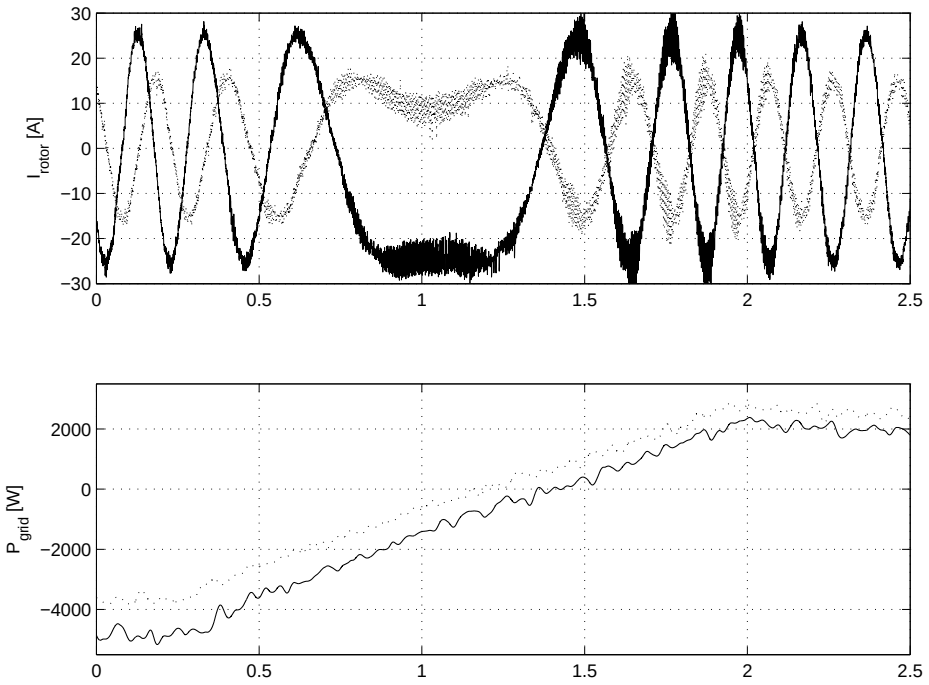

Fig. 15.13. Difference between P_{grid} and I_r with rotor magn. (solid) and stator magn. (dotted) (measured in Hammel)

15.6.2 Converter losses

The direct converter losses can be grouped into switching and conduction losses. The indirect losses are due to losses in the DC-link and the filter inductors.

The conduction loss for an IGBT is given by

$$P_{conduction} = I_{C\_av} U_{CE} + I^2_{C\_rms} R_{CE} \tag{15.1}$$

Similar expressions can be found for free wheeling and clamp diodes by substituting the appropriate values.

The switching losses are the product of the actual energy loss of each on and off switching multiplied by the switching frequency

$$P_{switch} = (E_{on} + E_{off}) f_{sw} \tag{15.2}$$

The efficiency of the converters is measured with a power analyzer (Voltech PM3000). With a load of 2-4 kVA, the efficiency is around 96% from the DC-link to either side AC. The total losses in the back to back are about 8% of the total apparent power.

15.6.3 Rough explanation of the losses

The study of the losses for this DFIG system is performed in order to show that the slip relation (5.2) is only valid for an ideal lossless system. Performing an accurate study of the losses for this system would not contribute to the understanding of the DFIG system, it would only be a tedious process.

Some of the losses can be clarified by using two sets of measurements. One with the generator magnetized from the stator and one where magnetizing comes from the rotor. By doing so, the rotor winding in the first case will only have to carry the current from the active slip power, whereas in the second case, the winding will carry a much larger current. Figure 15.13 shows how P_{grid} shifts depending on where magnetizing of the generator comes from. The measurements are similar to Fig. 15.12, but with increasing speed instead. The entire set of measurements are to be found

in Fig. E.2 and E.3. In the sub-synchronous range the difference in P_{grid} is about 1.2 kW, and in the super-synchronous range it is about 0.5 kW. Figure 15.13 also shows the rotor current for both cases. The two signals are measured on the same rotor phase, but the speed change does not occur in phase within the two measurements. The noise in the current signal after 1.2 sec. is because the adaptive filters are not settled yet. To overcome this, the μ factor (12.5) in the LMS algorithm has to be higher.

Whether the total losses are reduced by magnetizing the generator from the rotor or from the stator is a question that should be studied in detail for the specific generator/inverter configuration.

15.7 Current Measurements

The last set of measurements investigates the adaptive filters. As described in chapter 12, the purpose of the filters is to reduce the harmonics in the

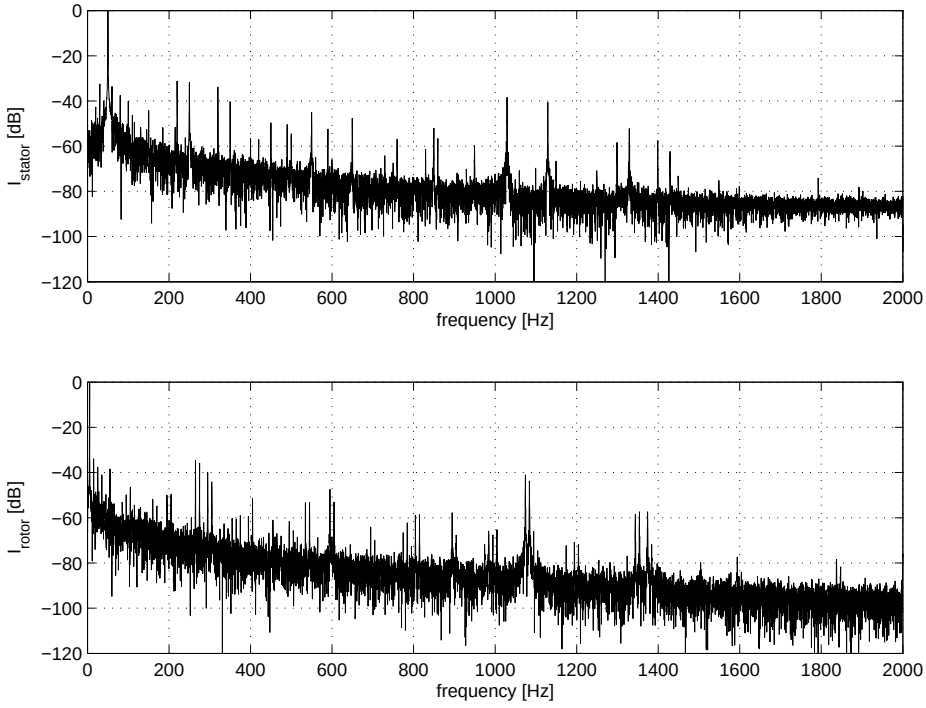

Fig. 15.14. Spectrum stator and rotor current, speed: 1350 RPM

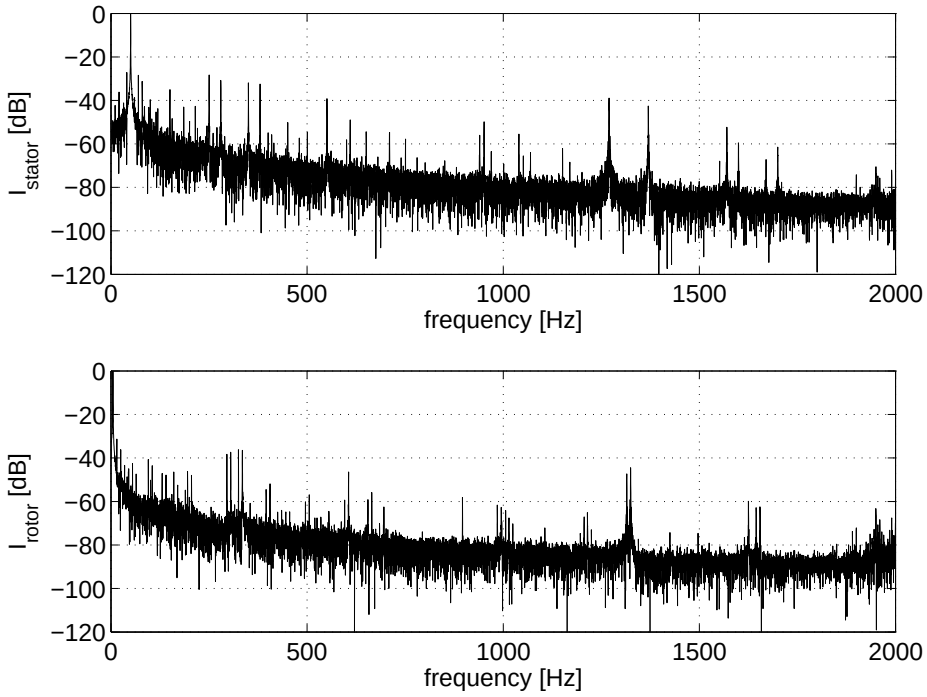

Fig. 15.15. Spectrum stator and rotor current, speed: 1650 RPM

stator current and in the grid converter current. In the stator current, a reduction of the 5th and 7th harmonics and the 5th and 7th slip harmonics is sought.

Figure 15.14 shows a frequency spectrum with a rotor speed of 1350 RPM equal to 10% slip without the adaptive filter. The stator power is 25 kW. The most dominant harmonics in the stator current are the 5th at 250 Hz and the 5th slip harmonic at 220 Hz, followed by the 7th and the 7th slip harmonics at 320 Hz with a 10% slip. The two spikes at 1080±50 Hz are slot harmonics.

Similarly in Fig. 15.15, the rotor speed has changed to supersynchronous speed at 1650 RPM equal to -10% slip. The 5th and 7th harmonics are still present, and the two slip harmonics have moved to 280 Hz and 380 Hz, respectively, still without the filter. The slot harmonics are now at 1320±50 Hz according to (11.3).

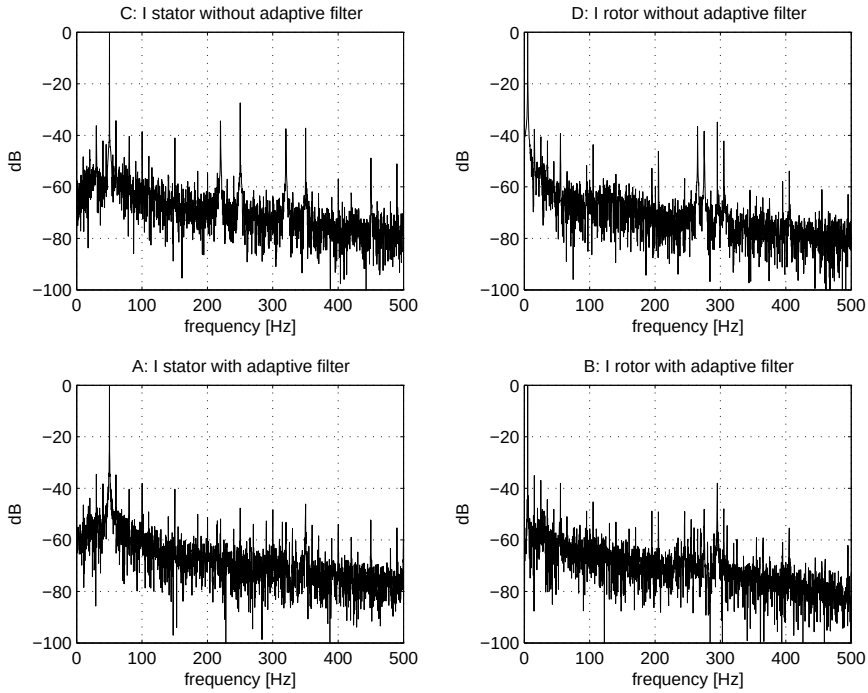

Fig. 15.16. Current spectrums w. & w.out adaptive filtering at 1350 RPM (10% slip)

15.8 Adaptive filtering

15.8.1 Rotor Converter

To show the effect of the filter Fig. 15.16 shows a frequency spectrum from 0-500Hz of the rotor and stator currents with and without the adaptive filter, where the graphs without the filter are an enlargement of Fig. 15.14 and Fig. 15.15. The figure shows a reduction of the 5th and 7th harmonics in the stator current by about 20dB. The slip harmonics are reduced by about 30dB. It is not a goal to get the lowest distortion in the rotor current, instead the primary goal must be to get the lowest distortion in the stator current, which might result in some distortion in the rotor side.

15.8.2 Grid Converter

Finally, Fig. 15.17 shows the frequency spectrum of the grid side current. On the upper graph, there are no adaptive filters implemented. The lower

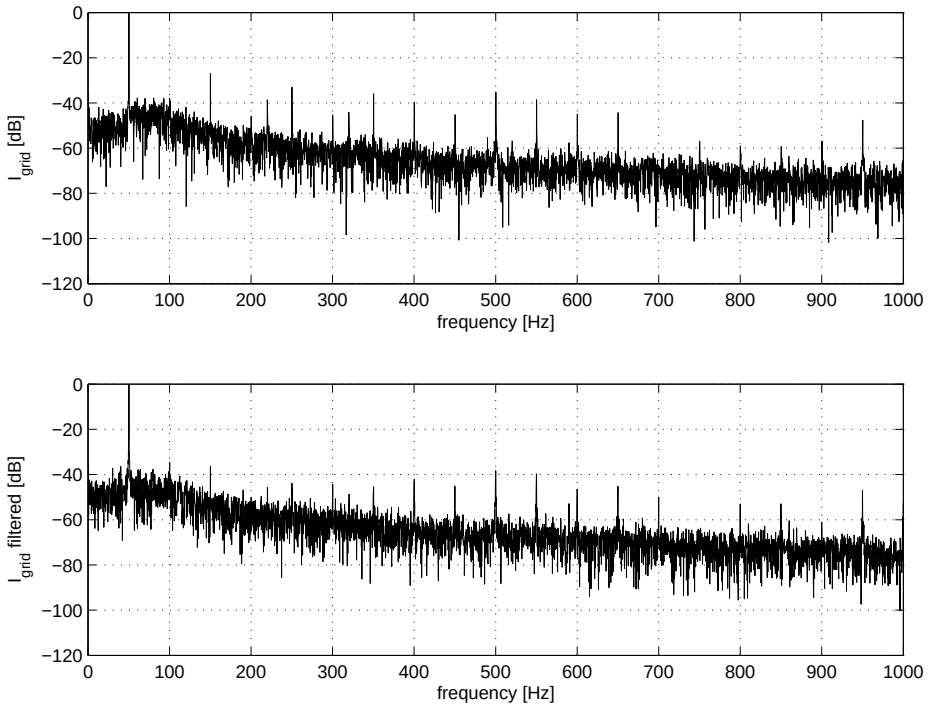

Fig. 15.17. Spectrum of the grid side current without and with adaptive filter.

graph shows the spectrum of the grid current with the adaptive filter. The graph shows a 10dB reduction in the 3rd, 5th and 7th harmonics, which are the harmonics that are sought reduced.

A 10dB reduction is barely worth implementing the filters. Other means to reduce the harmonics may be more efficient. As mentioned earlier, a control system with a high sampling rate is preferred. Many of the low order harmonics should not even be present in the signals due to the switch frequency, but with the reference frame transformations, some distortion is introduced. These kind of circles in the control loops cause more distortion.

16

Conclusion

In this thesis, control of a doubly fed induction generator has been investigated. In order to do so, a full scaled running laboratory model has been implemented. A back to back 3-level NPC inverter with space vector modulation is implemented together with the generator.

DC-link balancing, where zero sequence injects into the voltage of either one or both inverters, results in uncontrolled 3rd harmonics. That fact makes multilevel inverters less attractive for use together with DFIG machines, since zero sequence injected at the rotor side becomes present at the stator side.

Using the same sampling and switch frequency makes it difficult to use digital filters in the software, due to delays in the filters.

Proof and verification, that the transient time constant, σT_r for both the direct and quadrature current is the same, are presented. This makes it possible to change the flow of reactive power from the generator as fast as the active power flow.

Adaptive active filters are used to reduce harmonics in the stator current and in the grid side inverter current. A method for using the rotor side inverter to reduce stator harmonics has been presented, and verified experimentally. The method gives an easy and reliable way to eliminate or reduce harmonics from the DFIG generator. Even the slip harmonics that varies in frequency was reduced. The implementation of the adaptive filter in the rotor side converter gives a fairly good reduction in the harmonic frequencies applied.

Further Research

The topics in the thesis are not at all a complete coverage of the field of DFIG generator systems for wind turbine applications. There are still many topics to do further work on, a few of them are listed below.

Sensorless Control

The use of an encoder or other types of position sensors causes always a risk of some mechanical failure. Therefore sensorless control would be desirable. During start-up, some problems could occur with sensorless control due to lack of information.

Grid Faults

How the wind turbines react during grid faults is one of the most important questions to be answered. The demands from the utility companies are moving towards a situation where the turbines must stay connected to the grid no matter what happens on the grid.

Crowbar

During grid faults, some sort of equipment is required to get rid of the energy stored in the generator. This can be a thyristor-controlled crowbar or a switched crowbar using IGBTs. It is important that the crowbar is fast and reliable.

References

[1] S. Heier, *Grid Integration of Wind Energy Conversion Systems*, John Wiley Sons, 1998.

[2] Marian P. Kazmierkowski, R. Krishnan, and Frede Blaabjerg, *Control in Power Electronics*, Academic Press, 2002.

[3] Ned Mohan, Tore M. Undeland, and William P. Robbins, *Power Electronics: Converters, Applications and Design*, Wiley, 2nd edition, 1995.

[4] G. F. Franklin, J. D. Powell, and A Emami-Naeini, *Feedback Control of Dynamic Systems*, Addison-Wesley, 2nd edition, 1991.

[5] W. Leonhard, *Control of Electrical Drives*, Springer Verlag, 2nd edition, 1997.

[6] Bent Rasmussen and Flemming Øster, "Power production from the wind", in *Wind Energy in Denmark, research and technological development, 1990.*

[7] Per Lundsager Helge Petersen Peter S. Andersen, Ulrik Krabbe, *Basismateriale for Beregning af Propelvindmller*, Forsøgsanlæg Risø, 1980.

[8] E·on Netz GmbH, "Ergänzende netzanschlussregeln für windenergieanlagen", 2001.

[9] International Electrotechnical Commision, "Iec 61400-21, wind turbine generator systems - part 21: Measurement and assessment of power quality characteristics of grid connected wind turbines", Tech. Rep., IEC, 2000.

[10] Åke Larsson, *The Power Quality of Wind Turbines*, PhD thesis, Chalmers University of Technology, 2000.

[11] Åke Larsson, Poul Sørensen, and Fritz Santjer, "Grid impact of variable-speed wind turbines", *European Wind Energy Conference 1999. Proceedings of the*, 1999.

[12] J. Proakis and D. Manolakis, *Digital Signal Processing*, Macmillan Publishing Company, 2nd edition, 1992.

[13] B. Hopfensperger and D.J. Atkinson, "Doubly-fed a.c. machines: classification and comparison", *9th European Conference on Power Electronics and Applications. EPE 2001*, p. 17 pp., 2001.

[14] R. Pena, J.C. Clare, and G.M. Asher, "A doubly fed induction generator using back-to-back pwm converters supplying an isolated load from a variable speed wind turbine", *Electric Power Applications, IEE Proceedings-*, vol. 143, no. 5, pp. 380–387, 1996.

[15] R. Pena, J.C. Clare, and G.M. Asher, "Doubly fed induction generator using back-to-back pwm converters and its application to variable-speed wind-energy generation", *Electric Power Applications, IEE Proceedings-*, vol. 143, no. 3, pp. 231–241, 1996.

[16] R.S. Pena, R. Cardenas, G.M. Asher, and J.C. Clare, "Vector control strategy of a harmonic and reactive power compensator", *EPE'97. 7th European Conference on Power Electronics and Applications*, pp. 848–53 vol.4, 1997.

[17] S. Muller, M. Deicke, and R.W. De Doncker, "Adjustable speed generators for wind turbines based on doubly-fed induction machines and 4-quadrant igbt converters linked to the rotor", *Conference Record of the 2000 IEEE Industry Applications Conference. Thirty-Fifth IAS Annual Meeting and World Conference on Industrial Applications of Electrical Energy (Cat. No.00CH37129)*, pp. 2249–54 vol.4, 2000.

[18] B. Eggert, "1.5 mw wind power station with low ac-line distortion using a standard doubly-fed generator system with field orientation control", *EPE'97. 7th European Conference on Power Electronics and Applications*, pp. 739–42 vol.2, 1997.

[19] A.K. Wallace, R. Spee, and G.C. Alexander, "The brushless doubly-

fed machine: its advantages, applications and design methods", *Electrical Machines and Drives, 1993. Sixth International Conference on*, pp. 511–517, 1993.

[20] L. Xu, F. Liang, and T.A. Lipo, "Transient model of a doubly excited reluctance motor", *Energy Conversion, IEEE Transaction on*, vol. 6, no. 1, pp. 126–133, 1991.

[21] P. C. Krause, *Analysis of Electric Machinery and Drive Systems*, Wiley Interscience, 2002.

[22] Peter Vas, *Sensorless Vector and Direct Torque Control*, Oxford University Press, 1998.

[23] D. W. Novotny and T. A. Lipo, *Vector Control and Dynamics of AC Drives*, Oxford University Press, 1996.

[24] A. Zuckerberger, E. Suter, C. Schaub, A. Klett, and P. Steimer, "Design, simulation and realization of high power npc converters equipped with igcts", *Industry Applications Conference, 1998. Thirty-Third IAS Annual Meeting. The 1998 IEEE*, vol. 2, pp. 865 –872 vol.2, 1998.

[25] Leon M. Tolbert and Fang Z. Peng, "Multilevel converters for large electric drives", *Conference Proceedings - IEEE Applied Power Electronics Conference and Exposition - APEC*, vol. 2, pp. 530–536, 1998.

[26] D.M. Divan, "The resonant dc link converter-a new concept in static power conversion", *Conference Record of the 1986 IEEE Industry Applications Society Annual Meeting (Cat. No.86CH2272-3)*, pp. 648–56 vol.1, 1986.

[27] Per Karlson, *Quasi Resonant DC Link Converters*, PhD thesis, Lund Institute of Technology, 1999.

[28] Fang Zheng Peng, Jih-Sheng Lai, J. McKeever, and J. VanCoevering, "A multilevel voltage-source inverter with separate dc sources for static var generation", *Industry Applications Conference, 1995. Thirtieth IAS Annual Meeting, IAS '95., Conference Record of the 1995 IEEE*, vol. 3, pp. 2541 –2548 vol.3, 1995.

[29] A. Nabae, I. Takahashi, and H. Akagi, "A new neutral point clamped pwm inverter", *IEEE Transactions on Industry Applications*, vol.

IA-17, no. 5, pp. 518–23, 1981.

[30] Xiaoming Yuan and I. Barbi, "A new diode clamping multilevel inverter", *Applied Power Electronics Conference and Exposition, 1999. APEC '99. Fourteenth Annual*, vol. 1, pp. 495–501 vol.1, 1999.

[31] T.A. Meynard and H. Foch, "Multi-level choppers for high voltage applications", *EPE Journal*, vol. 2, no. 1, pp. 45–50, 1992.

[32] M.D. Manjrekar and T.A. Lipo, "A hybrid multilevel inverter topology for drive applications", *Applied Power Electronics Conference and Exposition, 1998. APEC '98. Conference Proceedings 1998., Thirteenth Annual*, vol. 2, pp. 523–529 vol.2, 1998.

[33] L. Helle and S. Munk-Nielsen, "Comparison of converter efficiency in large variable speed wind turbines", *APEC 2001. Sixteenth Annual IEEE Applied Power Electronics Conference and Exposition (Cat. No.01CH37181)*, pp. 628–34 vol.1, 2001.

[34] O. Al-Naseem, R.W. Erickson, and P. Carlin, "Prediction of switching loss variations by averaged switch modeling", *Applied Power Electronics Conference and Exposition, 2000. APEC 2000. Fifteenth Annual IEEE*, vol. 1, pp. 242–248 vol.1, 2000.

[35] J. Holtz, "Pulsewidth modulation-a survey", *Industrial Electronics, IEEE Transactions on*, vol. 39, no. 5, pp. 410–420, 1992.

[36] D.G. Holmes, "The general relationship between regular-sampled pulse-width-modulation and space vector modulation for hard switched converters", *Industry Applications Society Annual Meeting, 1992., Conference Record of the 1992 IEEE*, pp. 1002–1009 vol.1, 1992.

[37] B.P. McGrath, D.G. Holmes, and T.A. Lipo, "Optimised space vector switching sequences for multilevel inverters", *Applied Power Electronics Conference and Exposition, 2001. APEC 2001. Sixteenth Annual IEEE*, vol. 2, pp. 1123–1129, 2001.

[38] A.M. Hava, R.J. Kerkman, and T.A. Lipo, "Simple analytical and graphical methods for carrier-based pwm-vsi drives", *Power Electronics, IEEE Transactions on*, vol. 14, no. 1, pp. 49–61, 1999.

[39] A.M. Hava, R.J. Kerkman, and T.A. Lipo, "A high performance generalized discontinuous pwm algorithm", *Applied Power Electronics Conference and Exposition, 1997. APEC '97 Conference Proceedings 1997., Twelfth Annual*, vol. 2, pp. 886–894 vol.2, 1997.

[40] N. Celanovic and D. Boroyevich, "A fast space-vector modulation algorithm for multilevel three-phase converters", *Industry Applications, IEEE Transactions on*, vol. 37, no. 2, pp. 637–641, 2001.

[41] Nikola Celanovic, *Space Vector Modulation and Control of Multilevel Converters*, PhD thesis, Virginia Polytechnic Institute an State University, 2000.

[42] Dongsheng Zhou and D.G. Rouaud, "Experimental comparisons of space vector neutral point balancing strategies for three-level topology", *Power Electronics, IEEE Transactions on*, vol. 16, no. 6, pp. 872–879, 2001.

[43] F. Wang, "Coordinated control of regenerative three-level neutral point clamped pwm voltage source inverters", *Industry Applications Conference, 2002. 37th IAS Annual Meeting. Conference Record of the*, vol. 1, pp. 537–543, 2002.

[44] Nikola Celanovic and Dusan Borojevic, "Comprehensive study of neutral-point voltage balancing problem in three-level neutral-point-clamped voltage source pwm inverters", *Conference Proceedings - IEEE Applied Power Electronics Conference and Exposition - APEC*, vol. 1, pp. 535–541, 1999.

[45] F. Wang, "Sine-triangle vs. space vector modulation for three-level pwm voltage source inverters", *Conference Record of the 2000 IEEE Industry Applications Conference. Thirty-Fifth IAS Annual Meeting and World Conference on Industrial Applications of Electrical Energy (Cat. No.00CH37129)*, pp. 2482–8 vol.4, 2000.

[46] S. Ogasawara and H. Akagi, "Analysis of variation of neutral point potential in neutral-point-clamped voltage source pwm inverters", *Industry Applications Society Annual Meeting, 1993., Conference Record of the 1993 IEEE*, pp. 965–970 vol.2, 1993.

[47] J Holtz, "Pulsewidth modulation for electronic power conversion (in-

vited paper)", *IEEE Proceedings*, vol. 82, no. 8, pp. 1194–1214, 1994.

[48] Dongsheng Zhou and D.G. Rouaud, "Dead-time effect and compensations of three-level neutral point clamp inverters for high-performance drive applications", *Power Electronics, IEEE Transactions on*, vol. 14, no. 4, pp. 782–788, 1999.

[49] A.B. Plunkett, "A current-controlled pwm transistor inverter drive", *Industry Application Society IEEE-IAS Annual Meeting*, pp. 785–92, 1979.

[50] K. Hasse, "Speed control methods for fast-reversing drives using controlled rectifier fed induction motors with squirrel-cage rotors", *Regelungstechnik und Prozess-Datenverarbeitung*, vol. 20, no. 2, pp. 60–6, 1972.

[51] F. Blaschke, "The principle of field orientation as applied to the new transvektor closed-loop control system for rotating-field machines", *Siemens Review*, vol. 39, no. 5, pp. 217–20, 1972.

[52] Morten Lindholm, "Digitalt reguleret reaktiv effekt kompensator", Master's thesis, Technical University of Denmark, 1997.

[53] M. Malinowski, M.P. Kazmierkowski, and A.M. Trzynadlowski, "A comparative study of control techniques for pwm rectifiers in ac adjustable speed drives", *Industrial Electronics Society, 2001. IECON '01. The 27th Annual Conference of the IEEE*, vol. 2, pp. 1114–1118 vol.2, 2001.

[54] Boon Teck Ooi and Bin Lu, "C-upfc: a new facts controller with 4 degrees of freedom", *2000 IEEE 31st Annual Power Electronics Specialists Conference. Conference Proceedings (Cat. No.00CH37018)*, pp. 961–6 vol.2, 2000.

[55] Michael Lindgren, *Modeling and Control of Voltage Source Converters Connected to the Grid*, PhD thesis, Chalmers University of Technology, 1998.

[56] Martin Bojrup, *Advanced Control of Active Filters in a Battery Charger Application*, PhD thesis, Lund Institute of Technology, 1999.

[57] Sang-Joon Lee, Jun-Koo Kang, and Seung-Ki Sul, "A new phase detecting method for power conversion systems considering distorted

conditions in power system", *Industry Applications Conference, 1999. Thirty-Fourth IAS Annual Meeting. Conference Record of the 1999 IEEE*, vol. 4, pp. 2167–2172 vol.4, 1999.

[58] V. Kaura and V. Blasko, "Operation of a phase locked loop system under distorted utility conditions", *Industry Applications, IEEE Transactions on*, vol. 33, no. 1, pp. 58–63, 1997.

[59] Su Chen and G. Joos, "A novel dsp-based adaptive line synchronization system for three-phase utility interface power converters", *Power Electronics Specialists Conference, 2001. PESC. 2001 IEEE 32nd Annual*, vol. 2, pp. 528–532 vol.2, 2001.

[60] Jan Svensson, *Grid-Connected Voltage Source Converter -Control Principles and Wind Energy Apllications*, PhD thesis, Chalmers University of Technology, 1998.

[61] V. Blasko, V. Kaura, and W. Niewiadomski, "Sampling of discontinuous voltage and current signals in electrical drives: a system approach", *Industry Applications, IEEE Transactions on*, vol. 34, no. 5, pp. 1123–1130, 1998.

[62] R. Carbone, A. Testa, D. Menniti, R.E. Morrison, and E. Delaney, "Harmonic and interharmonic distortion in current source type inverter drives", *Power Delivery, IEEE Transactions on*, vol. 10, no. 3, pp. 1576–1583, 1995.

[63] M. Yamamoto and O. Motoyoshi, "Active and reactive power control for doubly-fed wound rotor induction generator", *Power Electronics, IEEE Transactions on*, vol. 6, no. 4, pp. 624–629, 1991.

[64] A. Ferrah, P.J. Hogben-Laing, K.J. Bradley, G.M. Asher, and M.S. Woolfson, "The effect of rotor design on sensorless speed estimation using rotor slot harmonics identified by adaptive digital filtering using the maximum likelihood approach", *IAS '97. Conference Record of the 1997 IEEE Industry Applications Conference Thirty-Second IAS Annual Meeting (Cat. No.97CH36096)*, pp. 128–35 vol.1, 1997.

[65] Bernard Widrow and Marcian E. Hoff, "Adaptive switching circuits", *Wescon Conference Record*, pp. 96–104, 1960.

[66] Bernard Widrow and Samuel D. Stearns, *Adaptive Signal Processing*, Prentice-Hall, 1985.

[67] Jr. Glover, J.R., "Adaptive noise canceling applied to sinusoidal interferences", *IEEE Transactions on Acoustics, Speech and Signal Processing*, vol. ASSP-25, no. 6, pp. 484–91, 1977.

[68] V. Blasko, "Adaptive filtering for selective elimination of higher harmonics from line currents of a voltage source converter", *Industry Applications Conference, 1998. Thirty-Third IAS Annual Meeting. The 1998 IEEE*, vol. 2, pp. 1222–1228 vol.2, 1998.

[69] Intersil, "Hgtg20n120cnd data sheet", 1 1, 2000.

[70] Intersil, "Rhrp15100 data sheet", 1 1, 2000.

[71] Kurt Andersen, *samplede Reguleringssystemer (vol. 1 & 2)*, Servolaboratoriet, 1982.

[72] Torsten Lund, "Sensorless control of an induction machine", Master's thesis, Technical University of Denmark, 2001.

Part III

Appendices

Glossary of Symbols

λ	tip speed ratio
$\mathbf{W}$	weight function vector for LMS algorithm
$\mathbf{X}$	input signal vector for LMS algorithm
μ	adaptation gain
ω_1	fundamental frequency of the signal
ω	angular speed
ψ	flux linkage
ρ	mass density of air
$\sigma T_s, \sigma T_r$	stator and rotor transient time constants respectively
σ	leakage factor
θ	grid angle
θ_r	rotor angle
ε	LMS filter error
$\vec{i}_{ms}$	stator magnetizing current
A	area
a	complex spatial operator ($e^{j\frac{2\pi}{3}}$)
C_p	power performance coefficient
ga, gb, gc	grid phases
h	harmonic order
i_d, i_q	instantaneous values of direct- and quadrature-axis current in the rotating reference frame
i_α, i_β	instantaneous values of direct- and quadrature-axis current in the stationary reference frame

J	inertia of the rotor
j	complex operator
L	dynamic inductance
L_m	magnetizing inductance
L_r, L_{lr}	self- and leakage inductances of the rotor respectively
L_s, L_{ls}	self- and leakage inductances of the stator respectively
m	modulation index
MMF	Magneto Motive Force
N	number of turns
P	active power
$p = d/dt$	differential operator
Q	reactive power
R	resistance
ra, rb, rc	rotor phases
sa, sb, sc	stator phases
T	time constant
t_e	instantaneous value of the electromagnetic torque
T_s, T_r	stator and rotor time constants respectively
u_d, u_q	instantaneous values of direct- and quadrature-axis voltage in the rotating reference frame
u_α, u_β	instantaneous values of direct- and quadrature-axis voltage in the stationary reference frame
v_w	velocity of the wind
v_{tip}	blade tip speed
VAr	Volt Ampere reactive
w	weight function for LMS algorithm
x	input signal for LMS algorithm
FIR	Finite Impulse Response
IIR	Infinite Impulse Response

B

SVM look-up table

Table B.1. Look-up table used for SVM selection table

Switching State Table Location	Large Medium Vector U(g,h)	Small Switching vector U(g,h)	Switching State (phase)	HEX Switching Number	Small Vectors NP Currents
0	(0,-2)		002	0x33c	
1	(-1,-1)		012	0x36c	
2	(-2,0)		022	0x3cc	
3					
4					
5					
6					
7	(1,-2)		102	0x63c	
8		(0,-1)	001	0x3336	ic
9		(-1,0)	122	0x16cc	ia
10	(-2,1)		021	0x3c6	
11					
12		(0,-1)	112	0x66c	-ic
13		(-1,0)	011	0x366	-ia
14	(2,-2)		202	0xc3c	
15		(1,-1)	212	0x2c6c	ib
16			000	0x666	
17		(-1,1)	010	0x2363	ib
18	(-2,2)		020	0x3c3	
19		(1,-1)	101	0x636	-ib
20					
21		(-1,1)	121	0x6c6	-ib
22	(2,-1)		201	0xc36	
23		(1,0)	100	0x1633	ia
24		(0,1)	221	0x3cc6	ic
25	(-1,2)		120	0x6c3	
26					
27		(1,0)	211	0xc66	-ia
28		(0,1)	110	0x663	-ic
29					
30	(2,0)		200	0xc33	
31	(1,1)		210	0xc63	
32	(0,2)		220	0xcc3	

C

Rotating Machinery Data

Table C.1. generator specification: Leroy Somer FLSB 280S4 B3

Nominal values of the DFIG machine:		
Stator voltage (Y)	400	V
Stator current (Y)	88	A
Frequency (Hz)	50	Hz
Rotor speed	1481	RPM
Locked rotor voltage (Y)	1600	V
Power	40	kW
$\cos\phi$	0.72	
Weight	850	kg
DFIG parameters:		
Rotor resistance	0.04945	Ω
Stator resistance	0.028	Ω
Rotor leakage inductance	0.1726	mH
Stator leakage inductance	0.1591	mH
Mutual inductance	12.71	mH

Table C.2. load motor specification: ABB M2AA SMA 4

Nominal values of the load motor:		
Stator voltage (Δ)	400	V
Stator current (Δ)	68	A
Frequency (Hz)	50	Hz
Rotor speed	1480	RPM
Power	37	kW
cosϕ	0.84	
Weight	215	kg

D

Diagram of DSP interface

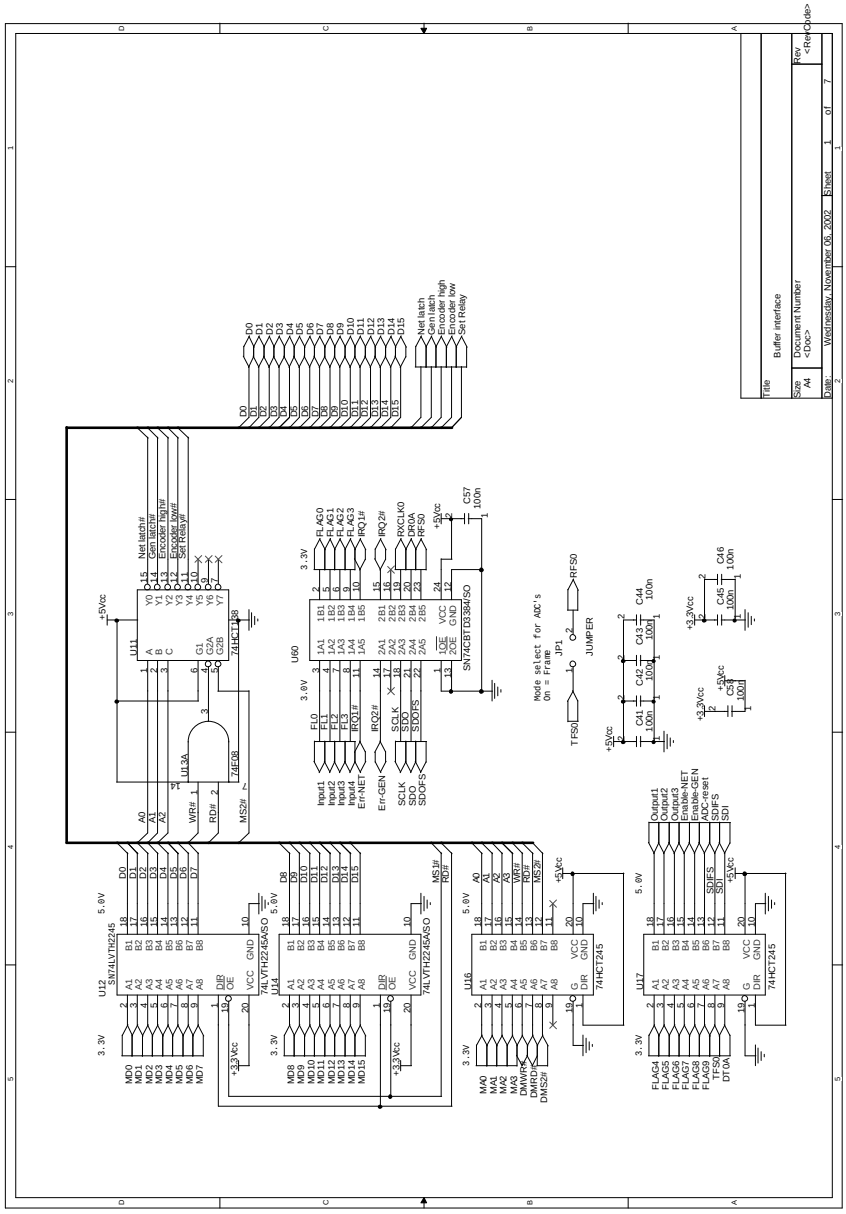

Fig. D.1. Buffer circuit

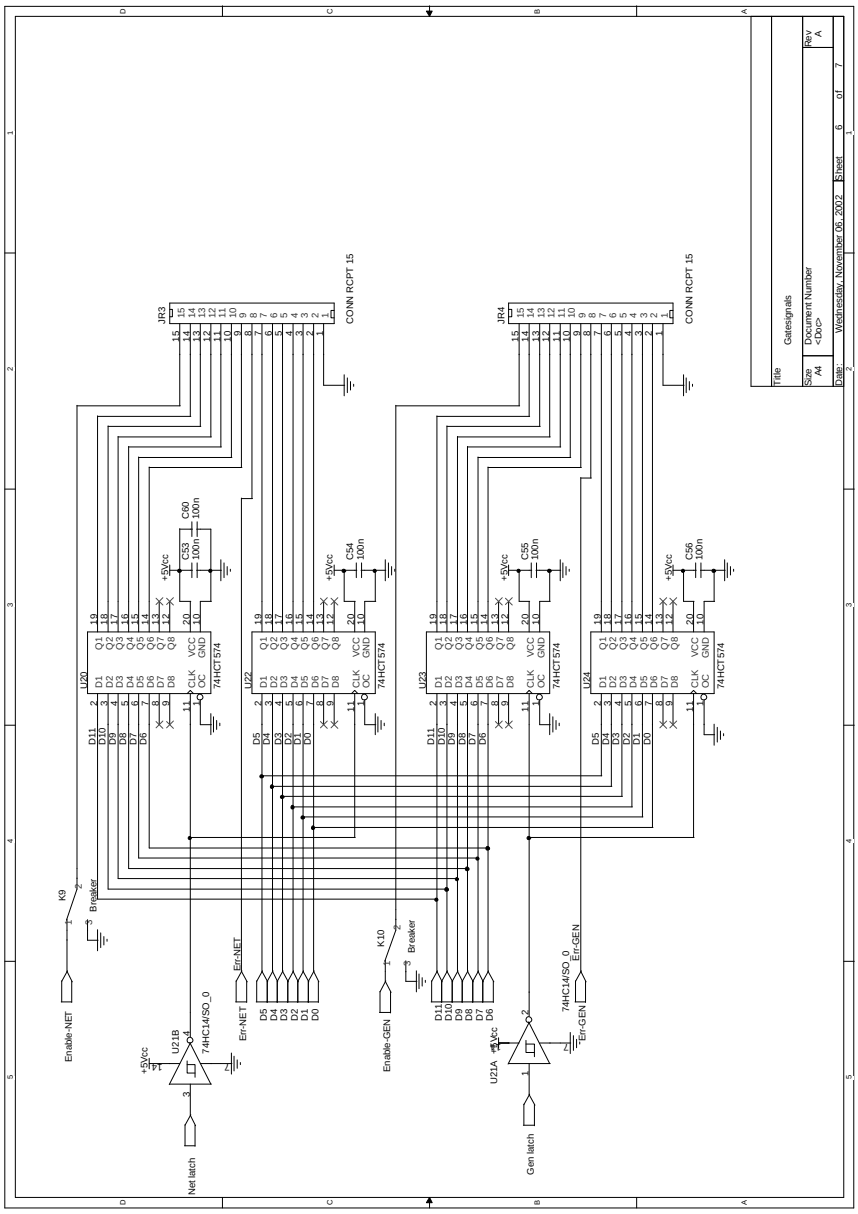

Fig. D.2. PWM latch

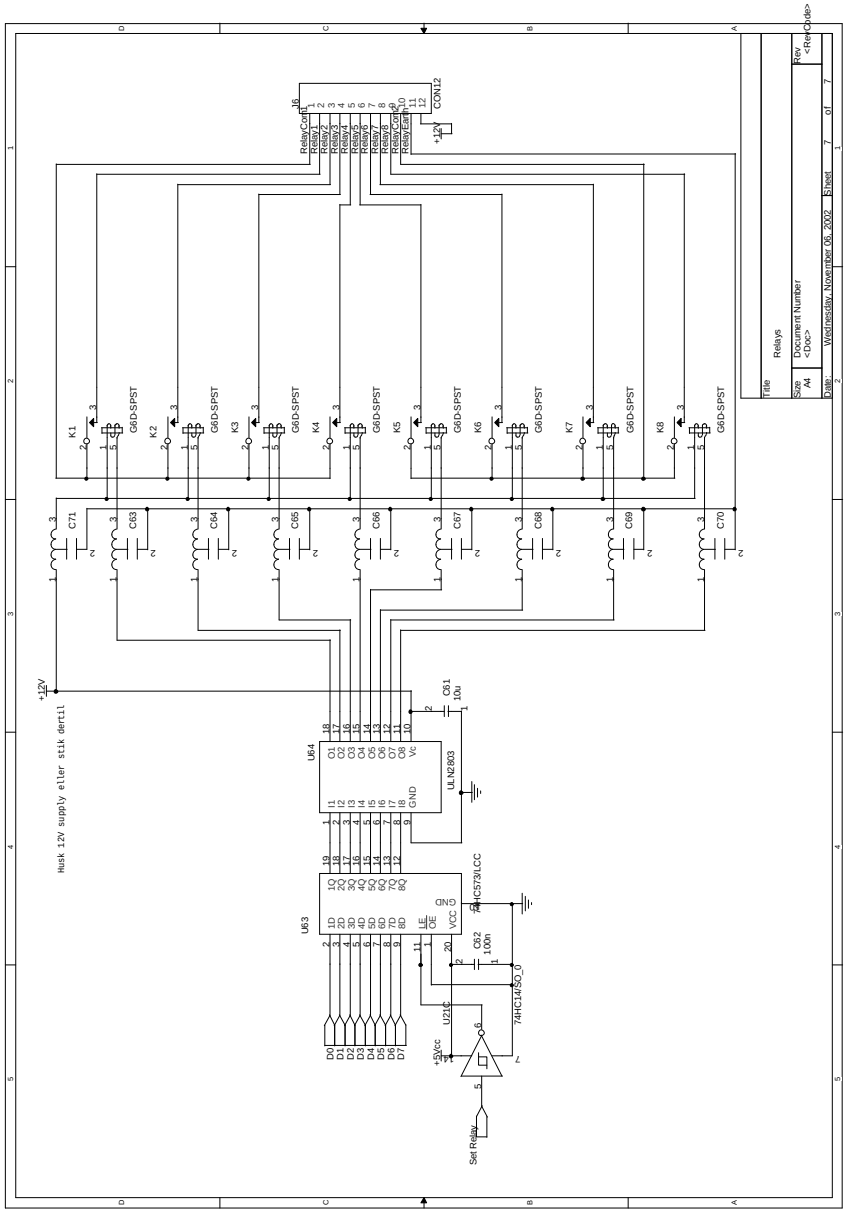

Fig. D.3. Relay outputs

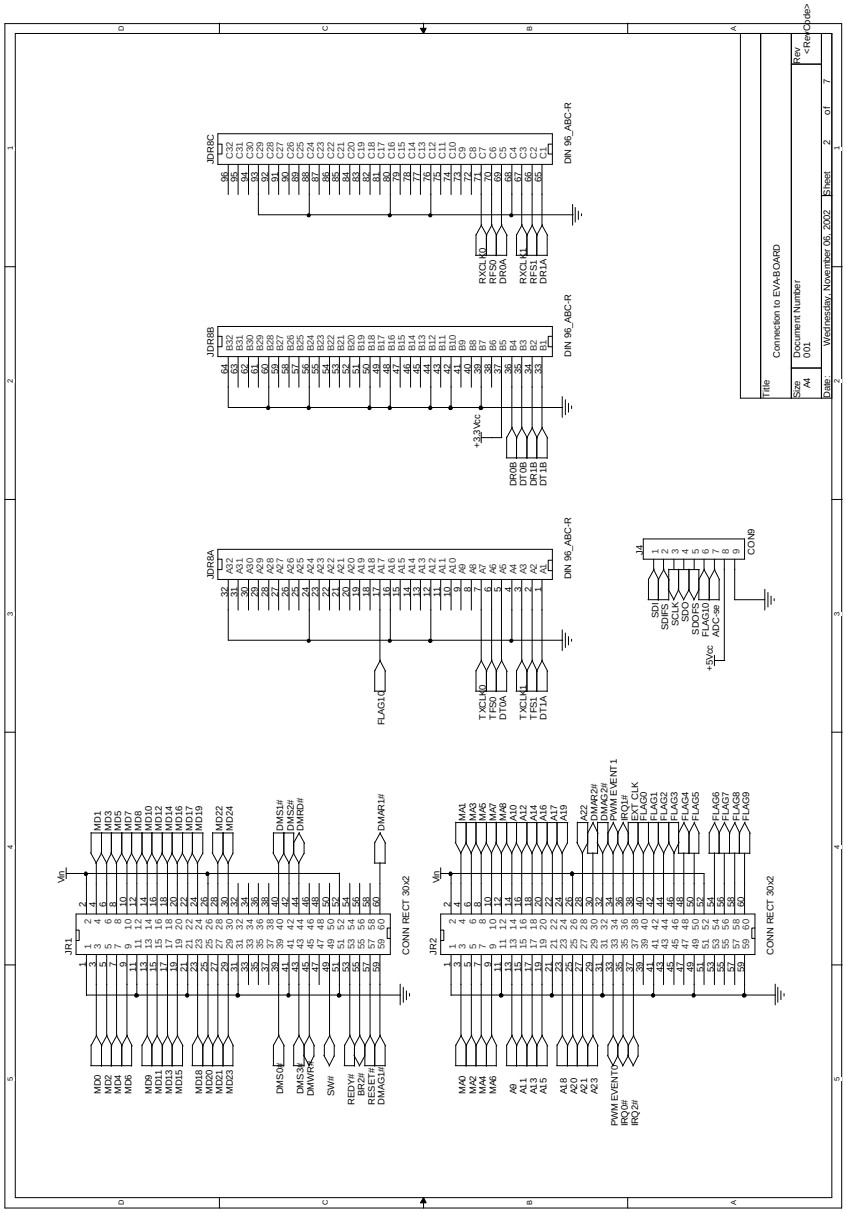

Fig. D.4. Connector diagram

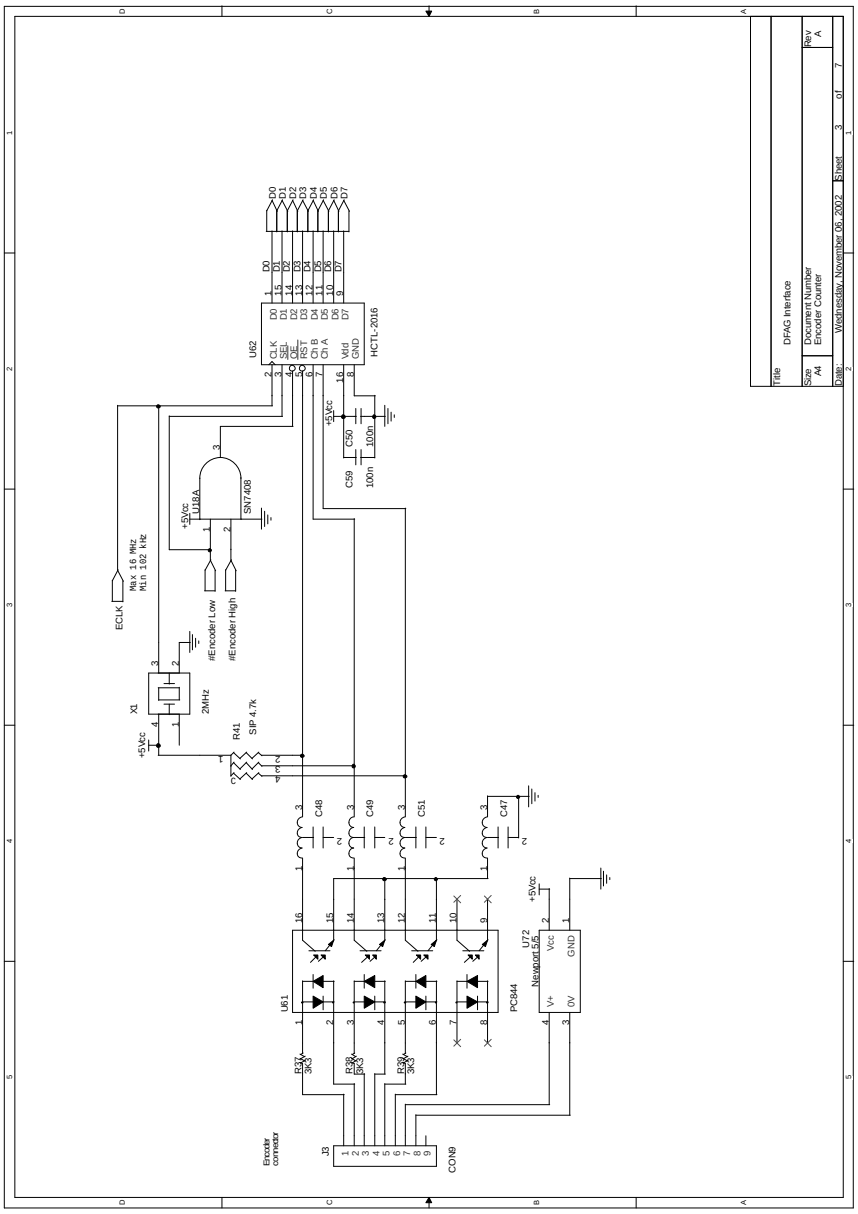

Fig. D.5. Encoder decoder circuit

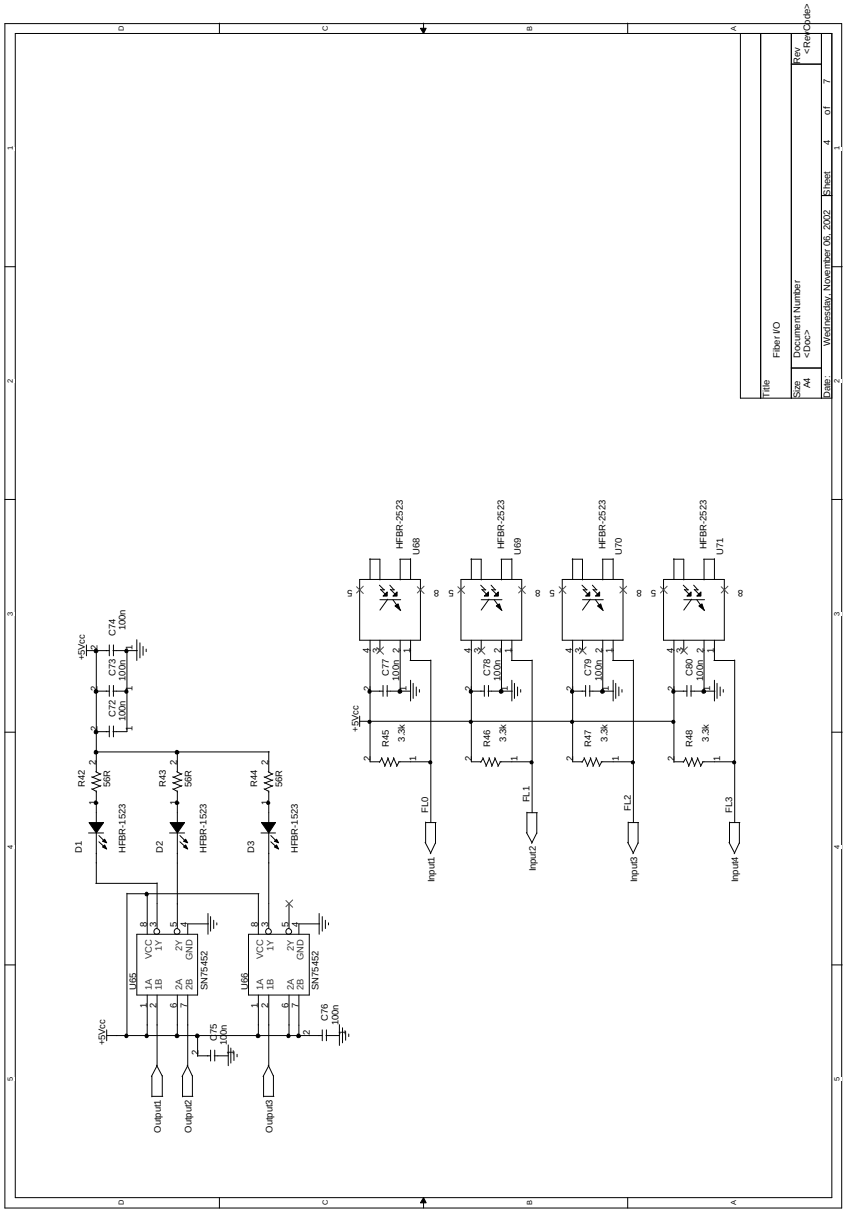

Fig. D.6. Aux. I/O-diagram

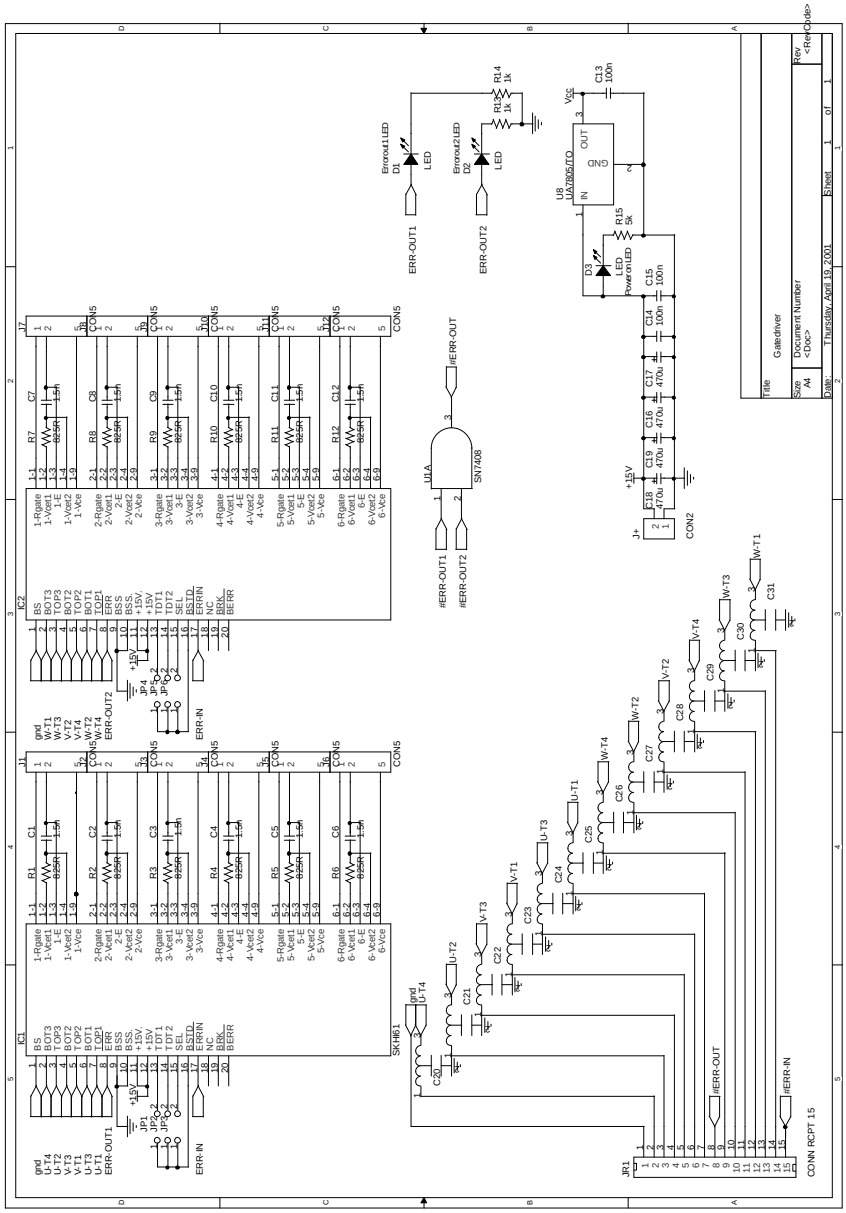

Fig. D.7. gatedriver

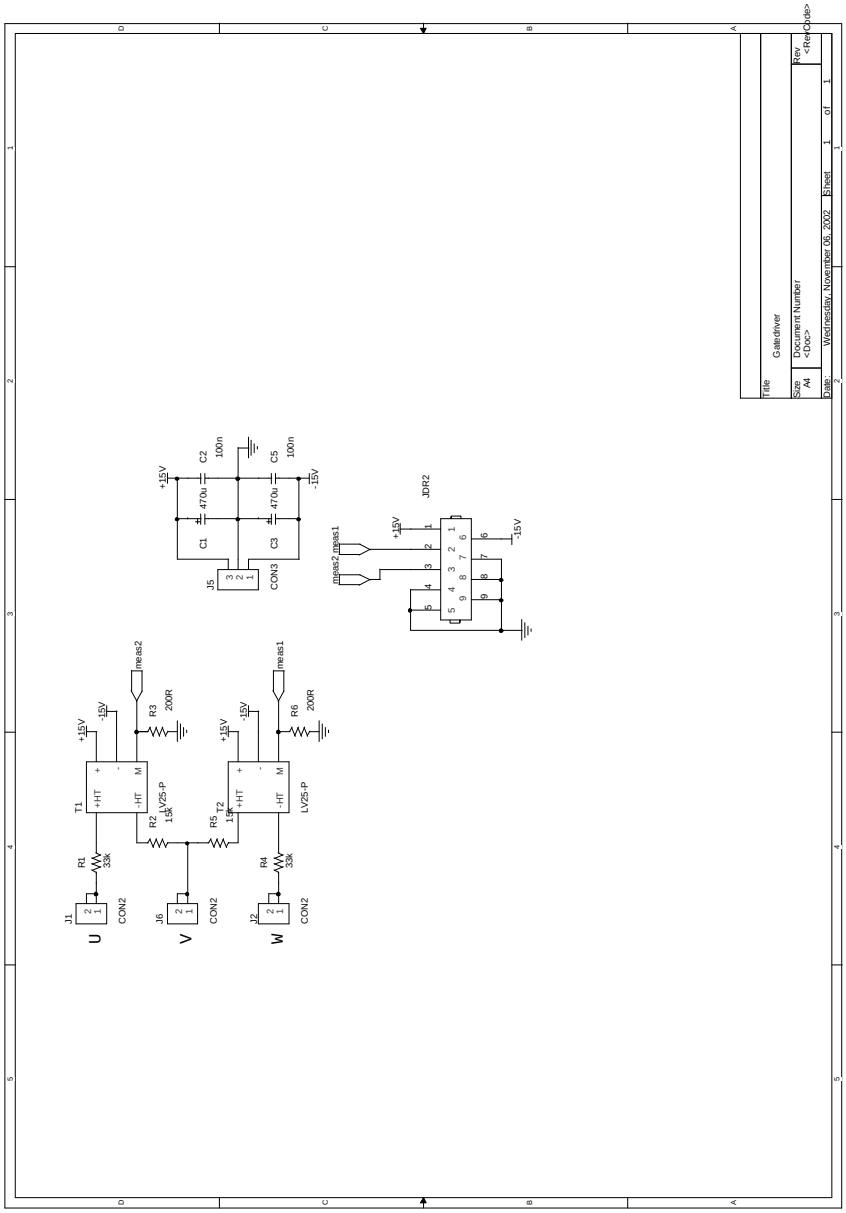

Fig. D.8. Voltage measurements

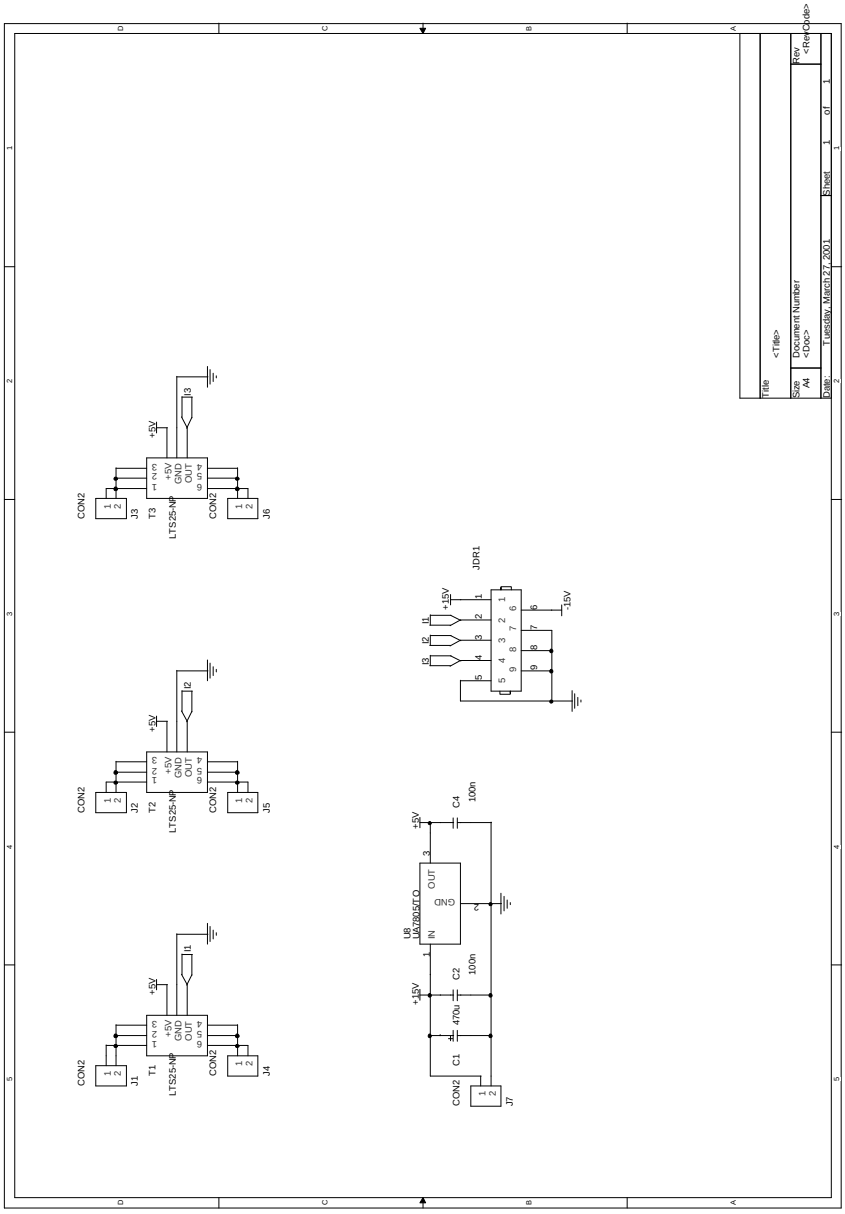

Fig. D.9. Current measurements

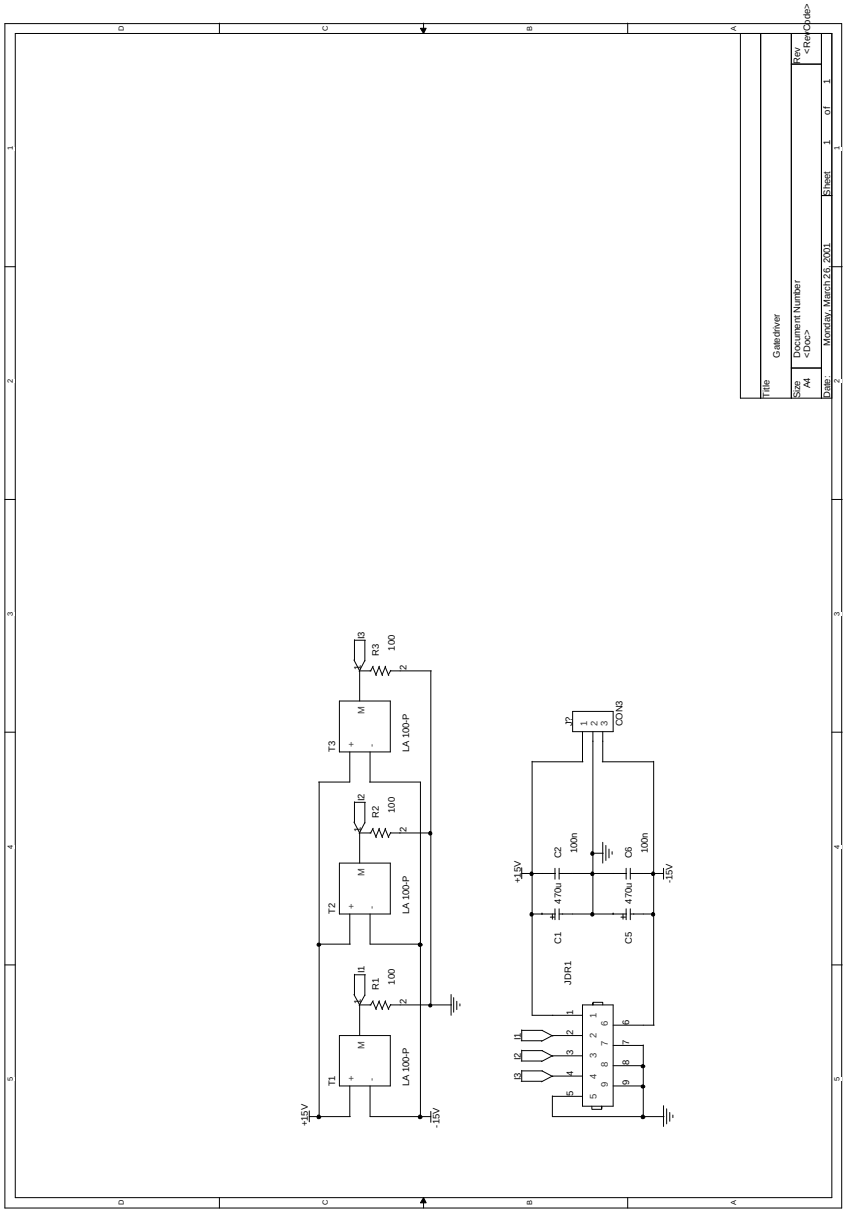

Fig. D.10. "High" current measurements

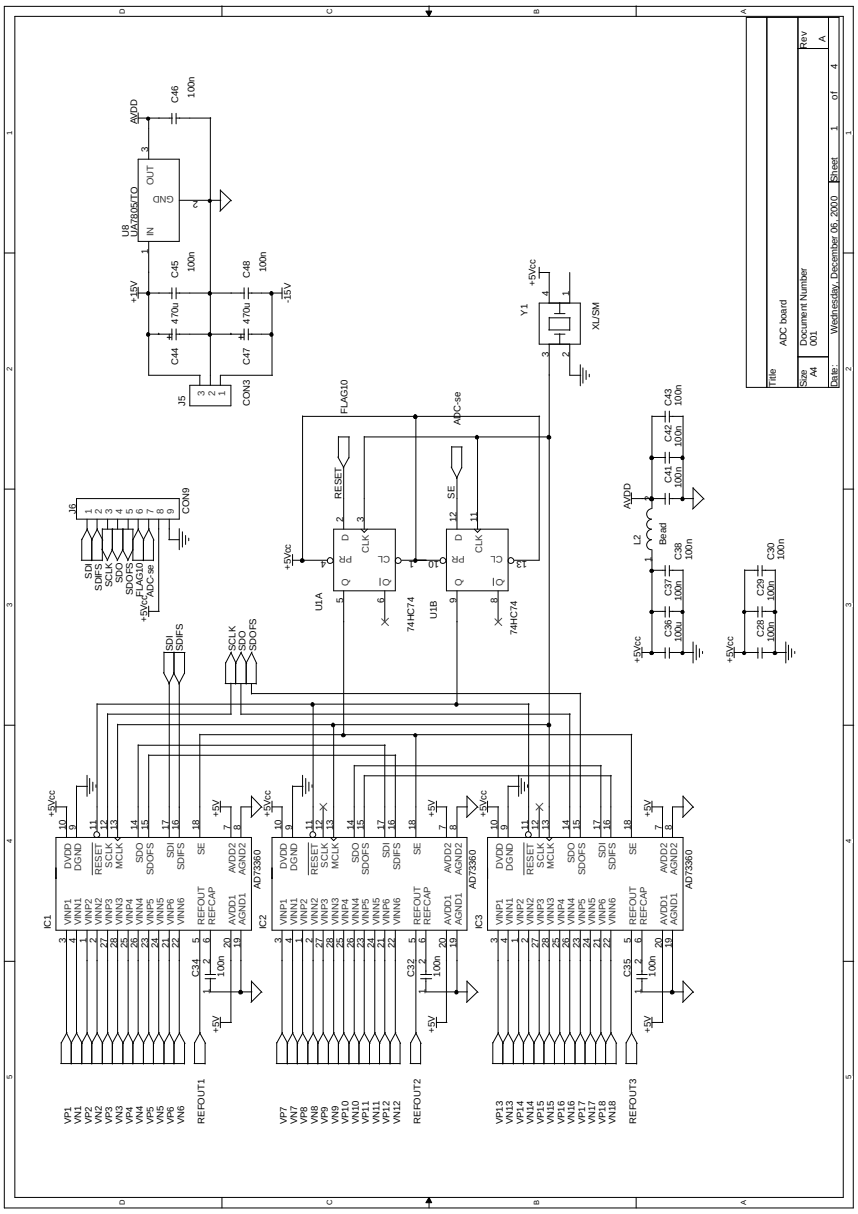

Fig. D.11. AD converter PCB

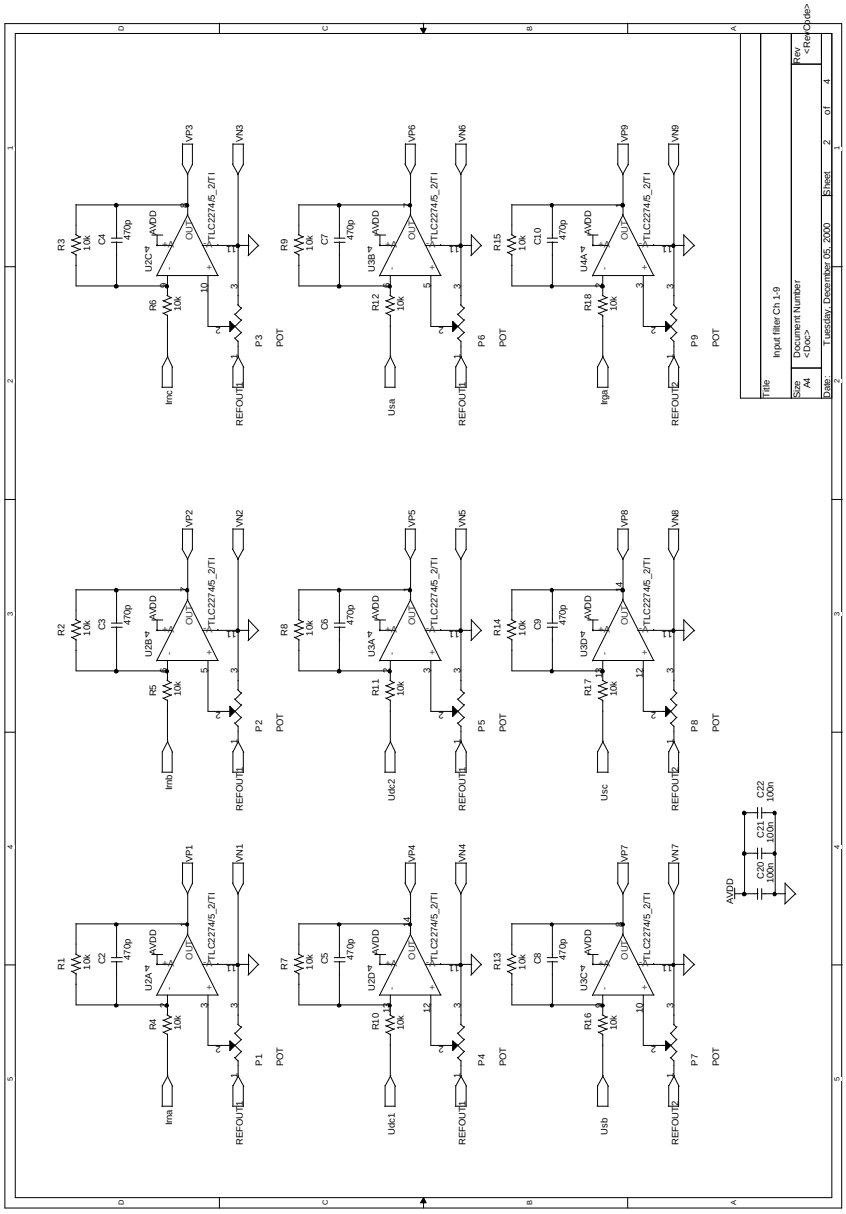

Fig. D.12. Anti-aliasing filter for sigma-delta AD-converter

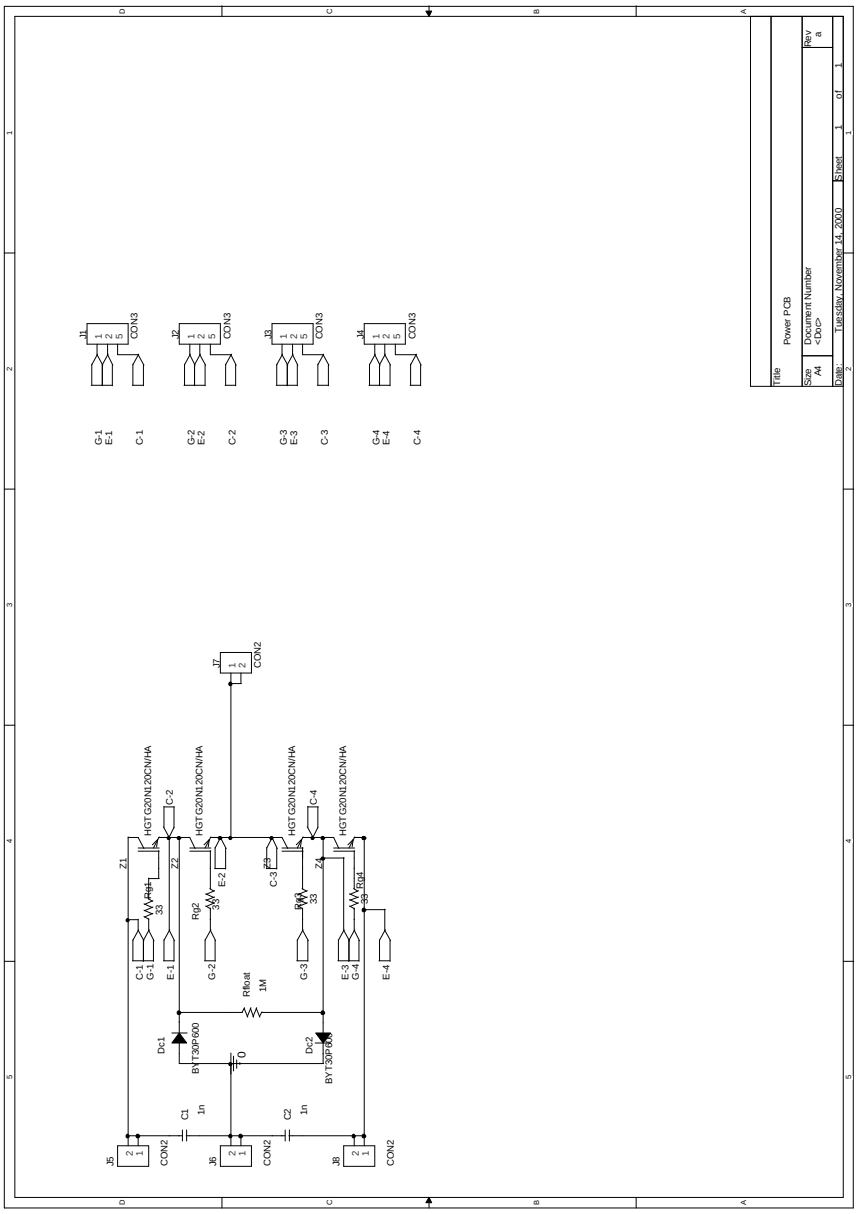

Fig. D.13. NPC diagram

E

Additional Measurements

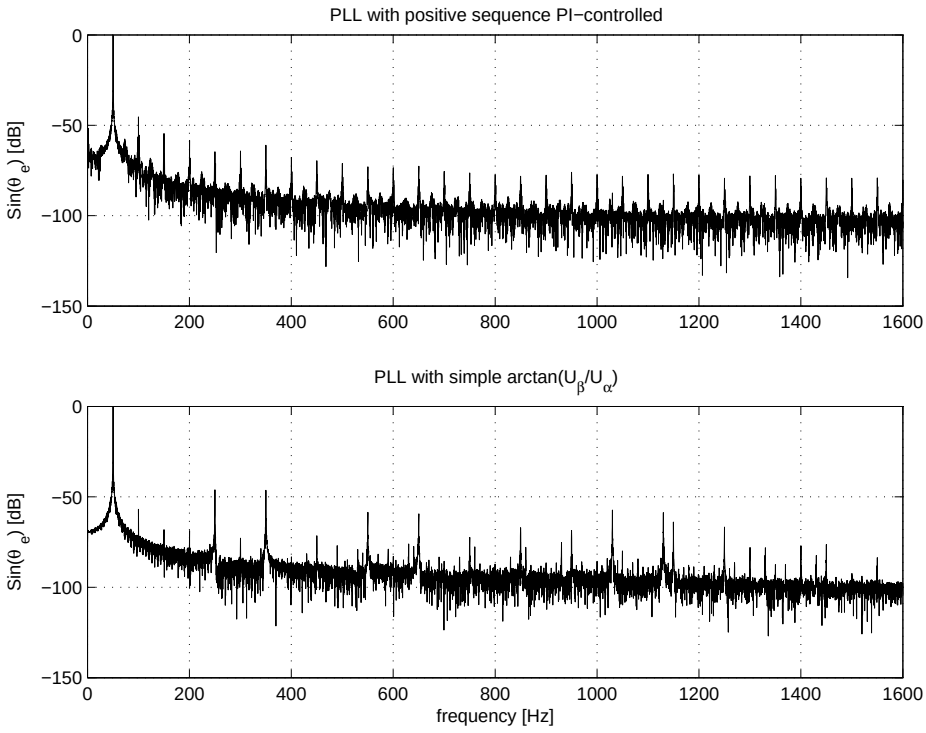

Fig. E.1. Measured frequency spectrum of two different types of PLL (Hammel).

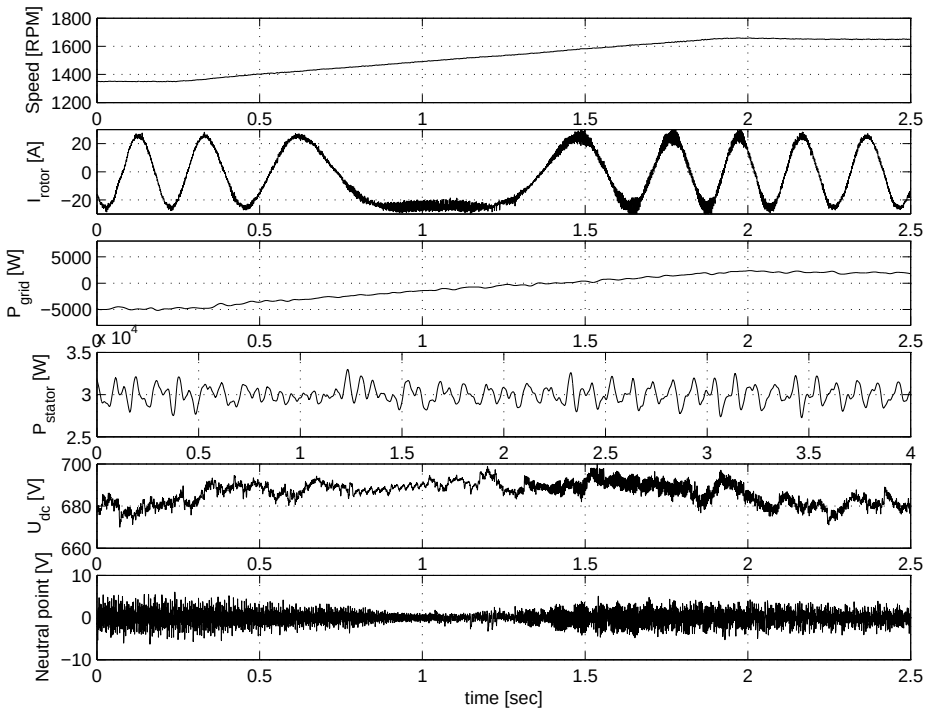

Fig. E.2. Rotor magnetizing with a speed change 1650 - 1350 RPM (Hammel)

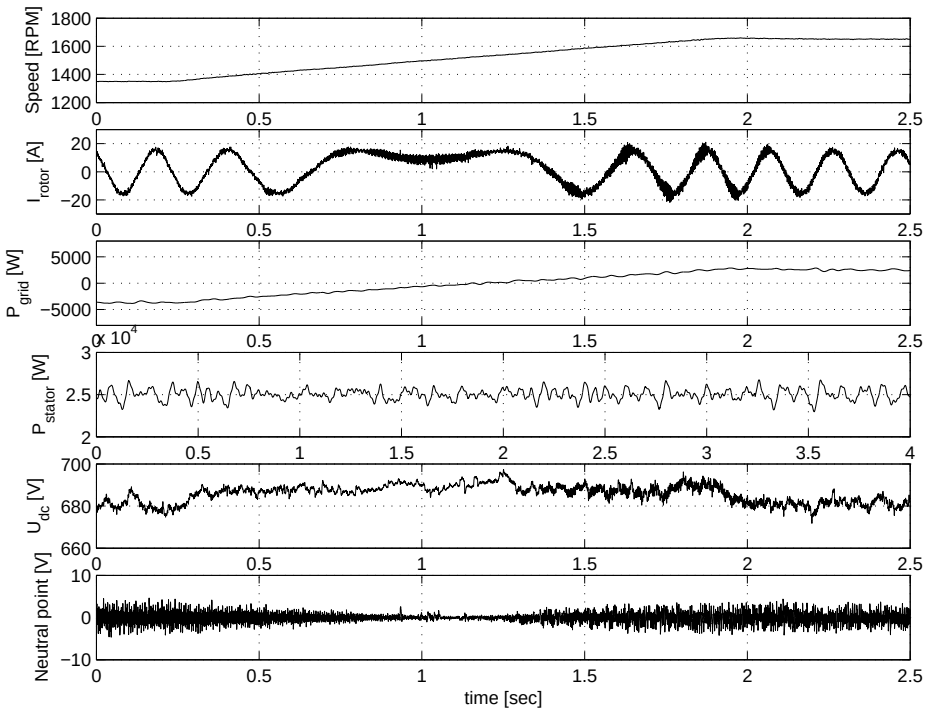

Fig. E.3. Stator magnetizing with a speed change 1650 - 1350 RPM (Hammel)

F

Included Paper

M. Lindholm, T. W. Rasmussen, "Harmonic analysis of Doubly Fed Induction Generators." IEEE Power Electronics and Drives Systems (PEDS 2003), Singapore 17-20 November 2003. Accepted for oral presentation.

Harmonic analysis of Doubly Fed Induction Generators

Morten Lindholm
NEG Micon Control Systems A/S
8450 Hammel, Denmark
fax: +45 8762 2601
Email: mol@control-systems.com

Tonny W. Rasmussen
Oersted.DTU
Technical University of Denmark
2800 Lyngby, Denmark
Email: twr@oersted.dtu.dk

***Abstract*— This paper gives an overview of the frequency spectrum of the stator and rotor currents in a doubly fed induction generator (DFIG) used in wind power applications. The paper also presents a method to eliminate higher harmonics and interharmonics in the DFIG stator current. The method is implemented on a 40 kW laboratory model connected to the utility-grid, where the DFIG is supplied by a back-to-back 3-level NPC-converter.**

***Keywords*— Doubly fed induction generator, Wind turbines, Harmonic elimination.**

I. Introduction

Ten years ago, Doubly Fed Induction Generators (DFIG) with a wound rotor were almost a forgotten type of machine, that was used before soft starters etc. came on the market. They were only used in laboratories, where measurable rotor terminals were practical.

Today DFIGs are widely used, together with Voltage Source Converters (VSC), in wind turbine applications [1]-[4]. Most wind turbine manufactures in the world are now using DFIG systems in their larger turbines (above 1.5 MW) in order to gain more freedom to control the speed and power production. The use of DFIG systems makes it easier to comply with emerging grid requirements from utility companies around Europe [5].

Variable speed wind turbines give a higher mechanical power output, since the most optimal turbine rotor speed can be utilized at any given wind speed [6]. The electrical power output is almost equal to the power output of a fixed speed turbine due to losses in the power electronics etc., so the benefits from variable speed are a more constant power production, a system with a controllable reactive power production and a system with fewer mechanical stresses.

II. The doubly fed induction generator system

The DFIG system used in wind turbines is controlled by two VSCs, as shown in Fig. 1. The converter on the rotor side, controls the torque and the field in the generator. The converter on the grid side, controls the DC-link voltage and the reactive power to the grid from the converter.

The active power transmitted to the grid is the sum of stator power P_s and rotor power P_r, assuming the power converter is loss less, $P_r = P_g$. P_g is the active power from the grid side converter.

$$P_{system} = P_s + P_g \tag{1}$$

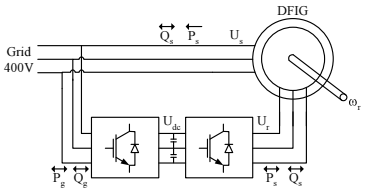

Fig. 1. DFIG system used

The active power from the rotor is proportional to the slip s of the generator:

$$P_r = -s \cdot P_s \tag{2}$$

$$s = \frac{\omega_s - \omega_r}{\omega_s} \tag{3}$$

Fig. 2 shows the relationship between speed and power measured on 4 pole machine, running with P_s = 30kW. The rotor changes speed from 1350 RPM to 1650 RPM e.g. from 10% slip to -10% slip. The middle graph shows how the rotor frequency also is a function of the slip. At synchronous speed the rotor current is DC and at stand still the machine works as a transformer. The bottom graph shows that the rotor power follows (2).

The relationship in (2) makes the DFIG system more attractive to the wind turbine business, compared to a full converter system, since their need for speed variations is limited to about $\pm 25\%$ of nominal speed.

The reactive power of the system Q_{system} is the sum of the reactive power of the stator Q_s and the reactive power from the grid side converter Q_g. This gives:

$$Q_{system} = Q_s + Q_g \tag{4}$$

Stator side reactive power Q_s can be controlled by the magnetizing current in the rotor circuit, that again is controlled by the rotor voltage, here given in the synchronous rotating frame by,

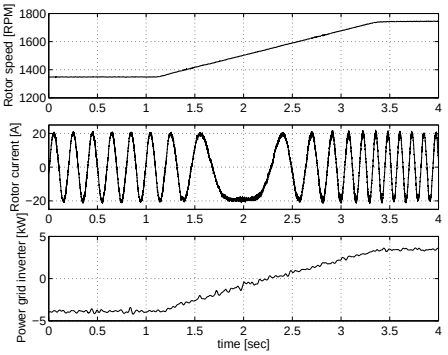

Fig. 2. Speed variation from sub to super synchronous speed

$$u_{dr} = R_r i_{dr} + \sigma L_r \frac{di_{dr}}{dt} - \omega_{slip}\sigma L_r i_{qr} \quad (5)$$

$$u_{qr} = R_r i_{qr} + \sigma L_r \frac{di_{qr}}{dt} - \omega_{slip}(L_m i_{ms} + \sigma L_r i_{dr}) \quad (6)$$

where i_{ms} is the magnetizing current.

The generator is magnetized either from the stator or from the rotor, or a combination. If magnetizing current is not supplied by the rotor, the current will be drawn from the stator. The DFIG is never under magnetized. This property gives more opportunities to maintain a cosϕ equal to one. If the rotor side converter is running at its maximum current and there is need for more active current from the rotor, then the reactive power fed by the rotor converter to the machine can be reduced. The grid side converter might then produce the missing reactive power, if the current is available, so that Q_{system} is maintained at zero.

III. Analysis of Harmonics and Interharmonics in DFIG

Due to the non-sinusoidal distributions of the stator and rotor windings, the air-gap flux will contain higher harmonics, referred to as MMF space harmonics [7]. Another source of harmonics are the slots in the rotor and stator. The slot harmonics are produced by variations in the reluctance due to the slots. The slot harmonics in the air-gap MMF induce slot harmonic voltages in the rotor and stator voltages. Every time the magnetic field in the air gap passes by a stator slot, it will increase the rotor and stator voltage in steps, so even with a pure sinus voltage source, the current from the generator contains harmonics. With a short circuit rotor there will be no induced voltage in the rotor, resulting in less harmonics in the rotor current.

The slot harmonics in the stationary $\alpha\beta$-frame are given by

$$f_{sh} = f_1(\frac{2S}{P}(1+s) \pm 1) \quad (7)$$

S is the number of slots in stator, P is number poles.

Induction machines normally have skewed rotors, which is not the case for DFIG machines. If the rotor is not skewed, it gives higher amplitude slot harmonics.

It has been shown in the literature that Doubly Fed induction motors fed by cycloconverters have certain amount of harmonics content in its current, due to the converter [8]. By using modern self-commutated IGBT inverters with a relatively high switching frequency, the harmonics content in the voltage, produced by the inverter, will be of rather high order due to switching and of no interest for this study.

TABLE I
Stator & rotor current harmonics

Stator harmonics	Rotor harmonics
$(6m-1)f_{grid} - 6(n-1)f_{slip}$	$(6m)f_{grid} - (6n-5)f_{slip}$
$(6m+1)f_{grid} + 6(n-1)f_{slip}$	$(6m)f_{grid} + (6n-5)f_{slip}$
$(6m+1)f_{grid} - 6(n)f_{slip}$	$(6m)f_{grid} - (6n-1)f_{slip}$
$(6m+1)f_{grid} - 6(n)f_{slip}$	$(6m)f_{grid} - (6n+1)f_{slip}$

Table I shows the harmonics in the stator and rotor. The first terms come from the higher harmonics due to the stator, the second terms come from the higher harmonics in the rotor. $n = 1, 2, 3, \ldots$ and $m = 1, 2, 3, \ldots$

Harmonics in the three phase system will rotate in different directions depending on the order of harmonic . The harmonics can be grouped into positive, negative or zero sequence:

Harmonics of the order $h = 6n + 1, \quad n = 1, 2, 3, \ldots$ are of a positive sequence.

Harmonics of the order $h = 6n - 1, \quad n = 1, 2, 3, \ldots$ are of a negative sequence.

Harmonics of the order $h = 3n, \quad n = 1, 2, 3, \ldots$ are of zero sequence.

The positive sequence will rotate in the opposite direction of the fundamental harmonics, and the negative sequence will rotate in the same direction as the fundamental harmonics.

Transforming vectors from a stationary-frame to a synchronous rotating frame here called the $dq-$frame, will result in a counter-clockwise rotation of the $dq-$frame with an angular frequency equal to the fundamental frequency. Transforming the stator current vector $\vec{i}_s$ results in:

$$\vec{i}^{dq} = \vec{i}_s e^{-j(\omega_g t - \frac{\pi}{2})} \quad (8)$$

where ω_g is the angular frequency of the grid voltage.

The fundamental current vector in the stationary $\alpha\beta$-frame will be transformed to a stationary vector in the synchronous rotating dq-frame. Positive sequence harmonics will rotate with the speed $(n-1)\omega_{grid}$, and negative sequence harmonics rotate with the speed $(n+1)\omega_{grid}$.

The fact that the positive sequence harmonics will slow down in rotational speed and the negative sequence harmonics will increase speed, means that the $(6n \pm 1)th$ harmonics in the stationary frame transform to the $(6n)th$ harmonics in the dq-frame. The same is valid for the slip harmonics. They transform to $6mf_{grid} - 6nf_{slip}$.

The slot harmonic in the dq-frame is reduced to only one frequency

$$f_{sh}^{dq} = f_1 \frac{2S}{P}(1+s) \tag{9}$$

The frequency changes as a function of the slip.

IV. Adaptive filtering of higher harmonics

The use of the Least Mean Square (LMS) algorithm to eliminate higher harmonics in line connected converters has been presented by Blasko [9]. Fig. 3 shows the method of the adaptive single frequency notch filter [10]:

$$x_k^s = \sin(n\omega_0 kT) \tag{10}$$
$$x_k^c = \cos(n\omega_0 kT) \tag{11}$$

where T is the sampling period, ω_0 is the notch circular frequency of the filter, k is the discrete time index, and superscripts c and s relate to sine and cosine, respectively. The LMS algorithm cross correlates the reference inputs x_k^s and x_k^c with the error input ε_k and adjust the w_k according to:

$$w_{k+1}^s = w_k^s + 2\mu\varepsilon_k x_k^s \tag{12}$$
$$w_{k+1}^c = w_k^c + 2\mu\varepsilon_k x_k^c \tag{13}$$

μ is the adaptation gain that regulates the how fast the system adapts, and stability of adaptation. Weights are adjusted until the component of noise with frequency ω_0 is eliminated from the error ε_k.

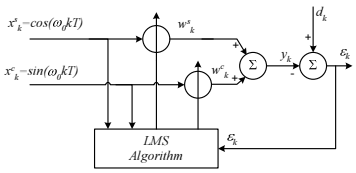

Fig. 3. Single frequency adaptive LMS filter

This can be extended to a multi-frequency filter, were the notch filter x_k and weight function w_k expand to,

$$\vec{X}_k^s = [\ldots x_{nk}^s \ldots]^{\mathrm{T}} \quad \vec{X}_k^c = [\ldots x_{nk}^c \ldots]^{\mathrm{T}} \tag{14}$$

$$\vec{W}_k^s = [\ldots w_{nk}^s \ldots]^{\mathrm{T}} \quad \vec{W}_k^c = [\ldots w_{nk}^c \ldots]^{\mathrm{T}} \tag{15}$$

The filter output is

$$y_k = \vec{W}_k^{s\mathrm{T}} \vec{X}_k^s + \vec{W}_k^{c\mathrm{T}} \vec{X}_k^c \tag{16}$$

V. Implementation

The laboratory system consists of a 40 kW DFIG with a 400V Y-connected stator and Y-connected rotor, with a locked rotor voltage of 1600V. The power converters used are two back to back 3-level neutral point clamped converters [11], each with a rated power of 15 kVA. The control system is based on a single SHARC DSP from Analog Device©. A direct torque controlled frequency converter with an induction motor is used as load for the DFIG machine.

When using the adaptive filtering method together with a DFIG system, it is obvious that the adaptive filter can be applied twice. The grid side converter can be used as a normal active filter [9], additionally the rotor side converter can also be used as an active filter by injecting current into the rotor that are then transformed through the air-gap to the stator.

In the laboratory setup, the LMS algorithm was implement as described in [9] for the grid side inverter. The new development in this paper is the implementation of the adaptive LMS algorithm in the rotor-stator circuit, so that the notch filter currents are injected into the rotor current to eliminate harmonics in the stator current.

A. Grid side filter

The implementation of single frequency notch filters on the grid side converter, has to be made in the stationary $\alpha\beta$-frame to avoid cross coupling between the q and d axes [9].

Therefore the notch filters were implemented in the stationary $\alpha\beta$-frame for the grid side filter. There were some 5th and 7th harmonics in the grid side converter current, and also 11th and 13th. Due to asymmetrical 3rd harmonic content in the 3 phases, the 3rd harmonic was able to flow without a neutral conductor. Three notch filters were implemented, one for each frequency: 150Hz, 250Hz and 350Hz.

The measured grid side current, transformed to the stationary $\alpha\beta$-frame, is the error input ε_k to the filter.

The filter output y has to be multiplied with the line inductor impedance,

$$u_n = y_n \omega_{grid} L \tag{17}$$
$$= \{w_n^s \sin(n\omega_{grid}) + w_n^c \cos(n\omega_{grid})\}\, n\omega_{grid} L$$

where L is the grid side inductor. This gives the signals that are added to the grid side converter voltage reference in the $\alpha\beta$-frame:

$$u_{\alpha ref2} = u_{\alpha ref} + u_{\alpha 3} + u_{\alpha 5} + u_{\alpha 7} \tag{18}$$
$$u_{\beta ref2} = u_{\beta ref} + u_{\beta 3} + u_{\beta 5} + u_{\beta 7} \tag{19}$$

B. Rotor side filter

The notch filters are implemented in the synchronous rotating dq-frame. Eventhough cross coupling between the q and d axes is also present here, it does not affect the filter.

Equations (5) and (6) are reduced in steady state and when neglecting the resistive part, while $R_r \ll n\omega\sigma L_r$, it gives,

$$u_{dr} = -\omega_{slip}\sigma L_r i_{qr} \quad (20)$$
$$u_{qr} = -\omega_{slip}(L_m i_{ms} + \sigma L_r i_{dr}) \quad (21)$$

Equations (20) and (21) show that there is no coupling between u_{dr} and i_{dr}, and similar for u_{qr} and i_{qr}. There is only the cross coupling between d and q.

The fact that the $(6n \pm 1)$th harmonics in the stationary $\alpha\beta$-frame transform to the $(6n)$th harmonics in the synchronous rotating dq-frame means that one filter is enough to eliminate two harmonics. In the setup we tried to eliminate 5th and 7th harmonics at 250Hz and 350Hz, and 5th and 7th slip harmonics at 220Hz and 320Hz with 10% slip.

The measured stator current, transformed to the synchronous rotating dq-frame, is the error input ε_k to the filter.

The filter output y has to be multiplied with the impedance from (20),

$$u_6 = y_6\omega_{slip}\sigma L_r \quad (22)$$
$$= \{w_6^s \sin(6\omega_{grid}) + w_6^c \cos(6\omega_{grid})\}\, 6\omega_{slip}\sigma L_r$$

$$u_{slip} = \left\{ \begin{array}{l} w_{slip}^s \sin(6(\omega_{grid} - \omega_{slip})) \\ +w_{slip}^c \cos(6(\omega_{grid} - \omega_{slip})) \end{array} \right\} \cdot \frac{\omega_{grid} - \omega_{slip}}{\omega_{grid}} 6\omega_{slip}\sigma L_r \quad (23)$$

This gives the signals that are added to the rotor converter voltage reference in dq-frame:

$$u_{dref2} = u_{dref} + u_{d6} + u_{dslip} \quad (24)$$
$$u_{qref2} = u_{qref} + u_{q6} + u_{qslip} \quad (25)$$

VI. Results

Fig. 4 shows a frequency spectrum of a 40 kW DFIG generator with a rotor speed of 1350 RPM equal to 10% slip. The stator power is 25kW. The most dominant harmonics in the stator current are the 5th, 250Hz and the 5th slip harmonic at 220Hz, followed by the 7th and the 7th slip harmonics at 320Hz with a 10% slip. The two spikes at 1030Hz and 1130Hz correspond with (7) and the fact that the machine has 48 slots, 4 poles and runs at 10% slip.

Next in Fig. 5 the rotor speed has changed to supersynchronous speed at 1650 RPM equal to -10% slip. The 5th and 7th harmonics are still present, the two slip harmonics have moved to 280Hz and 380Hz respectively. The slot harmonics are now at 1270Hz and 1370Hz.

In Fig. 6 a frequency spectrum from 0-500Hz of the rotor and stator current with and without the adaptive filter is shown. The figure shows a reduction of the 5th and 7th harmonics in the stator current by about 20dB. The slip harmonics are reduced by about 30dB.

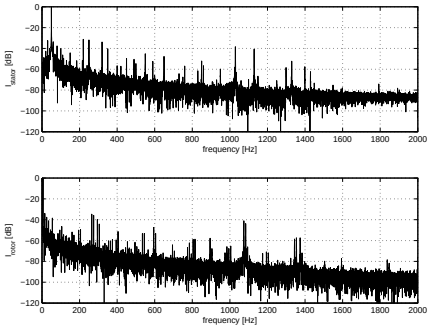

Fig. 4. Spectrum stator and rotor current, speed: 1350 RPM

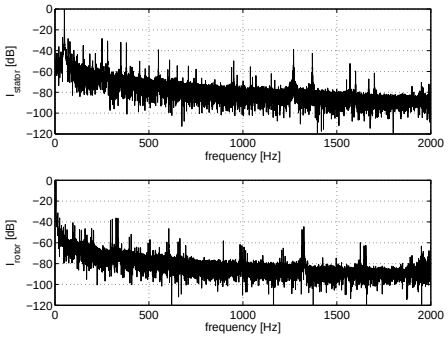

Fig. 5. Spectrum stator and rotor current, speed: 1650 RPM

Finally Fig. 7 shows the frequency spectrum of the grid side current. On the upper graph, there are no adaptive filters added. The lower graph shows a 10dB reduction in the 3rd, 5th and 7th harmonics.

VII. Conclusion

The spectrum of the DFIG machine has been presented. Some of the differences between the normal induction generator and the DFIG have been stated. A method to reduce harmonics has been presented, and verified experimentally. The method gives an easy and reliable way to eliminate or reduce harmonics from the DFIG generator. The implementation of the adaptive filter in the rotor side converter gives a fairly good reduction in the harmonic frequencies applied. On the grid side, the effect of filter is limited and other adaptive filter methods should be considered.

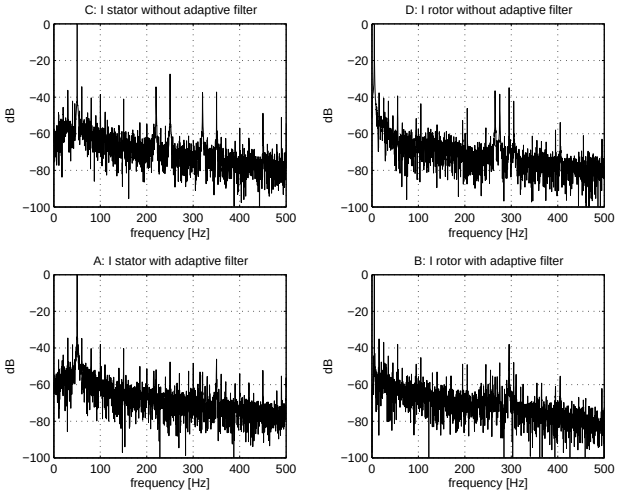

Fig. 6. Current spectrums w. & w.out adaptive filtering at 1350 RPM (10% slip)

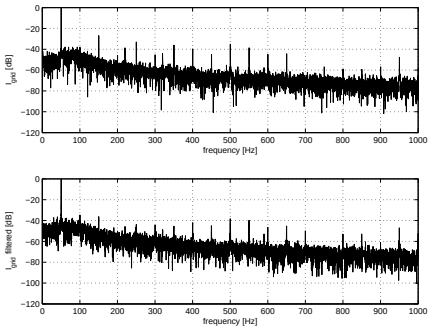

Fig. 7. Spectrum of the grid side current without and with adaptive filter.

REFERENCES

[1] R. Pena, J. Clare, and G. Asher, "Doubly fed induction generator using back-to-back pwm converters and its application to variable-speed wind-energy generation," *Electric Power Applications, IEE Proceedings-*, vol. 143, no. 3, pp. 231–241, 1996.

[2] B. Eggert, "1.5 mw wind power station with low ac-line distortion using a standard doubly-fed generator system with field orientation control," *EPE'97. 7th European Conference on Power Electronics and Applications*, pp. 739–42 vol.2, 1997.

[3] S. Muller, M. Deicke, and R. De Doncker, "Adjustable speed generators for wind turbines based on doubly-fed induction machines and 4-quadrant igbt converters linked to the rotor," *Conference Record of the 2000 IEEE Industry Applications Conference. Thirty-Fifth IAS Annual Meeting and World Conference on Industrial Applications of Electrical Energy (Cat. No.00CH37129)*, pp. 2249–54 vol.4, 2000.

[4] A. Dittrich, W. Hofmann, A. Stoev, and A. Thieme, "Design and control of a wind power station with double fed induction generator," *EPE'97. 7th European Conference on Power Electronics and Applications*, pp. 723–8 vol.2, 1997.

[5] E. on Netz GmbH, "Ergänzende netzanschlussregeln für windenergieanlagen," 2001.

[6] S. Heier, *Grid Integration of Wind Energy Conversion Systems*. John Wiley Sons, 1998.

[7] P. Vas, *Sensorless Vector and Direct Torque Control*. Oxford University Press, 1998.

[8] M. Yamamoto and O. Motoyoshi, "Active and reactive power control for doubly-fed wound rotor induction generator," *Power Electronics, IEEE Transactions on*, vol. 6, no. 4, pp. 624–629, 1991.

[9] V. Blasko, "Adaptive filtering for selective elimination of higher harmonics from line currents of a voltage source converter," *Industry Applications Conference, 1998. Thirty-Third IAS Annual Meeting. The 1998 IEEE*, vol. 2, pp. 1222–1228 vol.2, 1998.

[10] J. Glover, J.R., "Adaptive noise canceling applied to sinusoidal interferences," *IEEE Transactions on Acoustics, Speech and Signal Processing*, vol. ASSP-25, no. 6, pp. 484–91, 1977.

[11] A. Nabae, I. Takahashi, and H. Akagi, "A new neutral point clamped pwm inverter," *IEEE Transactions on Industry Applications*, vol. IA-17, no. 5, pp. 518–23, 1981.